Numerical Investigation of Propulsion Efficiency Depending on Propeller Position

Aung Ko Latt

Master Thesis

presented in partial fulfillment
of the requirements for the double degree:
“Advanced Master in Naval Architecture” conferred by University of Liege
"Master of Sciences in Applied Mechanics, specialization in Hydrodynamics, Energetics and Propulsion” conferred by Ecole Centrale de Nantes

developed at University of Rostock, Germany
in the framework of the

“EMSHIP”
Erasmus Mundus Master Course
in “Integrated Advanced Ship Design”

Ref. 159652-1-2009-1-BE-ERA MUNDUS-EMMC

Supervisor: Prof. Nikolai Kornev, University of Rostock

Reviewer: Prof. Mihaela Amoraritei, University of Galati

Rostock, February 2017

This document is not the full thesis.

This is the public version of the thesis, due to confidentiality issue (asked by Mecklenburger Metallguss GmbH - MMG).

The full version is available at ULG and URO (Prof. RIGO and Prof.Bronsart)

Ph RIGO
EMSHIP Cooordinator

ABSTRACT

Increasingly tight schedules in ship building projects as well as the opportunity of reliable RANS CFD codes including fast and flexible meshing methods lead to the application of numerical propulsion tests as standard procedures in the propeller design process. Due to the benefits of numerical self-propulsion simulations, the investigation of the ship propulsion characteristics and the analysis of fluid flow around the hull, propeller and rudder can be easily done with the relevant computational time consumptions.

In this thesis, the propulsion efficiency of the ship is mainly investigated when the axial position of the propeller behind hull is varied. Furthermore, the flow field around the ship hull and operating propeller is presented and analyzed according to the changes of propeller position behind hull. The pressure quantities exerted on the hull at certain points are determined when the positions of propeller operating behind the ship hull are relocated. These numerical investigations are made for the self-propulsion simulations with and without rudder condition to observe the influence of rudder.

With a view to fulfill the objectives of this thesis, the numerical propulsion simulations of the ship for different propeller positions with&without rudder conditions and reverse open water simulation of that propeller are performed by using commercial code RANSE solver, ANSYS CFX. All of the simulations are carried out in model scale of research vessel's hull, its corresponding propeller and rudder. With the results of these simulations, the powering prediction results and propulsion characteristics data in full-scale operating conditions are extrapolated from model scale results by using the ITTC 1978 service performance prediction procedure. The results of propeller hydrodynamic performance and self-propulsion characteristics are analyzed to compare and investigate the propulsion efficiency between the different positions of propeller operating behind the hull with&without rudder conditions. Finally, the distribution of pressure and velocity contour are executed to study the flow effects on the hull-propeller-rudder interaction.

ACKNOWLEDGEMENTS

First of all, a special gratitude I give to my supervisor, Prof. Dr.-Ing. Nikolai Kornev, whose contribution in stimulating suggestions and encouragement, which led to the creation of this thesis. I would also like to take this opportunity to thank Prof. Dr.-Ing. Robert Bronsart for giving valuable advice with technical problems and guiding me to the success of the master thesis. My grateful thanks are also extended to various people; to Prof. Mihaela Amoraritei to review this thesis; to Prof. Philippe Rigo who have been always concerning us in every possible way; to all the professors and lecturers who taught and encouraged me; to all staffs in ULG, ECN and URO involved in EMSHIP Erasmus programme.

I would like to delicate a special thanks to Mr. Robert Pfannenschmidt, my supervisor during the internship, for the constructive discussions and valuable insights in marine propulsion field. His willingness to answer all my questions has been very much appreciated. I would also like to acknowledge with much appreciation the crucial role of MMG team that made my work possible and pleasant, receiving me with open arms and answering all my questions with delight. I also want to show my gratitude to Mr. Tom Geodicke from MMG office in Waren, for his support during my internship. It is inevitably that the development of this thesis won't be possible without the support from MMG office technician member, Mr. Rodrigo dos Santos Correa.

My gratitude for all parties who have supported me during finishing my study in three different countries, which left me unforgettable memories.

Finally and most importantly, I would like to express my gratitude to my family especially my mother, for the unconditional love that led me all the way to here. All will become meaningless without their supports.

This thesis was developed in the frame of the European Master Course in "Integrated Advanced Ship Design" named "EMSHIP" for "European Education in Advanced Ship Design", Ref.: 159652-1-2009-1-BE-ERA MUNDUS-EMMC.

TABLE OF CONTENT

ABSTRACT....3

ACKNOWLEDGEMENTS....5

TABLE OF CONTENT....7

LIST OF FIGURES....11

LIST OF TABLES....15

Declaration of Authorship....17

1. Introduction....19

1.1. General....19

1.2. Objectives And Scope of Thesis....21

1.3. Methodology And Approach....22

1.4. Literature Review....24

1.5. Outline Of Thesis....26

2. Background Theory....27

2.1. Resistant Test....27

2.1.1. Analysis of Model Scale Results....*27*

2.2. Open Water Test....29

2.2.1. Analysis of The Open Water Results....*29*

2.3. Self-Propulsion Test....31

2.3.1. Two Methods of Propulsion Test....*31*

2.3.2. Analysis of Propulsion Test Results....*33*

2.4. ITTC 1978 Performance Prediction Method (IPPM78)....34

2.4.1. Thrust Identity Principle....*35*

2.4.2. Full Scale Correction for Total Resistance Coefficient of Ship....*36*

2.4.3. Scale Effect Corrections for Propeller Characteristics....*37*

2.4.4. Scale Corrections for Full Scale Wake and Operating Condition of Propeller....*39*

2.5. Computational Fluid Dynamics (CFD) 41
2.6. Governing Equations 42
2.7. Modeling 43
2.7.1. Incompressible Reynolds Averaged Navier–Stokes Equations - RANS *44*
2.7.2. Turbulence Models *46*
2.8. ANSYS CFX Solver 49
2.9. Near Wall Y^+ Treatment 49
2.10. Numerical Discretization 51
2.10.1. Finite Volume Method *52*
2.10.2. Meshing Generation *52*
2.11. Rotating Motion 54
2.11.1. Multiple Reference Frame Model or Moving Refrence Frame MRF (Frozen Rotor) *54*
2.11.2. Sliding Mesh *55*
3. Numerical Propulsion Simulation in Model Scale 57
3.1. Workflow of Numerical Propulsion Simulation Procedure 57
3.2. Test Data Description 59
3.3. Geometry Creation of Computational Domains in DesignModeler 60
3.3.1. Computational Ship Domain Creation *60*
3.3.2. Computational Propeller Domain Creation *62*
3.4. Meshing Implementation of Computational Domains in ANSYS Workbench Meshing 62
3.4.1. Mesh Generation of Ship Domain *63*
3.4.2. Mesh Generation of Propeller Domain *65*
3.5. Numerical Propulsion Simulation Set Up 66
3.5.1. Simulation Setup Details in ANSYS CFX *66*
3.6. Solving Simulation in ANSYS CFX 69
3.7. Test Case Definition 70

4. Numerical Reverse Open Water Simulation of Propeller in Model Scale 73

4.1. Geometry Creation Of Computational Domains In DesignModeler 73

4.2. Meshing Implementation of Computational Domains in ANSYS Workbench Meshing 73

4.3. Numerical Reverse Open Water Simulation Set Up.....74

4.4. Solving and Post-Processing Of ROW Simulation Results 74

5. Numerical Investigation on Results of Propulsion Simulations.....76

5.1. Determination of Full-Scale Propulsion Results By Using ITTC 1978 Service Performance Prediction Method.....76

5.1.1. Computed Results from Numerical Propulsion Simulations for Four Cases.....76

5.1.2. Performance Prediction Method.....77

5.2. Investigation on Results of Propulsion Simulations 82

5.2.1. Importance of Propulsive Coefficient Prediction for Powering and Propulsion of Ship 83

5.2.2. Investigation on Results of Propeller Hydrodynamics Performance in Model Scale and Full-Scale Prediction 85

5.2.3. Investigation on Results of Relative Rotative Efficiencies (η_R) for Four Cases With/Without Rudder Conditions.....88

5.2.4. Investigation on Results of Hull Efficiency (η_H) for Four Cases With/Without Rudder Conditons 90

5.2.5. Investigation on Results of Delivered Power (P_D) and Propulsion Efficiency (η_D) for Four Cases With/Without Rudder Conditions.....94

6. Results for Fluid Flow Characteristics and Hull Pressure Determination of Numerical Propulsion Simulation in model Scale.....98

6.1. Results of Fluid Flow Characteristics in Numerical Propulsion Simulations in Model Scale.....98

6.2. Determination of Hull Pressure at Pressure Tapping Points in Model Scale.....109

6.2.1. Hull Pressure Prediction.....109

6.2.2. Evaluation and Comparison of Hull Pressure at Pressure Tapping Points for Four Cases with/without Rudder Condition 111

7. Conclusion and Further Developments.....116

8. References.....118

LIST OF FIGURES

Figure 1 Test Setup for Resistance Test [28].....27
Figure 2 Results of Wake Measurement [26] 27
Figure 3 Flow Chart of Resistance Test Analysis [27].....28
Figure 4 Test Setup for Propeller Open Water Test [28].....29
Figure 5 Flow Chart of Open Water Test Analysis [27] 30
Figure 6 Propeller open water diagram, as resulting from a propeller open water test [28] ...30
Figure 7 Propulsion Test Setup for Constant Loading Method [28].....32
Figure 8 Flow Chart of Self Propulsion Test Analysis [27] 33
Figure 9 ITTC 1978 Service Performance Prediction Procedure [30].....34
Figure 10 Workflow Chart of CFD Simulations (https://www.learncax.com/knowledge-base/blog/by-category/cfd/introduction-to-cfd-part-ii-selecting-the-domain).....41
Figure 11 Available CFD methods with their accuracy and CPU time [36] 44
Figure 12 Flow Chart of General Solution Used in ANSYS CFX [42] 49
Figure 13 Various geometrically shaped 3D elements (Wikimedia commons 2015) [34] 53
Figure 14 Coordinate System for Relative Velocity [54].....54
Figure 15 Two-Dimensional Grid Interface [54] 56
Figure 16 Workflow of Numerical Propulsion Simulation Procedure.....58
Figure 17 CAD Representation of Test Case Vessel in Full Scale(Profile View).....59
Figure 18 CAD Representation of Test Case Vessel in Full Scale(Perspective View) 59
Figure 19 CAD Representation of Test Case Propeller in Full Scale in Perspective View 60
Figure 20 Computational Domain Size and Patch Descriptions of Ship Domain (Stationary Domain) 61
Figure 21 Computational Domain Size and Patch Descriptions in Stern View of Ship Hull in Ship Domain 61
Figure 22 Computational Domain Size and Patch Descriptions in Propeller Domain [Perspective View (Left) & Side View (Right)].....62
Figure 23 Tetrahedral Volume Mesh Implementation of Ship Domain (Stationary Domain) .64
Figure 24 Tetrahedral Volume Mesh Implementation of Ship Domain (Stationary Domain) Half View.....64
Figure 25 Mesh Generation of Ship Domain Near Hull.....64
Figure 26 Refinement Meshing Implementation of Hull and Rudder in Ship Domain [Top (Stern View) & Bottom(Bow View).....65

Figure 27 Tetrahedral Volume Mesh Implementation of Propeller Domain (Rotating Domain) 65
Figure 28 Refinement Meshing Implementation around Hub and Blades of Propeller in Propeller Domain 65
Figure 29 Boundary Assignment of Ship Domain 68
Figure 30 Meshing in Propeller Cylinder as Sliding Interface 69
Figure 31 Blade Reference Line [57] 70
Figure 32 Propeller Blades Position for Four Cases along The Hub 71
Figure 33 Computational Domain Size and Patch Descriptions of OWT Domain (Stationary Domain) 73
Figure 34 Computational Domain Size and Patch Descriptions of Propeller Domain (Rotating Domain) 73
Figure 35 Tetrahedral Volume Mesh Implementation of OWT Domain (Stationary Domain) 73
Figure 36 Refinement Meshing Implementation of Propeller Shaft in OWT Domain 74
Figure 37 Tetrahedral Volume Mesh Implementation of Propeller Domain (Rotating Domain) 74
Figure 38 Refinement Meshing Implementation around Hub and Blades of Propeller in Propeller Domain 74
Figure 39 Boundary Assignment of OWT Domain and Propeller Domain 74
Figure 40 Numerical Open Water Chart Data in Model Scale 75
Figure 41 Numerical Open Water Chart Data in Full Scale 75
Figure 42 Towing Force Vs Thrust Curve for Model Self-propulsion Results 78
Figure 43 Example of Open Water Chart in Model Scale 79
Figure 44 Example of Open Water Chart Data (Full Scale) with Propeller Load Curve 80
Figure 45 Components of Ship Powering and Efficiencies – Main Consideration [60] 83
Figure 46 Thrust Coefficient K_T Results of Model Scale and Full-Scale Prediction for Propulsion Simulation With/Without Rudder Conditions 86
Figure 47 Advance Coefficient J Results for Model Scale and Full-Scale Prediction for Propulsion Simulation With/Without Rudder 86
Figure 48 Comparison of Open Water Efficiency (η_0) Between Model Scale and Full Scale Prediction for Propulsion Simulation With/Without Rudder Conditions 87
Figure 49 Results of Torque Coefficient K_Q for Model Propeller in Open Water Condition and Behind Hull Condtion of With/Without Rudder Conditions 89

Figure 50 Comparison between Relative Rotative Efficiency η_R for Four Cases With/Without Rudder Conditions....90
Figure 51 Comparison of Thrust Deduction Coefficient t for Four Cases With/Without Rudder Conditions....91
Figure 52 Comparison between Wake Fraction w in Model and Full Scale for Propulsion Simulations With/ Without Rudder Conditions....92
Figure 53 Comparison of Hull Efficiency η_H between Four Cases for Simulaions With/Without Rudder Conditions....94
Figure 54 Results of Delivered Power P_D in Full Scale Prediction for Four Cases from Propulsion Simulations With/Without Rudder Conditions....95
Figure 55 Comparison of Propulsion Efficiency η_D between Four Cases from Propulsion Simulations With/Without Rudder Conditions....96
Figure 56 Pressure Distribution on Model Hull with Inflow Velocity 1.95 m/s....98
Figure 57 Determination of Propeller Plane Positions and Hull Pressure Point Locations....99
Figure 58 Axial Wake Distribution at Upstream Plane (x/R=0.3) from Propeller Plance in Model Scale For Four Cases (With Rudder Condition)....99
Figure 59 Axial Wake Distribution at Upstream Plane (x/R=0.3) from Propeller Plance in Model Scale For Four Cases (Without Rudder Condition)....100
Figure 60 Axial Wake Distribution at Downstream Plane (x/R=-0.5) from Propeller Plance in Model Scale For Four Cases (With Rudder Condition)....100
Figure 61 Axial Wake Distribution at Downstream Plane (x/R=-0.5) from Propeller Plance in Model Scale For Four Cases (Without Rudder Condition)....101
Figure 62 Pressure Distribution on Stern of The Hull and Rudder with Axial Velocity Field in Mid Plane (Port Side View) For Case1 with Rudder Condition....102
Figure 63 Pressure Distribution on Stern of The Hull and Rudder with Axial Velocity Field in Mid Plane (Port Side View) For CaseOrig with Rudder Condition....102
Figure 64 Pressure Distribution on Stern of The Hull and Rudder with Axial Velocity Field in Mid Plane (Port Side View) For Case2 with Rudder Condition....102
Figure 65 Pressure Distribution on Stern of The Hull and Rudder with Axial Velocity Field in Mid Plane (Port Side View) For Case3 with Rudder Condition....103
Figure 66 Pressure Distribution on Stern of The Hull with Axial Velocity Field in Mid Plane (Port Side View) For Case1 without Rudder Condition....103
Figure 67 Pressure Distribution on Stern of The Hull with Axial Velocity Field in Mid Plane (Port Side View) For CaseOrig without Rudder Condition....103

Figure 68 Pressure Distribution on Stern of The Hull with Axial Velocity Field in Mid Plane (Port Side View) For Case2 without Rudder Condition.....104
Figure 69 Pressure Distribution on Stern of The Hull with Axial Velocity Field in Mid Plane (Port Side View) For Case3 without Rudder Condition.....104
Figure 70 Pressure Distribution on Blades Resulted form Case1 Simulation with Rudder Condition [Left(Face) & Right(Back)].....106
Figure 71 Pressure Distribution on Blades Resulted form CaseOrig Simulation with Rudder Condition [Left(Face) & Right(Back)].....106
Figure 72 Pressure Distribution on Blades Resulted form Case2 Simulation with Rudder Condition [Left(Face) & Right(Back)].....106
Figure 73 Pressure Distribution on Blades Resulted form Case3 Simulation with Rudder Condition [Left(Face) & Right(Back)].....107
Figure 74 Pressure Distribution on Blades Resulted form Case1 Simulation without Rudder Condition [Left(Face) & Right(Back)].....107
Figure 75 Pressure Distribution on Blades Resulted form CaseOrig Simulation without Rudder Condition [Left(Face) & Right(Back)].....107
Figure 76 Pressure Distribution on Blades Resulted form Case2 Simulation without Rudder Condition [Left(Face) & Right(Back)].....108
Figure 77 Pressure Distribution on Blades Resulted form Case3 Simulation without Rudder Condition [Left(Face) & Right(Back)].....108
Figure 78 Dummy Model and Propeller in A Cavitation Tunnel [57].....110
Figure 79 Comparison of Hull Pressure on Pressure Tapping Points For Four Cases with/without Rudder Condition.....111
Figure 80 Comparison of Pressure Coefficient on Pressure Tapping Points For Four Cases with/without Rudder Condition.....112
Figure 81 Distribution of Total Pressure Contour on Hull Surface for Four Cases from Simulations with Rudder Condition.....113
Figure 82 Distribution of Total Pressure Contour on Hull Surface for Four Cases from Simulations without Rudder Condition.....114

LIST OF TABLES

Table 1 Advantages and Limitations of All Types of Mesh Cells [46].....54
Table 2 Main Dimensions of Test Case Ship in Full Scale and Model Scale 59
Table 3 Main Dimensions of Test Case Propeller in Full Scale and Model Scale 60
Table 4 No. of Nodes and Elements Generated in Ship Domain.....65
Table 5 No. of Nodes and Elements Generated in Propeller Domain.....66
Table 6 Boundary Condition Assignment in Inlet and Outlet of Stationary Domain 67
Table 7 Boundary Condition Assignment in Stationary and Rotating Domains 67
Table 8 Numerical Propulsion Simulation Running Conditions for Each of Four Cases 71
Table 9 Boundary Condition Assignment in Inlet and Outlet of Stationary Domain 74
Table 10 Boundary Condition Assignment in Stationary and Rotating Domains 74
Table 11 Computed Results For Model Scale of Numerical Propulsion Simulations for Four Cases.....77
Table 12 Propulsion Results of Full Scale Prediction from Model Scale by using Numerical Propulsion Simulation Results with/without Rudder and Numerical Open Water Simulation Results.....82

Declaration of Authorship

I declare that this thesis and the work presented in it are my own and have been generated by me as the result of my own original research.

Where I have consulted the published work of others, this is always clearly attributed.

Where I have quoted from the work of others, the source is always given. With the exception of such quotations, this thesis is entirely my own work.

I have acknowledged all main sources of help.

Where the thesis is based on work done by myself jointly with others, I have made clear exactly what was done by others and what I have contributed myself.

This thesis contains no material that has been submitted previously, in whole or in part, for the award of any other academic degree or diploma.

I cede copyright of the thesis in favour of the University of Rostock, Germany.

*Date:**12.1.2017* *Signature*

1. INTRODUCTION

1.1. General

When we consider about ship designs and design improvements, the propulsive efficiency is one of the most important issues. The marine propellers are necessary to be very efficient. The propulsive efficiency for ship designs is mandatory to be predicted and determined by model tests and full-scale observations in pre-design stage. Furthermore, there are many approaches and analysis have been done by researchers and naval architects in order to achieve the increasingly propulsive efficiency by comparing and investigating the ship hulls, propellers, rudders and energy saving devices.

High marine fuel costs and low freight rates are causing operators to seek ways to boost ship efficiency. Advanced ship propulsion solutions are one way to achieve considerable improvements in this regard but require highly detailed concept, design and construction processes. [1]

Model tests of self-propulsion were conventionally the only way to determine and evaluate the characteristics of hull-propeller interaction, the powering performance and the propulsion parameters of the ship. With the rapid advances in the field of computational fluid dynamics (CFD) and high-performance computing (HPC), numerical simulations of ship self-propulsion have recently gained increasing attention. [2] Due to the increased capabilities of numerical flow simulations, it has become possible to make Computational Fluid Dynamics (CFD) analyses of self-propulsion calculations of ships with propellers. The detailed geometry of the propeller can be taken into account, as well as the free surface wave making effects, which occur when a vessel sails through the water. The effects of dynamic sinkage and trim can be taken into account as well, either based on a series of prescribed values or automatically in the calculations process. Based on the current status of the numerical methods, the experimental self-propulsion tests can be reproduced with sufficient accuracy. Combined with a bare hull resistance calculation and an open water performance calculation, the interaction factors for wake-fraction, thrust deduction and relative rotative efficiency can be determined. [3]

The study of propeller-hull and propeller-hull-rudder interaction is critical to predict the efficiency of the propeller as well as its influences on the resistance of the ship hull. By the Computational Fluid Dynamics (CFD) method, the viscous flow computation of the ship hull is usually coupled with some propeller programs either by viscous method or by potential method. In the viscous model, the propeller, hull and rudder geometries are all resolved directly

in the RANS grid in which the solid bodies are considered as no-slip faces and all of these become parts of the viscous flow solution. This method gives very detailed information about the stern and propeller flows, but the grid generation is considerably complicated and unsteady flow simulation is required. [4]

There are two methods to model propellers in the study of hull-propeller-rudder interaction or ship self-propulsion. One is the actuator disk method in which the propeller is represented by some equivalent body force. The other is the full RANS approach in which the propeller has meshed geometrically. The body force method in the study of self-propulsion is preferred because of considerably less computational time compared with the direct RANS simulation. Direct RANS simulation in which the propeller and hull have geometrically meshed is relatively new and requires substantial computer resources. The advantage of the method is that there would be no uncertainties resulting from body force modelling, allowing induced velocity to be introduced. [2]

Concerning the free surface, two different approaches can be used normally. One was to omit the free surface to limit the complexity and the size of the numerical model. In this case only the under-water part of the hull is considered and the free-surface boundary condition is replaced by a symmetry condition on the still water surface. This approach allows comparison with measured propeller data from the cavitation tunnel, but not with resistance. Another approach was to include the free surface and the part of the hull above the water. By doing this it was both possible to compare measured propeller quantities and resistance. [5]

The prediction of the fluid dynamic interaction between hull and propeller is very important for the improvement of ship performance since this interaction is directly related to propulsion performances, vibrations and noises. Propellers produce periodically varying exciting forces in the three-way non-uniform wake field at the stern, which are transferred to the hull by the shaft system and fluids, significantly increasing the underwater noise and vibration of the hull. The pressure transferred to hull surface by fluids is called fluctuating pressure, on which extensive researches and calculations have been made by scholars all around the world. [6]

1.2. Objectives And Scope of Thesis

In order to meet the environmental challenges on the marine transport industry over the next 25 years, as predicted by the World Bank (Streamline 2008), the vessels and propulsion systems need to be more efficient. Less conservative solutions may be necessary to meet this requirement. It has been known for a long time that an increase in propeller diameter and moving a propeller aft behind the hull will result in increased propulsive efficiency. The total propulsive efficiency will be broken down into components to distinguish the different effects. [7] The starting point of this investigation is to do variations of propeller's axial positions for a given state-of-the-art preliminary design. The present thesis is also focused on the utilization of numerical methods to the investigation of the propulsion characteristics of the ship propulsion system due to the effects of hull-propeller-rudder interaction by performing the numerical CFD simulations. The numerical investigation on the propulsion efficiency of the ship propulsion and powering system is mainly to be done when the axial position of the propeller is changed behind ship hull by simulating numerical model self-propulsion test with standard numerical procedure.

Since the efficiency of propulsion system is strongly dependent on the propeller performance (i.e. thrust force, torque of the propeller and its efficiency) and the hydrodynamic characteristics such as effective wake to the propeller, thrust deduction and relative rotative efficiency. These components are necessary to determine and investigate accordance to the different propeller positions behind the ship hull. The fluid flow phenomenon around the hull, propeller and rudder is required to study for a deeper understanding of flow effects and resulting hull efficiencies. Furthermore, the pressure distributions on the hull, propeller and rudder are examined with respect to the operating propeller loading condition. The hull pressure fluctuations in the stern region near the operating propeller are determined and investigated with the changes of propeller position behind hull.

These numerical investigations are implemented in the conditions of with & without rudder considerations although the self-propulsion simulations are usually carried out with hull, propeller and rudder model. This allows observing the influence of rudder on the fluid flow effects in hull-propeller interaction.

Therefore, this thesis work is motivated to investigate the propulsion efficiency for different propeller positions with the usage of numerical propulsion simulations in the conditions of with&without rudder consideration. The research vessel and its corresponding propeller are used as test case data.

1.3. Methodology And Approach

As mentioned in the objective and scope of the thesis, the investigations are necessary depending on the different propeller positions operating behind the ship hull by using numerical simulation methods. Therefore, the detailed list of tasks are as following;

1. Test Case Data Determination and Test Case Definition for Different Propeller Positions i.e. Case1, Case2, Case3 and CaseOrig
2. Geometry Creation, Mesh Implementation, and Case Setup in ANSYS Workbench for Numerical Propulsion Simulations
3. Numerical Propulsion Simulations including Hull, Propeller Together with Rudder Condition for Four Cases in Model Scale
4. Geometry Creation, Mesh Implementation and Case Setup in ANSYS Workbench for Numerical Reverse Open water Simulation
5. Numerical Reverse Open water Simulation of the Propeller in Model Scale
6. Numerical Propulsion Simulations including Hull, Propeller Together without Rudder Condition for Four Cases in Model Scale
7. Extrapolation of Model Scale Results to Full Scale Operating Conditions by using ITTC'78 Performance Prediction Procedure for Four Cases with&without Rudder Conditions
8. Compare the Post-processing Results of Case1, 2 and 3 against CaseOrig for Both Conditions of with&without Rudder
9. Determine and Compare the Hull Pressure Fluctuation at Certain Points of Case1, 2 and 3 against CaseOrig for Both Conditions of with&without Rudder

According to the tasks mentioned above, the first step of this work is the test case data determination for the study. The CAD representation of reasearch vessel's hull form, its corresponding propeller and rudder are provided in IGES format which allows seeing the full scale of the hull form together with propeller and rudder. So then the different axial positions of propeller behind hull are defined for self-propulsion simulations.

A combined hull, propeller and rudder is extremely complicated, and it requires an advanced numerical method in order to model the flow also. It is necessary to build the model step by step and gradually increase complexity throughout the project. One of the most widely used numerical methods is based on numerical solution of the continuity equation and the RANS equations in conjunction with a turbulence model. The RANS method seems to perform well for complex fluid flows and therefore, the RANS solver is used to carry out all of the numerical

simulations in this thesis. The computations were performed with RANS solver, ANSYS CFX which solves the continuity equation and the RANS equations by means of finite volume method. Concerning the turbulence model, closure of the Reynolds stress problem is achieved utiziling the two equations SST k-ω turbulence model for all simulations with automatic y^+ treatment.

The rotating of propeller is treated in two ways. For numerical self-propulsion simulations of the propeller rotating behind hull, the time-dependent sliding mesh approach is used that means the whole propeller domain rotates with a speed equivalent to the propeller rate of revolution. The numerical propulsion simulations are run in transient mode. In numerical reverse open water simulation, the propeller inflow is uniform, and the moving reference frame approach is applied, i.e. the blade velocity is set on the propeller blades and centripetal effects are included in additional source terms in the momentum equations. The steady state mode is adopted for numerical reverse open water simulation.

The RANS model including the physical representation of hull, propeller and rudder would require a complex computational grid consisting of millions of cells. The direct RANS calculations are carried out on unstructured tetrahedral volume mesh type for all simulations. The mesh arrangement and boundary conditions and the simulation parameters are chosen on the standard data of Company and projects and activities from literature review. Concerning the free surface model in self-propulsion condition, it is omitted since the results are only concerned on the propulsion characteristics and the calculation of the free surface is extremely expensive, concerning required number of cells and of required computational time.

The numerical propulsion simulations in model scale are carried out for all cases with&without rudder conditions. The results of full scale operating conditions are evaluated from the combined results in model scale of numerical propulsion simulation, numerical reverse open water simulation and experimental resistance test according to the ITTC 1978 performance prediction procedure. The propeller rpm used in the simulations are set at the values used during the model tests. Therefore, it is not necessary to search for the self-propulsion point. This saves resources since a calculation of the self-propulsion point will require an iterative procedure where the propeller revolutions are adjusted so that the propeller thrust balances the resistance. The visualization of the post-processing results for propulsion simulations are studied for flow effects on the hull-propeller-rudder interaction. Finally, the hull pressure fluctuation coefficients for three points on the hull near stern region are evaluated from the mean pressure exerted on the hull due to the flow of rotating propeller. All results from Case1,2 and 3 with&without rudder conditions are compared and investigated referring to that of CaseOrig.

1.4. Literature Review

This thesis is dealing with a wide range of engineering studies concerning on the numerical simulations of flows around the propeller rotating behind the hull and in open water conditions, the numerical analysis and investigation between the hull, propeller and rudder interaction and the investigation of scale effects by using numerical propulsion and open water simulations.

In a paper of “Ship Self Propulsion with different CFD methods: from actuator disk to viscous inviscid unsteady coupled solvers” Villa et al (2012) [8], a viscous inviscid coupled algorithm has been formulated and applied to the analysis of ships advancing in self-propulsion. The method is based on a panel method to solve for the unsteady forces produced by the propeller blades working in the hull wake and a RANSE solver for the calculation of hull drag with the action of the propeller. The two solvers are coupled through effective wake (in the panel method) and unsteady body forces (in the RANSE solver). The two layers k-ε turbulence model is used. Both the methodologies seem adequate to estimate the thrust deduction factor resulting in a predicted hull total resistance error within the 3% on the experimental measurement.

T. BUGALSKI(2007) [9] wrote about a paper for an overview of the selected results of the European Union Project EFFORT. The European-Union EFFORT project focuses on validating and introducing innovative CFD prediction methods for the performance of the ship/propeller combination at the full scale, instead of the usual model scale. The following observations have been taken into account: a modification of the standard model for free surface flows simply by increasing the mesh density and changing the turbulence model to obtain an accurate wake field would result in unacceptable computational time, the time required to obtain a convergence of the free surface flow is even few times longer than the convergence time for the flow without free surface. The block-structured, hexahedral mesh has been generated with the use of ANSYS ICEM CFD Hexa. The computations have been carried out using the FLUENT solver with two turbulence models: SST k-ω and RSM. The results of the wake field computations with the mesh of high density yield the following conclusions: the results obtained with the two-equation SST k-w model are better than the results obtained with the coarse grid, but are still poor, the results obtained with the RSM model are satisfactory, so this model of turbulence seems to be a good choice for the accurate wake field computations.

Paik et al (2013) [10] performed simulations of cavitation flow and hull pressure fluctuation for a marine propeller operating behind a hull using the unsteady RANS. A full hull body submerged under the free surface is modeled in the computational domain to simulate directly the wake field of the ship at the propeller plane. Simulations are performed in design and ballast

draught conditions to study the effect of cavitation number. And two propellers with slightly different geometry are simulated to validate the detectability of the numerical simulation. All simulations are performed using a commercial CFD software FLUENT. The simulation results for the hull pressure fluctuation induced by a propeller are also compared with the experimental results showing good agreement in the tendency and amplitude, especially, for the first blade frequency.

Abdel-Maksoud et al. (2000) [11] computed hull-propeller interaction of Korean container ship (KCS) with the geometrically meshed propeller using CFX. Although relatively coarse meshes were used, the numerical results were encouraging with error rates in the range of 5%−7% for predicted propeller loads. As a free surface was not taken into account in their calculations, total resistance cannot be therefore correctly predicted. Lübke (2005) [12] studied the hull-propeller interaction of KCS with the geometrical modelling of a propeller using CFX. He investigated the mesh and time step effects on the hydrodynamic loads. Free surface elevation was prescribed from the potential based method. Overall, good agreement between the calculations and measurements was achieved. The results showed that the computed pressure resistance exhibits unrealistic high frequency oscillation, which would therefore introduce large errors in the simulation of self-propulsion. Carrica et al. (2010) [13] adopted a Proportional-Integral (PI) speed controller to find the self-propulsion point of a free running ship using the overset grid technique of the latest code CFDSHIP-IOWA .

In the publication of AQUO [14], the organizations of UNIGE, SU, CEHIPAR and SSPA made the predictions by using different numerical simulations. The predictions cover different aspects related to the prediction of the flow field to the propeller, its interaction with the hull, the development of unsteady pressure fields, unsteady induced pressures, cavitation development, noise generation and propagation.

Knutsson and Larsson(2011) [7] used CFD software SHIPFLOW with a zonal approach (RANS, potential flow and boundary layer methods, and the propeller is represented by a lifting line method. The original propeller and a larger one were systematically moved aft, and the delivered power, as well as the propulsive coefficients, are computed. Results were compared with experimental data from SSPA. They proposed one way by moving the propeller aft behind the hull. This allows the propeller diameter to increase without risks of pressure pulses being transferred to the hull. An increase in efficiency may then be achieved, reducing environmental impacts and cost. This was referred to as the large area propeller (LAP) concept and is investigated.

1.5. Outline Of Thesis

The present thesis consists of eight sections which are organized according to the work flow and method approach. Chapter One describe the motivation and challenge of this work, scopes of thesis, some available literatures and methods and approaches used for numerical simulations.

In Chapter Two, the experimental test procedures for resistance, open water and self-propulsion are shortly mentioned and this allows to analyse the results from these tests which are combined to evaluate the full scale powering and propulsion results by adopting ITTC 1978 performance prediction method. In this chapter, the basic computational fluid dynamics and numerical modelling applied in this thesis are also explained in theoretically.

The test case definitions for different propeller positions and pre-processing of numerical propulsion simulations including geometry creation, meshing implementation and simulation set up are included in Chapter Three.

The pre-processing, solving and post-processing results of the numerical reverse open water simulation is described in Chapter Four.

The main objective of this thesis about the investigation of the propulsion efficiency is presented in Chapter Five. In this chapter, the results in model scale from numerical propulsion simulations, numerical reverse open water simulation and experimental resistance test are combined to determine the full scale operating conditions by using the ITTC 1978 performance prediction method. The results of four cases from simulations with&without rudder conditions are compared and investigated according to the factors which can affect the propulsion efficiency of the ship.

Chapter Six shows the illustration of the hull-propeller-rudder interaction from the point of view of fluid flow. The influence of rudder on the propulsion characteristics can be seen in the visualization of pressure and velocity distribution from the results of simulations. Moreover, the hull pressure fluctuations resulted from the operating propeller are determined in this chapter. The observation of pressure distribution on the hull surface is presented to understand the flow effects of propeller when the simulations are performed with&without rudder.

Finally, in Chapter Seven, the summary of work done, problem experienced in the work and further work to research development are shortly prescribed.

The list of references can be found in Chapter Eight.

2. BACKGROUND THEORY

2.1. Resistant Test

The purpose of the resistance test is the ship pure hull resistance at different speeds [15]. In other words, we can determine a form factor, k, calculate the wave making resistance coefficient, C_R and then determine the full-scale resistance, R_{TS} by doing resistance test. The form factor is calculated according to Prohaska's method using results from low speed resistance tests (Lindgren et al., 1978) [16]

The resistance test is performed on the basis of geometric-, kinematic- and dynamic-similarity criteria. This implies that the geometrical similar scaled model are towed at Froude scaled speeds to ensure correctly scaled wave resistance

The set up for a resistance test is presented in Figure 1. As seen from the figure the model is attached to a towing carriage by a dynamometer that measures the resistance R_{TM} during the test. Further, the vessel speed V_M are recorded, and these two values are the input to the scaling procedure from the resistance test. These values will be used to determine the residual resistance coefficient C_R, which is assumed equal in model and full scale, and in the end to give an estimation of required power for the ship. [15]

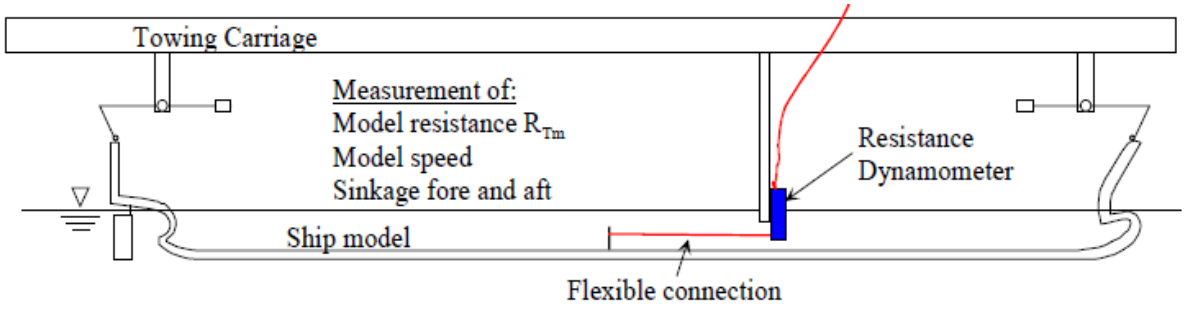

Figure 1 Test Setup for Resistance Test [19]

Removed due to Non-disclosure Agreement

Figure 2 Results of Wake Measurement [18]

2.1.1. Analysis of Model Scale Results

ITTC Recommended Procedure and Guidelines (ITTC, 2011) described the following extrapolation procedure from model scale results to full-scale results. When the resistance test has been performed, a data series including V_M and R_{TM} will be used to determine necessary propulsive power for the full scale ship, through this following extrapolation procedure.

1. Total Resistance Coefficient of Model (C_{TM})

$$C_{TM} = \frac{R_{TM}}{\frac{1}{2}\rho_M S_M V_M^2} \quad (1)$$

2. Frictional Coefficient of Model (C_{FM})

$$C_{FM} = \frac{0.075}{(log_{10}Re - 2)^2} \quad (2)$$

3. Total Resistance of Coefficient of Ship (C_{TS})

$$C_{TS} = (1 + k)C_{FS} + \Delta C_F + C_A + C_R + C_{AAS} \quad (3)$$

4. Residuary Resistance (C_R)

$$C_R = C_{TM} - C_{FM}(1 + k) \quad (4)$$

5. Resistance of The Ship (R_{TS})

$$R_{TS} = C_{TS}(0.5\ \rho_S S_S V_S^2) \quad (5)$$

6. Effective Power (P_E)

$$P_E = R_{TS}\ V_S \quad (6)$$

Figure 3 presented a condensed version of the test analysis procedure. They show the order in which data acquired from the test are analyzed to determine values that will be used in the extrapolation. The intermediate blocks indicate the order of calculation of the various coefficients. The final block in each flow chart has the data that will be passed to the method.

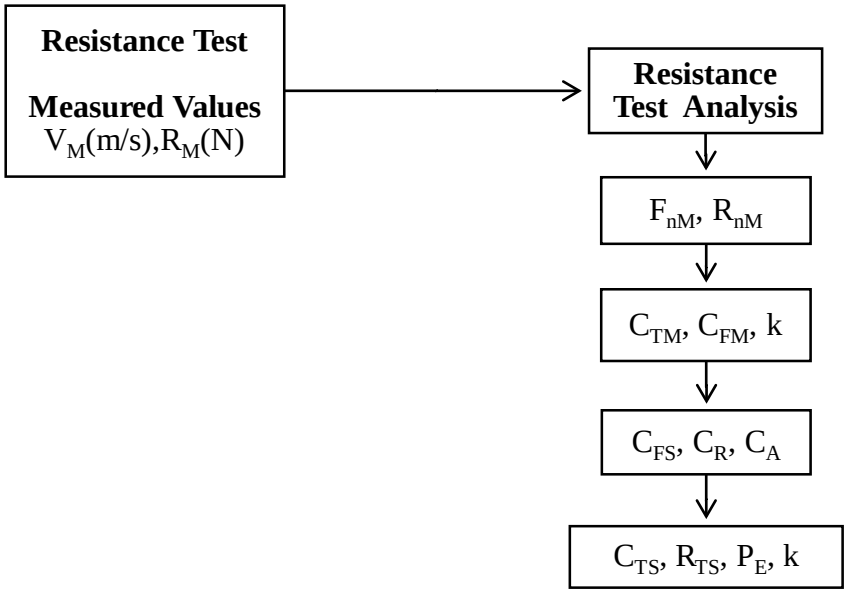

Figure 3 Flow Chart of Resistance Test Analysis [17]

2.2. Open Water Test

Although in reality the propeller operates in the highly non-uniform ship wake, a standard propeller test is performed in uniform flow yielding the so-called open-water characteristics, namely thrust, torque, and propeller efficiency. The model scale for the model propeller should be the same as for the ship [18]. The purpose of the propeller open water test is to measure the performance of the propeller alone, without the hull present. This allows the inflow of water to be unaffected by the hull. In the propeller open water test, the propeller is mounted on a propeller open water dynamometer, which is like an extremely slender thruster with pulling propeller Fi

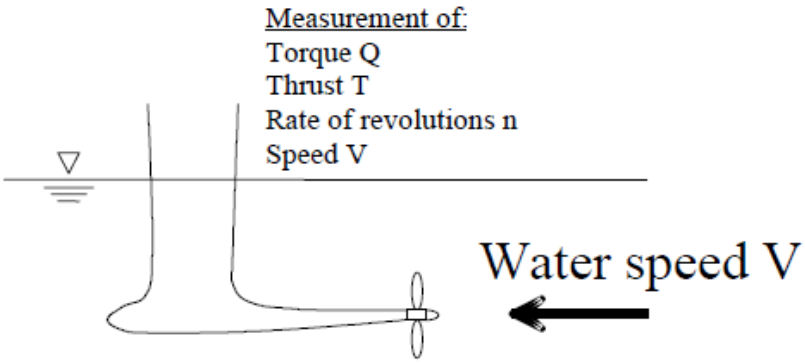

Figure 4 Test Setup for Propeller Open Water Test [19]

The propeller is equipped with a dummy propeller cap. The resistance (thrust) and torque of the dummy propeller cap and propeller hub is measured in separate runs and subtracted from the results so that one effectively gets the performance characteristics of the propeller blades. One measures the propeller torque, thrust, and revs, as well as the speed. Tests are usually done at constant propeller revs, varying the speed from zero to a speed that gives zero propeller thrust. [19]

2.2.1. Analysis of The Open Water Results

The following measured data can be determined as non-dimensional characteristics of the model propeller that can be plotted in the traditional open water chart as shown in Figure 6.

- Speed (V_A)
- Thrust (T_M)
- Torque (Q_M)
- Propeller revolutions (n)
- Water temperature (T_W)

The dimensionless values of the thrust and torque values are made dimensionless by Equations (8) and (9). Speed of advance is also expressed as a dimensionless value J, by Equation (10).

1. Thrust Coefficient (K_T)

$$K_{TM} = \frac{T_M}{\rho_M n_M^2 D_M^4} \tag{7}$$

2. Torque Coefficient (K_Q)

$$K_{QM} = \frac{Q_M}{\rho_M n_M^2 D_M^5} \tag{8}$$

3. Advanced Coefficient (J)

$$J = \frac{V_A}{n_M D_M} \tag{9}$$

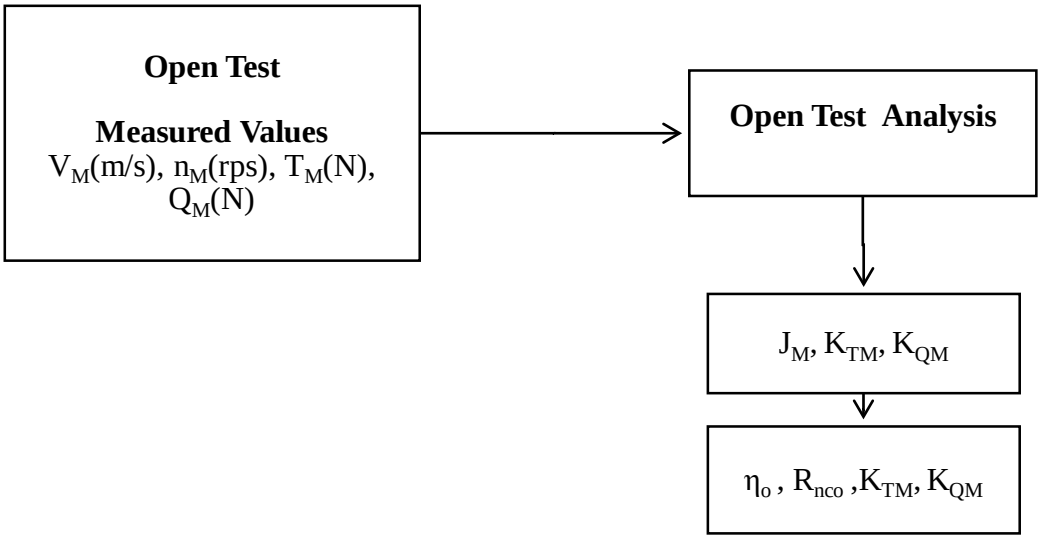

Figure 5 Flow Chart of Open Water Test Analysis [17]

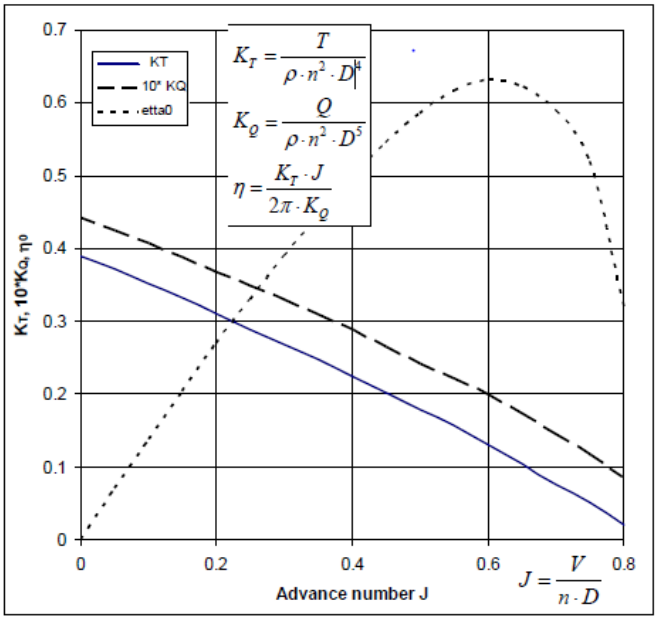

Figure 6 Propeller open water diagram, as resulting from a propeller open water test [19]

2.3. Self-Propulsion Test

The purpose of the self-propulsion test is to perform a model test that takes the propeller-hull interaction effects into account. [15] Propulsion tests are performed to determine the power requirements, but also to supply wake and thrust deduction, and other input data (such as the wake field in the propeller plane) for the propeller design [18].

The self-propulsion test models as closely as possible the ship operating condition, i.e. the appendages are in place and the propeller is operating in a non-uniform flow due to the model wake. In addition, the experimental arrangement ensures that the model is free to heave and pitch and sometimes also free to roll and surge. If the model propeller balances the model resistance and fully self-propels the model then it will be working at a higher thrust loading than the full scale. This is due to the difference in friction coefficients between the model and full-scale and the allowance at the full scale for roughness and still-air through the correlation allowance [17]. Because The tests are again performed for Froude similarity. The total resistance coefficient is then higher than for the full-scale ship since the frictional resistance coefficient decreases with increasing Reynolds number. This effect is compensated by applying a 'friction deduction force, F_D [18].

The propeller then has to produce a thrust that has to compensate the total resistance R_T minus the compensating force F_D. The propulsion test is conducted with constant speed. The rpm of the propeller is adjusted such that the model is in self-propelled equilibrium. Usually the speed of the towing tank carriage is kept constant and the rpm of the propeller varied until an equilibrium is reached i.e. the propeller is said to be at the ship self-propulsion point. A propeller dynamometer then measures thrust and torque of the propeller as a function of speed. In addition, dynamical trim and sinkage of the model are recorded. [18]

Self Propulsion Point Towing Force (F_D)

$$F_D = \frac{1}{2}\,\rho_M V_M^2 S_M [C_{FM} - C_{FS} - C_A] \tag{10}$$

2.3.1. Two Methods of Propulsion Test

When preforming a self-propulsion test there are two different approaches on how the test can be performed, the Constant speed (load varying) method and the Constant Loading method.

Constant speed method (British method)

The constant speed method is a load varying method, often better known as the British method. The set up for this test is the same as for a resistance test, which means that the model is connected to a resistance dynamometer (as indicated in Figure 3) that measures the actual resistance during the test. When performing the self-propulsion test with this method, the model speed and desired propeller loading should be selected before each run, and the corresponding propeller thrust should be estimated. [20]

Constant loading method (Continental method)

The constant loading method, also known as the continental method, requires a different set up than the one used for the resistance test and the constant speed test. This method introduces a tow force on the model, and the setup is shown in Figure 7 . The tow force should be computed before each run, and tuned such that it corresponds to the skin friction difference between model and full scale. The test starts with the model being accelerated simultaneously as the propeller rate of revolutions are increased. When the model has reached the target speed, the propulsion system should (together with the applied tow force) propel the model freely at the same speed as the towing carriage. Measurements are started when a steady state is achieved. [20]

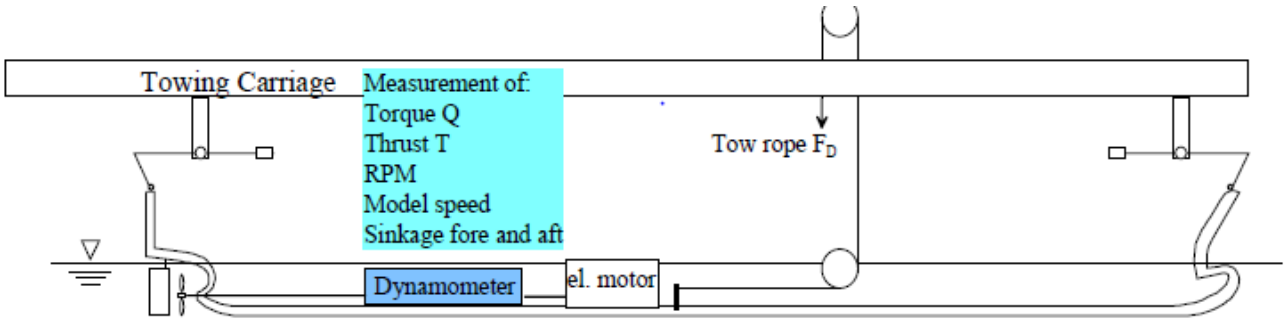

Figure 7 Propulsion Test Setup for Constant Loading Method [19]

Advantages and Disadvantages of Two Methods

Both tests have their advantages and disadvantages. The load varying test requires several load varied tests for each speed, which obviously requires more time in the towing tank than the constant loading method which only needs one run for each speed. This makes the constant loading method cheaper to perform, and this is the reason why the constant loading method is the most used method today Thus it then seems little attractive to use more time and money on performing the load varying method, it also has an advantage over the constant loading method

when it comes to using the results afterwards. As it has recordings for several loading conditions at each speed, it is easy to re-scale the results to different scaling ratios and different powering performance methods later. [19]

2.3.2. Analysis of Propulsion Test Results

The following measured data can be determined as non-dimensional characteristics of the model propeller that can be plotted in the traditional open water chart as shown in Figure 6.

- Speed (V_A)
- $F_{carriage}$ (N)
- Thrust (T_M)
- Torque (Q_M)
- Propeller revolutions (n)
- Water temperature (T_W)

The non-dimensional coefficients can be determined in the self-propulsion test. K_{TM}, K_{QM} and J_M are calculated in the same manner as the open water test by using Equations (8), (9) and (10). They are used to estimate the change in propeller performance from a homogeneous to non-homogeneous inflow field in effect due to the wake.

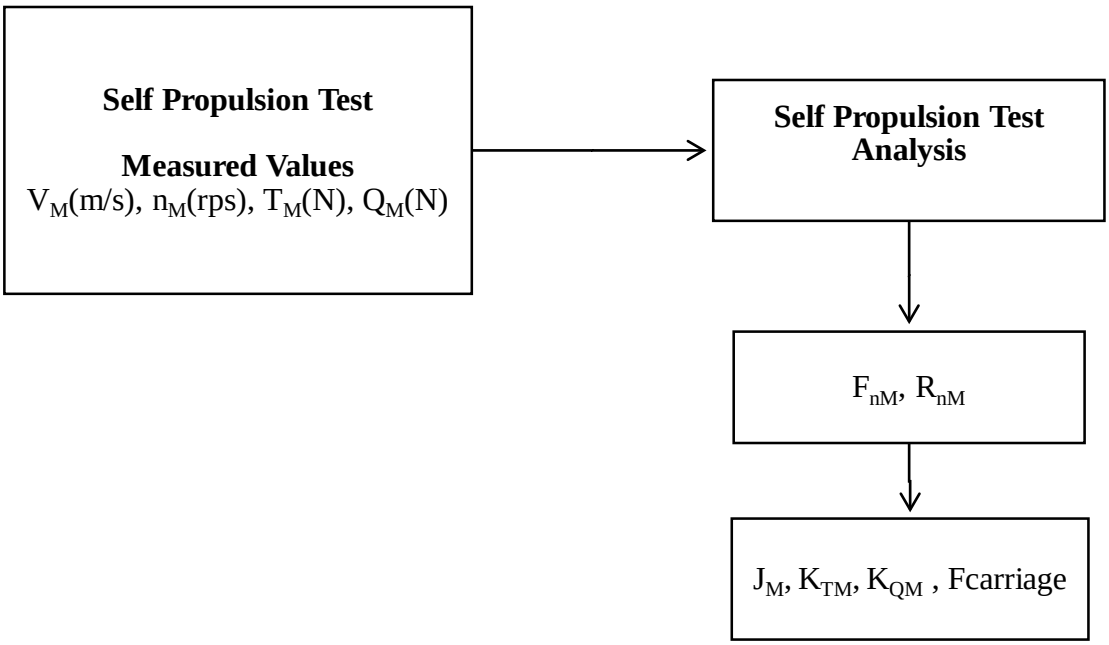

Figure 8 Flow Chart of Self Propulsion Test Analysis [17]

The evaluation of the propulsion test requires the resistance characteristics and the open-water characteristics of the stock propeller. There are two approaches:

1. 'Thrust Identity' Approach

The propeller produces the same thrust in a wake field of wake fraction w as in open-water with speed $V_S(1- w)$ for the same rpm, fluid properties etc.

2. 'Torque Identity' Approach

The propeller produces the same torque in a wake field of wake fraction w as in open-water with speed $V_S(1- w)$ for the same rpm, fluid properties etc.

ITTC standard is the 'thrust identity' approach. We described the details procedure for the ITTC 1978 performance prediction method. [18]

2.4. ITTC 1978 Performance Prediction Method (IPPM78)

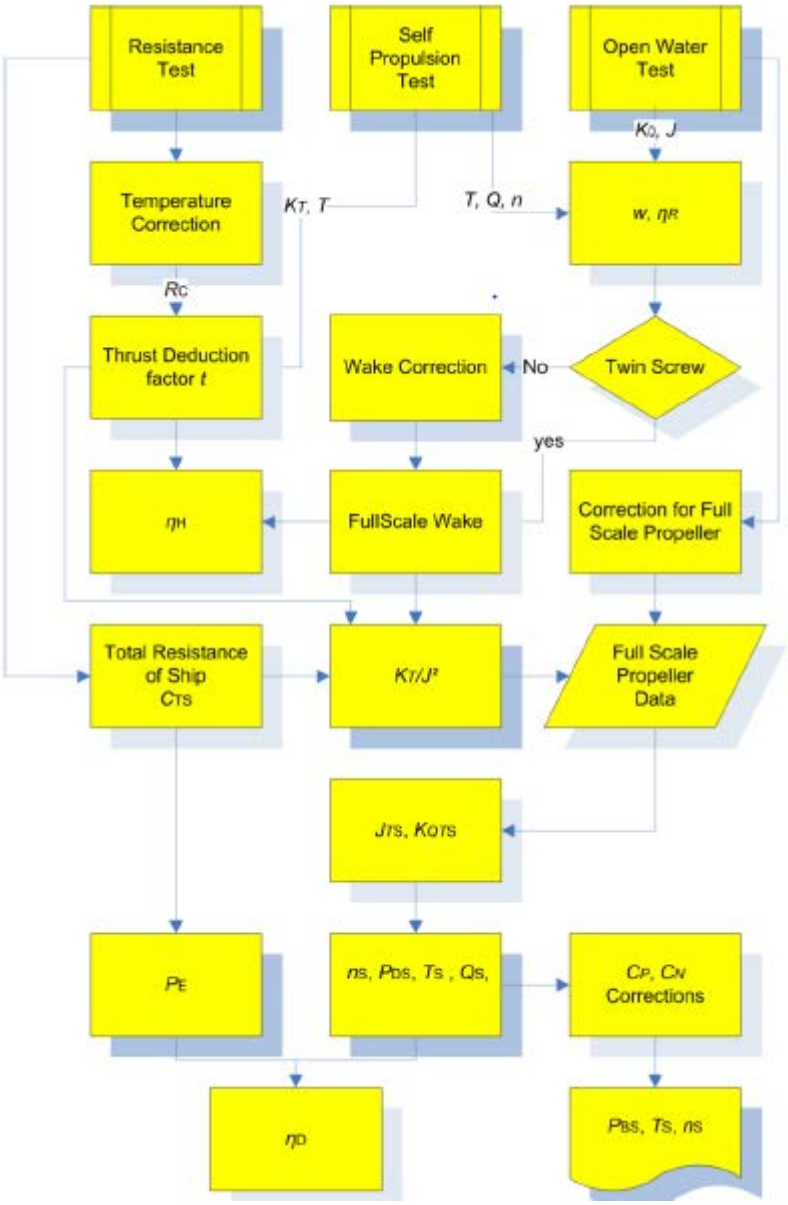

Figure 9 ITTC 1978 Service Performance Prediction Procedure [21]

The ITTC 1978 performance prediction method (IPPM78) has become a widely accepted procedure to evaluate model tests. It combines various aspects of resistance, propulsion, and open-water tests. The IPPM78 assumes that the following tests have been performed yielding the corresponding results [18]:

Resistance test $R_{TM} = f(V_M)$

Open-water test $T_M = f(V_{AM}, n_M)$

$Q_M = f(V_{AM}, n_M)$

Propulsion test $T_M = f(V_M, n_M)$

$Q_M = f(V_M, n_M)$

Figure 9 ITTC 1978 Service Performance Prediction Procedurean overview of how the entire procedure are built up, and what that is extracted from the different parts. When the tests are done, an extrapolation procedure is used to give a full scale prediction.

2.4.1. Thrust Identity Principle

The results of the analysis from each test are inputs to the performance prediction analysis. The load-varying method requires the interpolation of the self-propulsion point. The method used here involves first plotting the non-dimensionless thrust coefficients at different propeller revolutions from the self-propulsion test against the towing carriage force. At the point where F_D is projected to this curve, we read the thrust coefficient at that point according to thrust identity principle. From that thrust coefficient, we noted that value of thrust T_M, and torque Q_M, measured in the self-propulsion tests and then these values are expressed in the non-dimensional forms as in the procedure for propulsion test.

$$K_{TM} = \frac{T_M}{\rho_M D_M^4 n_M^2} \; and \; K_{QM} = \frac{Q_M}{\rho_M D_M^5 n_M^2}$$

Thrust identity is assumed, i.e. K_{TM} (Self-Propulsion Test) = K_{TM} (Open Water Test).

Using thrust identity with K_{TM} as input data, J_{TM} and K_{QTM} are read off from the model propeller open water diagram, and the corresponding wake fraction and the relative rotative efficiency can be calculated by following Equations (12) and (13):

$$w_{TM} = 1 - \frac{J_{TM} D_M n_M}{V_M} \tag{11}$$

$$\eta_R = \frac{K_{QTM}}{K_{QM}} \tag{12}$$

where, V_M is model speed

The thrust deduction is obtained from Equation (14) :

$$t = \frac{T_M + F_D - R_C}{T_M} \tag{13}$$

where F_D is the towing force actually applied in the propulsion test. R_C is the resistance corrected for differences in temperature between resistance and self-propulsion tests:

$$R_C = \frac{(1+k).C_{FMC} + C_R}{(1+k).C_{FM} + C_R} \tag{14}$$

where C_{FMC} is the frictional resistance coefficient at the temperature of the self-propulsion test. The thrust deduction factor and the relative rotative efficiency are equal in model and full scale, hence the scaling effects will be taken into account on all the other coefficients. [21]

2.4.2. Full Scale Correction for Total Resistance Coefficient of Ship

The extrapolation of the resistance test results to full scale will be performed according to ITTC 2014 Procedure, analysis of the model scale values from resistance test were already described in *Sub-section 2.1.1*.

The total resistance coefficient of a ship without bilge keels is

$$C_{TS} = (1+k)C_{FS} + \Delta C_F + C_A + C_R + C_{AAS} \tag{15}$$

where

- k is the form factor determined from the resistance test, see ITTC standard procedure 7.5-02-02-01.
- C_{FS} is the frictional resistance coefficient of the ship according to the ITTC1957 model-ship correlation line
- C_R is the residual resistance coefficient calculated from the total and frictional resistance coefficients of the model in the resistance tests:

$$C_R = C_{TM} - (1+k)C_{FM} \tag{16}$$

- ΔC_F is the roughness allowance:

$$\Delta C_F = 0.044\left[\left(\frac{k_S}{L_{WL}}\right)^{\frac{1}{3}} - 10.Re^{-\frac{1}{3}}\right] + 0.000125 \tag{17}$$

where k_S indicates the roughness of hull surface. When there is no measured data, the standard value of k_S=150x10^{-6} m can be used. For modern coating different value will have to be considered.

- C_A is the correlation allowance

C_A is determined from comparison of model and full scale trial results. When using the roughness allowance as above, the 19th ITTC recommended using

$$C_A = (5.68 - 0.6logRe).10^{-3} \quad (18)$$

to give values of $\Delta C_F + C_A$ that approximates the values of ΔC_F of the original 1978 ITTC method. It is recommended that each institution maintains their own model-full scale correlation.

- C_{AAS} is the air resistance coefficient in full scale

$$C_{AAS} = C_{DA}\frac{\rho_A.A_{VS}}{\rho_S.S_S} \quad (19)$$

where, A_{VS} is the projected area of the ship above the water line to the transverse plane

S_S is the wetted surface area of the ship

ρ_A is the air density

C_{DA} is the air drag coefficient of the ship above the water line. Values of CDA are typically in the range 0.5-1.0, where 0.8 can be used as a default value. [21]

2.4.3. Scale Effect Corrections for Propeller Characteristics

In this subsection, we performed scale effect corrections of model propeller open water to the propeller performance in full scale. The propulsion system must be scaled in order to estimate the required power for the full scale ship.

The characteristics of the full-scale propeller are calculated from the model characteristics as follows (ITTC 2014) [21] :

$$K_{TS} = K_{TM} - \Delta K_T \quad (20)$$

$$K_{QS} = K_{QM} - \Delta K_Q \quad (21)$$

where K_{TM} is the model scale thrust

K_{QM} is the model scale torque

ΔK_T is a thrust factor difference between model and full scale, calculated according to Equation (23)

ΔK_Q is a thrust factor difference between model and full scale, calculated according to Equation (24)

$$\Delta K_T = -\Delta C_D . 0.3 . \frac{P}{D} . \frac{c.Z}{D} \tag{22}$$

$$\Delta K_Q = \Delta C_D . 0.25 . \frac{c.Z}{D} \tag{23}$$

where P is propeller pitch

D is propeller diameter

Z is number of propeller blades

c is the chord length

ΔC_D is the change in the profile resistance coefficient of the propeller blades, calculated according to Equation (25) by using Equations (26) and (27).

$$\Delta C_D = C_{DM} - C_{DS} \tag{24}$$

$$C_{DM} = 2\left(1 + 2\frac{t}{c}\right)\left[\frac{0.044}{(Re_{c0})^{\frac{1}{6}}} - \frac{5}{(Re_{c0})^{\frac{2}{3}}}\right] \tag{25}$$

$$C_{DS} = 2\left(1 + 2\frac{t}{c}\right)(1.89 + 1.62 . log\frac{c}{k_p}) \tag{26}$$

where, c is the chord length

t is the maximum thickness

P/D is the pitch ratio

k_P denotes the blade roughness, the standard value of which is set $k_P=30x10^{-6}$ m

Re_{c0} is the local Reynolds number with Kempf's definition at the open-water test

They are defined for the representative blade section, such as at r/R = 0.75.

Reynolds Number of propeller based on chord length 0.7 R

$$Re_{0.7} = \frac{c_{0.7}\sqrt{V_A^2 + (0.7\pi nD)^2}}{\nu} \tag{27}$$

where, $c_{0.7}$ is chord length at 0.7R (m)

V_A is speed of advance of the model propeller (m/s)

n is rate of revolutions of the model pro-peller (rps)

D is model propeller diameter (m)

υ is kinematic viscosity (m^2/s)

2.4.4. Scale Corrections for Full Scale Wake and Operating Condition of Propeller

The full-scale wake is calculated by the following formula using the model wake fraction w_{TM}, and the thrust deduction fraction (t) obtained as the analysed results of self-propulsion test [21],

$$w_{TS} = (t + w_R) + (w_{TM} - t - w_R)\frac{(1+k)C_{FS} + \Delta C_F}{(1+k)C_{FM}} \tag{28}$$

where w_R stands for the effect of rudder on the wake fraction. If there is no estimate for w_R, the standard value of 0.04 can be used.

If the estimated w_{TS} is greater than w_{TM}, w_{TS} should be set as w_{TM}.

A curve for the parameter K_T/J^2 as function of J is introduced in the open water diagram for the full-scale ship. The design point is can be defined as Equation (30).

The load of the full-scale propeller is obtained from

$$\frac{K_T}{J^2} = \frac{1}{N_P}.\frac{S_S}{2D_S^2}.\frac{C_{TS}}{(1-t).(1-w_{TS})^2} \tag{29}$$

where N_P is the number of propellers.

By plotting K_T/J_2 curve on the full scale open water chart, full scale advance coefficient J_{TS} and the torque coefficient K_{QTS} are read off from the full scale propeller characteristics when K_T/J_2 curve intersects with the thrust coefficient curve and the following quantities are calculated,

1. The rate of revolutions (r/s):

$$n_s = \frac{(1-w_{TS}).V_S}{J_{TS}.D_S} \tag{30}$$

2. Delivered power of the propeller (kW):

$$P_{DS} = 2\pi\rho_S D_S^5 n_S^3 \frac{K_{QTS}}{\eta_R}.10^{-3} \tag{31}$$

3. Thrust of the propeller (N):

$$T_S = \left(\frac{K_T}{J^2}\right).J_{TS}^2\rho_S D_S^4 n_S^2 \tag{32}$$

4. Torque of the propeller (Nm) :

$$Q_S = \frac{K_{QTS}}{\eta_R}.\rho_S D_S^5 n_S^2 \tag{33}$$

5. Effective power (kW) :

$$P_E = C_{TS}.\frac{1}{2}\rho_S V_S^3 S_S.10^{-3} \tag{34}$$

6. Quasi propulsive efficiency:

$$\eta_D = \frac{P_E}{N_P.P_{DS}} \tag{35}$$

7. Hull efficiency:

$$\eta_H = \frac{1-t}{1-w_{TS}} \tag{36}$$

2.5. Computational Fluid Dynamics (CFD)

In order to evaluate the powering performance, the propeller design and propulsion parameters of a ship, we do the traditional model tests for resistance test, open water test and self-propulsion test. With the rapid advances in the field of computational fluid dynamics (CFD) and high-performance computing (HPC), numerical simulations of ship self-propulsion have recently gained increasing attention. Computational fluid dynamics (CFD) are becoming an increasingly important way for propeller tests in the propeller pre-design phase. Because CFD takes the advantages of powerful modern computers and make the CPU consuming, numerical time-domain simulations of flow around propellers.

Computational fluid dynamics, CFD, utilizes the governing partial differential equations (PDEs) of fluid motion with the method of discretized algebraic equations that approximate these PDEs. The equations are then numerically solved and can apply to a wide variety of flow problems. This can be simplified as the simulation and analysis of fluid flows, thereby including heat and mass transfer and chemical reactions and much more, using computational resources.(Keon-Je & Shin-Hyoung 1995 [22] ; Rhee & Joshi 2006 [23])

Important advantages with this technique are the possibility of savings in both cost and time for industries using CFD as a tool that complements the experimental and theoretical work in fluid dynamics. (Munson et al. 2013) [24]

We can generally describe the workflow of CFD simulations as following three main steps; pre-processing, solving and post-processing.

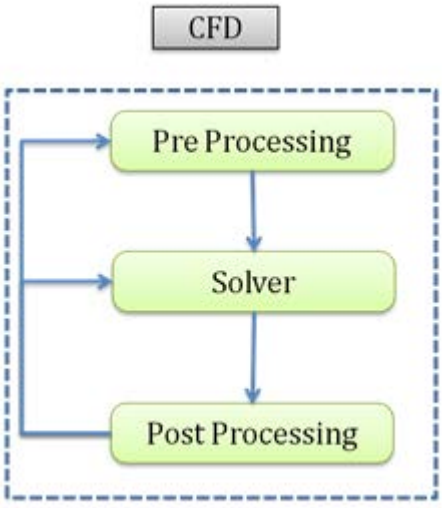

Figure 10 Workflow Chart of CFD Simulations (https://www.learncax.com/knowledge-base/blog/by-category/cfd/introduction-to-cfd-part-ii-selecting-the-domain)

2.6. Governing Equations

Ship flows are governed by the three basic conservation laws for mass, momentum and energy, collectively referred to as the Navier–Stokes equations.

The first law is mass conservation law- continuity equation which states that the rate of change of mass in an infinitesimally small control volume equals the rate of mass flux through its bounding surface.

Mass conservation – Continuity equation,

$$\frac{\partial \rho}{\partial t} + \nabla.(\rho V) = 0 \tag{37}$$

where ∇ is the differential operator ($\partial/\partial x$, $\partial/\partial y$, $\partial/\partial z$)

ρ is water density (kg/m^3)

V = (u, v, w) , fluid velocity (m/s)

The momentum conservation law states that the rate of change of momentum for the infinitesimally small control volume is equal to the rate at which momentum is entering or leaving through the surface of the control volume, plus the sum of the forces acting on the volume itself. The momentum equation is also known as the Navier-Stokes equation.

Momentum conservation – Momentum equation (Navier-Stokes equation),

$$\begin{aligned}
\frac{\partial(\rho u)}{\partial t} + \nabla.(\rho u V) &= -\frac{\partial p}{\partial x} + \frac{\partial \tau_{xx}}{\partial x} + \frac{\partial \tau_{yx}}{\partial y} + \frac{\partial \tau_{zx}}{\partial z} + \rho f_x \\
\frac{\partial(\rho v)}{\partial t} + \nabla.(\rho v V) &= -\frac{\partial p}{\partial y} + \frac{\partial \tau_{xy}}{\partial x} + \frac{\partial \tau_{yy}}{\partial y} + \frac{\partial \tau_{zy}}{\partial z} + \rho f_y \\
\frac{\partial(\rho w)}{\partial t} + \nabla.(\rho w V) &= -\frac{\partial p}{\partial z} + \frac{\partial \tau_{xz}}{\partial x} + \frac{\partial \tau_{yz}}{\partial y} + \frac{\partial \tau_{zz}}{\partial z} + \rho f_z
\end{aligned} \tag{38}$$

Where P is pressure (Pa)

τ_{ij} is viscous stresses (Pa)

f_i is body force (N)

The third law is the energy conservation law which states that the rate of change in internal energy in the control volume is equal to the rate at which enthalpy is entering, plus work done on the control volume by the viscous stresses.

Energy conservation – Energy equation,

$$\begin{aligned}\frac{\partial}{\partial t}\left[\rho\left(e+\frac{V^2}{2}\right)\right]+\nabla.\left[\rho\left(e+\frac{V^2}{2}\right)V\right]\\ =\rho q+\frac{\partial}{\partial x}\left(k\frac{\partial T}{\partial x}\right)+\frac{\partial}{\partial y}\left(k\frac{\partial T}{\partial y}\right)+\frac{\partial}{\partial z}\left(k\frac{\partial T}{\partial z}\right)-\frac{\partial(up)}{\partial x}-\frac{\partial(vp)}{\partial y}\\ -\frac{\partial(wp)}{\partial z}+\frac{\partial(u\tau_{xx})}{\partial x}+\frac{\partial\left(u\tau_{yx}\right)}{\partial y}+\frac{\partial(u\tau_{zx})}{\partial z}+\frac{\partial\left(v\tau_{xy}\right)}{\partial x}+\frac{\partial\left(v\tau_{yy}\right)}{\partial y}\\ +\frac{\partial\left(v\tau_{zy}\right)}{\partial z}+\frac{\partial(w\tau_{xz})}{\partial x}+\frac{\partial\left(w\tau_{yz}\right)}{\partial y}+\frac{\partial(w\tau_{zz})}{\partial z}+\rho f.V\end{aligned} \quad (39)$$

and $V^2 = V \cdot V$. [25]

2.7. Modeling

By means of accuracy and computational costs, various kinds of CFD solvers have their own advantages and disadvantages. Therefore, selection of relevant solvers for each case that can capture the necessary accurate results with minimum cost is crucial for every project. Figure 11 shows relation of CFD methods with their accuracy and computational time. [26]

When we do the numerical simulation for ship and propeller together, the flow in many cases is mainly turbulent because of the viscosity. At critical Reynolds number the flow transits from laminar to turbulent. The turbulent flow displays a chaotic and unpredictable flow field consisting of eddies of various length scales. Because of the chaotic behavior it is nearly impossible to predict the flow around a body. [27]

Turbulence is a flow regime that is irregular, random and characterized by chaotic changes and includes low momentum diffusion, high momentum convection and rapid variation in space and time. There are several models to simulate turbulence via Direct Numerical Simulation (DNS), Large Eddy Simulation (LES) or based on Reynolds-Average Navier-Stokes (RANS) methods. [28]

LES requires a large number of time steps to derive a statistically valid solution and a very fine mesh for the boundary layer, whereas DNS introduces an extremely large increase in mesh resolution and a very small time step. In practice, zonal approaches, such as detached eddy simulation (DES), provide a reasonable compromise through use of a suitable wall boundary layer turbulence closure and application of an LES model through use of a suitable switch in separated flow regions [29].

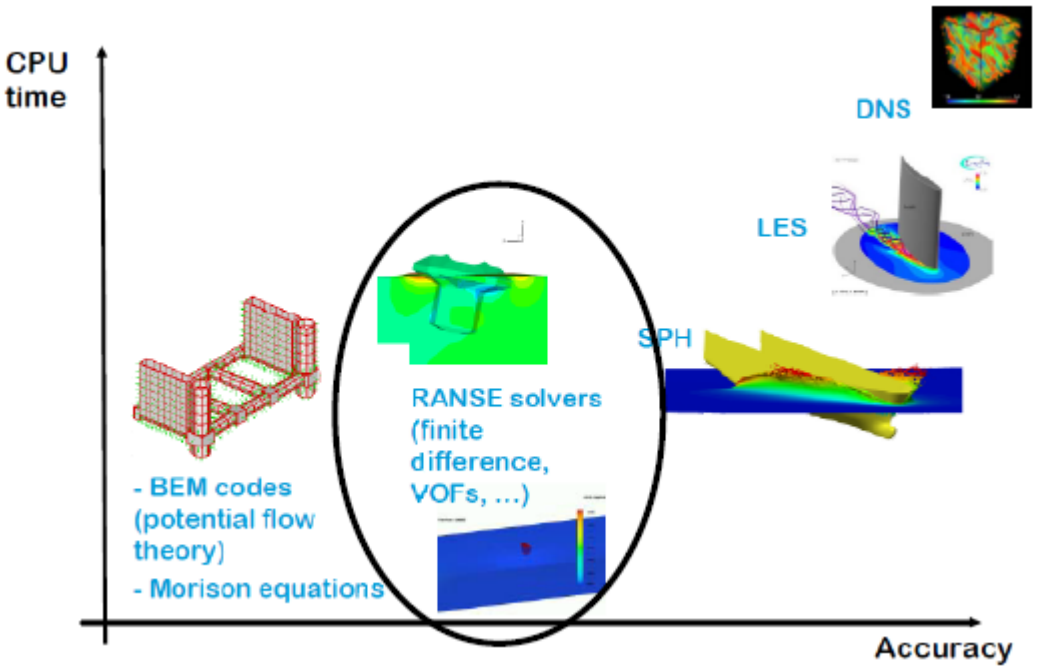

Figure 11 Available CFD methods with their accuracy and CPU time [26]

The RANS approach is based on complete averaging of Navier-Stokes equations and the flow characteristics, such as the velocity and pressure, are represented as a sum of averaged and fluctuating values. The turbulent stresses are modeled by one or another turbulence model. [30] Typically, propeller flows are turbulent but it is not practicable to resolve all the turbulent scales, thus it is common in computational fluid dynamics to utilize some form of turbulence modeling. Perhaps the most prevalent models are Reynolds-Averaged Navier-Stokes (RANS) models which only solve for the mean flow and use a turbulence model to estimate the effects of the turbulent fluctuations on the mean flow. RANS solutions are a good compromise between accuracy and computational requirements and have consequently been chosen for the study in this project. [31] The other models like DNS and LES are computationally very costly.

2.7.1. Incompressible Reynolds Averaged Navier–Stokes Equations - RANS

RANS is a modeling approach to predict turbulent flows by averaging (time or ensemble averaging) the Navier-Stokes equations. [28] In this method, the flow is considered as incompressible, which simplifies Equations (38) and (39) and removes the need to solve Equation (40). The Reynolds averaging process assumes that the three velocity components can be represented as a rapidly fluctuating turbulent velocity around a slowly varying mean velocity. This averaging process introduces six new terms, known as Reynolds stresses. These represent the increase in effective fluid velocity due to the presence of turbulent eddies within the flow. [25]

By introducing averaged and fluctuating components, for example, a velocity U_i may be divided into an average component,$\overline{U}_\iota$and a time varying component,u_i

$$U_i = \overline{U}_\iota + u_i \tag{40}$$

The averaged component is given by

$$\overline{U}_\iota = \frac{1}{\Delta t}\int_t^{t+\Delta t} U_i \, dt \tag{41}$$

where Δt is a time scale that is large relative to the turbulent fluctuations, but small relative to the time scale to which the equations are solved. For compressible flows, the averaging is actually weighted by density (Favre-averaging), but for simplicity, the following presentation assumes that density fluctuations are negligible.

For transient flows, the equations are ensemble-averaged. This allows the averaged equations to be solved for transient simulations as well. The resulting equations are sometimes called URANS (Unsteady Reynolds Averaged Navier-Stokes equations).

Substituting the averaged quantities into the governing equations results in the Reynolds averaged equations given below;

$$\frac{\partial \rho}{\partial t} + \frac{\partial}{\partial x_j}(\rho U_j) = 0 \tag{42}$$

$$\frac{\partial \rho U_i}{\partial t} + \frac{\partial}{\partial x_j}\left(\rho U_i U_j\right) = -\frac{\partial p}{\partial x_i} + \frac{\partial}{\partial x_J}\left(\tau_{ij} - \rho\overline{u_\iota u_J}\right) + S_M \tag{43}$$

where τ is the molecular stress tensor (including both normal and shear components of the stress). In the above equations, the bar is dropped for averaged quantities, except for products of fluctuating quantities. The continuity equation has not been altered but the momentum and scalar transport equations contain turbulent flux terms additional to the molecular diffusive fluxes. These are the Reynolds stresses, $\rho\overline{u_\iota u_J}$. [32]

There is one additional stress called Reynolds stresses, and it has to be determined. The process of specifying Reynolds stresses is called turbulence model or turbulence closure. In order to close this system of equations, a turbulence model has to be introduced that can be used to represent the interaction between these Reynolds stresses and the underlying mean flow. It is in the appropriate choice of the model used to achieve turbulence closure that many of the uncertainties arise. Wilcox [33] discusses the possible approaches that range from a simple empirical relationship which introduces no additional unknowns to those which require six or more additional unknowns and appropriate auxiliary equations.

2.7.2. Turbulence Models

Modeling of the components of the Reynolds stress tensor is rather complicated, because it requires detailed and usually unavailable information about the turbulent structures in the flow. Besides, the components do not only depend on the physical properties of the fluid, but also on the local conditions of the flow like velocity, geometry, surface roughness and upstream history. [32]

The Reynolds stress term in de RANS equations has to be determined with use of a turbulence model. The most used RANS turbulence models are classified on the basis of the number of transport equations that are solved together with the RANS equations. [34] There are five classes of turbulence models [35]:

- Zero-equation models
- One-equation models
- Two-equation models
- Algebraic stress models
- Reynolds stress models

One particular turbulence model capable of capturing all possible flows and conditions still has to be developed. Some models work well in certain type of flows, while others perform better in other conditions. In this thesis, two equation SST (Shear Stress Transport) k-ω turbulence model is chosen for turbulence closure.

The k-ω turbulence models represent a group of two-equation turbulence models in which the transport equation are solved for the turbulent kinetic energy k and its specific dissipation rate ω. This model is the most commonly used turbulence models in numerical propeller simulations. The k-ω SST model is known for predicting a more accurate ship wake.

The advantages of this model are seen in its ability to handle simultaneously lower-Re and higher-Re zones in the flow, and to predict more accurately non equilibrium regions in the boundary layer with adverse pressure gradients such as observed when separation occurs. The above considerations are important when modeling model scale propellers, model and full scale propellers operating at heavy loading. One can also expect more adequate location of vortical structures such as leading edge vortex and tip vortex. When considering the predicted ship's resistance there usually is a difference of about 3% between the predicted values, where the k-ω SST model predicts lower resistance values. In order to get a better understanding of this turbulence model, the basic assumptions in turbulence modelling and the main working principles of turbulence model are briefly explained. [36] [37] [38]

The k-ε model is less sensitive to the free stream value turbulence properties while the k-ω model tends to depend on free-stream turbulence properties. The k-ω model does not require any damping functions while the k-ε requires complex nonlinear damping functions for near wall-modifications. Since the two models have different strengths and weaknesses, a hybrid model was developed by Menter [39] to combine the most accurate regimes of the two models. That resulted in the two equation eddy viscosity SST k-ω model. In the model, the k-ω model is used in the near wall region and transforms to a k-ε far from the wall in the fully turbulent region. With the ability to combine the strengths of the k-ω and the k-ε respectively, the SST k-ω becomes an appropriate choice for adverse pressure gradients. [38]

The k equation in Wilcox's [40] two equation k-ω model reads:

$$\frac{\partial(\rho k)}{\partial t}+\frac{\partial(\rho U_j k)}{\partial x_j}=\frac{\partial}{\partial x_j}\left[\left(\mu+\frac{\mu_t}{\sigma_{k1}}\right)\frac{\partial k}{\partial x_j}\right]+P_k-\beta^*\rho k\omega \tag{44}$$

and ω the equation:

$$\frac{\partial(\rho\omega)}{\partial t}+\frac{\partial(\rho U_j \omega)}{\partial x_j}=\frac{\partial}{\partial x_j}\left[\left(\mu+\frac{\mu_t}{\sigma_{\omega1}}\right)\frac{\partial \omega}{\partial x_j}\right]+\alpha_1\frac{\omega}{k}P_k-\beta_1\rho\omega^2 \tag{45}$$

The turbulent viscosity is defined

$$v_t=\frac{\mu_t}{\rho}=\frac{k}{\omega} \tag{46}$$

and the Reynolds stresses in the production term P_k are calculated using the Boussinesq assumption, i.e. turbulent viscosity is introduced to model the Reynold's stresses:

$$-\overline{u_i' u_j'}=v_t\left(\frac{\partial U_i}{\partial x_j}+\frac{\partial U_j}{\partial x_i}\right)-\frac{2}{3}\delta_{ij}(k+v_t\frac{\partial U_k}{\partial x_k}) \tag{47}$$

The k-ε is transformed to a k-ω model using the turbulence frequency, defined $\omega = \varepsilon/k$, as a second variable and the length scale is $l = sqrt(k)/\omega$. The k equation in the transformed k-ε model reads:

$$\frac{\partial(\rho k)}{\partial t}+\frac{\partial(\rho U_j k)}{\partial x_j}=\frac{\partial}{\partial x_j}\left[\left(\mu+\frac{\mu_t}{\sigma_{k2}}\right)\frac{\partial k}{\partial x_j}\right]+P_k-\beta^*\rho k\omega \tag{48}$$

and ω the equation:

$$\frac{\partial(\rho\omega)}{\partial t}+\frac{\partial(\rho U_j \omega)}{\partial x_j}=\frac{\partial}{\partial x_j}\left[\left(\mu+\frac{\mu_t}{\sigma_{\omega2}}\right)\frac{\partial \omega}{\partial x_j}\right]+2\rho\frac{1}{\sigma_{\omega2}\omega}\frac{\partial k}{\partial x_j}\frac{\partial \omega}{\partial x_j}+\alpha_2\frac{\omega}{k}P_k-\beta_2\rho\omega^2 \tag{49}$$

The k equation in the standard SST k-ω model, with buoyancy term disregarded, reads:

$$\frac{\partial(\rho k)}{\partial t}+\frac{\partial(\rho U_j k)}{\partial x_j}=\frac{\partial}{\partial x_j}\left[\left(\mu+\frac{\mu_t}{\sigma_{k3}}\right)\frac{\partial k}{\partial x_j}\right]+P_k-\beta^*\rho k\omega \tag{50}$$

where the production term is defined

$$P_k=(2v_t s_{ij}s_{ij}-\frac{2}{3}k\frac{\partial v_i}{\partial x_j}\delta_{ij}) \tag{51}$$

ω the equation reads:

$$\frac{\partial(\rho\omega)}{\partial t}+\frac{\partial(\rho U_j\omega)}{\partial x_j}=\frac{\partial}{\partial x_j}\left[\left(\mu+\frac{\mu_t}{\sigma_{\omega3}}\right)\frac{\partial\omega}{\partial x_j}\right]+(1-F_1)2\rho\frac{1}{\sigma_{\omega2}\omega}\frac{\partial k}{\partial x_j}\frac{\partial\omega}{\partial x_j}+\alpha_3\frac{\omega}{k}P_k-\beta_3\rho\omega^2 \tag{52}$$

where the blending function F_1 is defined as

$$F_1=\tanh(\xi^4) \tag{53}$$

with

$$\xi=\min[\max\left\{\frac{\sqrt{k}}{\beta^*\omega y},\frac{500v}{y^2\omega}\right\}\frac{4\rho k}{CD_{k\omega}\sigma_{\omega2}y^2}] \tag{54}$$

and

$$CD_{k\omega}=\max\{2\rho\frac{1}{\sigma_{\omega2}\omega}\frac{\partial k}{\partial x_j}\frac{\partial\omega}{\partial x_j},1.10^{-10} \tag{55}$$

The turbulent viscosity is defined

$$v_t=\frac{\alpha_1 k}{\max(\alpha_1\omega,SF_2)} \tag{56}$$

and

$$F_2=\tanh(\eta^2) \tag{57}$$

with

$$\eta=\max\{\frac{2k^{1/2}}{\beta^*\omega y},\frac{500v}{y^2\omega}\} \tag{58}$$

Using a blending function the model transforms from a k-ω model to a k-ε model. Near the wall, F_1 = 1, the model behaves as a k-ω model but far from the wall, F_1 = 0, the model behaves as a k-ε model. The variable y is defined as the distance to the closest wall node. The constants

are a linear combination, $\Phi_3 = F_1 \Phi_1 + (1 - F_1) \Phi_2$, of the coefficients of the k-ω and k-ε models and are defined [38]:

$$\begin{aligned} \beta^* &= 0.09, \\ \alpha_1 &= {}^{5}/_{9} \\ \beta_1 &= 0.075, \\ \sigma_{k1} &= 2, \\ \sigma_{\omega 1} &= 2, \\ \alpha_2 &= 0.44, \\ \beta_2 &= 0.0828, \\ \sigma_{k2} &= 1, \\ \sigma_{\omega 2} &= 1/0.856 \end{aligned} \tag{59}$$

2.8. ANSYS CFX Solver

Removed due to Non-disclosure Agreement

Figure 12 Flow Chart of General Solution Used in ANSYS CFX [32]

ANSYS CFX uses a coupled solver, which solves the hydrodynamic equations (for *u*, *v*, *w*, *p*) as a single system. This solution approach uses a fully implicit discretization of the equations at any given time step. For steady-state problems, the time-step behaves like an 'acceleration parameter', to guide the approximate solutions in a physically based manner to a steady-state solution. This reduces the number of iterations required for convergence to a steady state, or to calculate the solution for each time step in a time-dependent analysis.

When solving fields in the CFX-Solver, the outer (or time step) iteration is controlled by the physical time scale or time step for steady and transient analyses, respectively. Only one inner (linearization) iteration is performed per outer iteration in steady-state analyses, whereas multiple inner iterations are performed per time step in transient analyses. [32]

2.9. Near Wall Y^+ Treatment

Turbulent flows are significantly affected by the presence of walls. The mean velocity field is affected through the no-slip condition that has to be satisfied at the wall. Very close to the wall, viscous damping reduces the tangential velocity fluctuations, while kinematic blocking reduces

the normal fluctuations. Toward the outer part of the near-wall region, however, the turbulence is rapidly augmented by the production of turbulence kinetic energy due to the large gradients in mean velocity. [30]

An important consideration when modeling turbulent boundary layers is the mesh resolution and the near-wall treatment of the chosen turbulence model. The reasoning behind this can be found by examining the structure of a turbulent boundary layer, which can be divided into two distinct layers, the inner and outer layer. When velocity and distance are normalized into wall units, u^+ and y^+ respectively, the inner layer is assumed to have the same velocity profile in every turbulent boundary layer. The wall units are defined as:

$$u^+ = \frac{u}{u_\tau}, y^+ = \frac{y u_\tau}{v} \tag{60}$$

where y is the distance away from the wall and u_τ is the friction velocity given by:

$$u_\tau = \sqrt{\frac{\tau_w}{\rho}} \tag{61}$$

The inner layer of the turbulent boundary layer can be subdivided into three sublayers. First, closest to the wall, is the viscous sublayer where turbulent eddies are limited in size by their proximity to the wall. The viscous sublayer extends of the region of ($0 \leq y^+ \leq 5$) and the velocity profile is given by:

$$u^+ = y^+ \tag{62}$$

Following the viscous sublayer is a buffer region where the velocity profile undergoes a transition from the viscous sublayer to the third and final sublayer within the inner layer known as the log-law region. The log-law region extends from approximately $y^+ = 30$ to the end of the inner layer (the size of which varies) and within this region, under the present assumptions, the velocity profile follows the relationship after which it is named, the log-law of the wall:

$$u^+ = \frac{1}{k} ln y^+ + A \tag{63}$$

where κ is Karman's constant whose value is the topic of much debate but is typically reported to lie in the region $0.38 \leq \kappa \leq 0{:}43$ and in engineering is most commonly taken as 0.41. Similarly A is not definitely determined, however a typical value is approximately 5.5. After the log-law region is the outer layer, which depends fully on the external flow.

The ANSYS CFX Solver basically uses three different wall functions: the standard wall functions, scalable wall functions and an automatic near wall treatment for ω based turbulence models. The first one is obsolete and only included for compatibility reasons. The second one uses a Low-Re number formulation when using a refined mesh, with $y^+ \leq 2$ to resolve the boundary layer. For $y^+ \geq 2$ wall functions are used until the ω treatment is blended into the k-ε. The automatic near wall treatment is used by default in the standard k-ω, baseline k-ε , SST and ω -Reynolds Stress models. Using the scalable wall function is only recommended if the viscous sub-layer can be neglected and also if $y^+ \geq 11{:}06$, which is the definition ANSYS CFX uses for the intersection between the viscous sub-layer and the log-law region. [32]

2.10. Numerical Discretization

Analytical solutions to the Navier-Stokes equations exist for only the simplest of flows under ideal conditions. To obtain solutions for real flows, a numerical approach must be adopted whereby the equations are replaced by algebraic approximations that can be solved using a numerical method. There are significant commonalities between the various governing equations and can be written in the following general form:

$$\underbrace{\frac{\partial(\rho\phi)}{\partial t}}_{\text{Rate of change term}} + \underbrace{div(\rho\phi\mathbf{u})}_{\text{Convective term}} = \underbrace{div(\Gamma grad\phi)}_{\text{Diffusive term}} + \underbrace{S_\phi}_{\text{Source term}} \tag{64}$$

where ϕ is the variable of interest , Γ is the diffusion coefficient. The above Equation is known as transport equation since it describes various transport processes of dependent variables. This equation represents different aspects of the fluid motion. The convection term represents the flux of ϕ convected by the mass flow rate ρU_j, the diffusion term represents the random motion of particles and the source term represents the generation and destruction of ϕ. The non-linear nature of the convective term makes it difficult to solve the equations directly, that is, as a set of simultaneous equations. An iterative solution method is the only way to solve these equations. The governing equations are discretised, that is, approximately linearised to obtain the algebraic equations and are solved at discrete points throughout the domain. [41]

In CFD, one important step is to represent and evaluate the partial differential equations to stable, consistent and accurate algebraic replacements. There are several method currently in use, such as the finite volume method (FV), finite element (FE) and finite difference (FD) method. [28] In this thesis, we used the ANSYS CFX solver to make the numerical simulations.

ANSYS CFX uses an element-based finite volume method (FV) to discretise the RANS equations, which first involves discretizing the spatial domain using a mesh. The mesh is used to construct finite volumes, which are used to conserve relevant quantities such as mass, momentum, and energy. [32]

2.10.1. Finite Volume Method

The finite volume method is probably the most discretization method used in CFD. This method draws on ideas from both finite element and the finite difference discretization techniques. In this approach the computational domain is discretized into finite control volumes also known as cells. The governing equations are integrated over each control volume which utilizes the conservation principles directly. The integral form of Equation over a control volume gives

$$\frac{\partial}{\partial t}\int_{CV}\rho\phi dV + \int_{A}\mathbf{n}\cdot(\rho\phi\mathbf{u})dA = \int_{A}\mathbf{n}\cdot(\Gamma grad\phi)dA + \int_{CV}S_{\phi}dV \qquad (65)$$

This equation represents the flux balance in a control volume where the left hand side represents the rate of change of ϕ and the net convective flux and right hand side gives the net diffusive flux and the generation or destruction of the property ϕ. These fluxes are evaluated by various numerical schemes.

The main advantage of the finite volume method is that the spatial discretization is carried out directly in the physical space. Thus, there are no problems with any transformation between coordinate systems, like in the case of the finite difference method. Compared to the finite difference method, another advantage of the finite volume method is that it is flexible to implement on both structured and unstructured grids. This makes finite volume method suitable for the treatment of flows in complex geometries. [41]

2.10.2. Meshing Generation

In previous section of this chapter, we have introduced the finite volume method. As we have observed, in order to analyze the fluid flow, the computational domains are split into subdomains and the discretized Navier-Stokes equations are solved inside of each cell. The process to approach appropriate grid called mesh generation. Mesh generation is an important step to work with CFD. It employs different algorithms to provide qualitative analyses of the fluid fields. The quality of the mesh plays important role when it comes to accuracy, stability

and the efficiency of the solution. [28] Classification of mesh type is often done by means of connectivity or element shapes used. Regarding connectivity this includes structured, unstructured or a hybrid mesh. Structured implies a regular connectivity with elements of rectangles or triangles (in 2D). Unstructured depends on irregular connections with various and unevenly shaped elements, while the hybrid mesh are a mix up of the two preceding. Element-based classification concerns the dimensions or types present; either for meshes generated in 2D or 3D. For a 3-dimensional case the most commonly used elements are hexahedral or tetrahedral. Figure 13 shows examples of 3D mesh elements. [42]

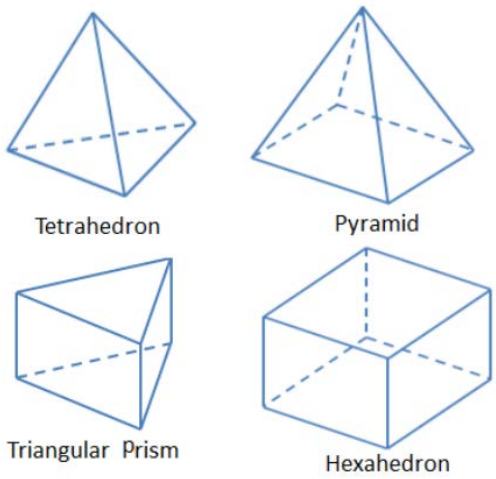

Figure 13 Various geometrically shaped 3D elements (Wikimedia commons 2015) [42]

Computation mesh is a discrete geometrical representation of computational water domain which will be divided into finite cells. These aforementioned domain boundaries are also parts of computation mesh. Many meshing methods begin with the mesh generations on the domain boundaries (surfaces) which enclosed the computational water domain. Surface mesh consists of many two-dimensional planar or curvilinear elements called faces. A face is comprised of vertices and edges. A volume mesh will be built from the surface mesh consisting of three-dimensional elements called cells. The density of faces on a domain boundary (i.e. the size of every faces and the distributions) depend on the boundary type, and will affect the CFD results. According to Figure 13 , there are different kinds of cell types in modern CFD codes, such as tetrahedron, hexahedron, pyramid, prism/wedge and polyhedron. With different cell types, the required computational efforts (such as time required for mesh generation, memory and time consumption during numerical solution, complexity of numerical solution algorithm, convergence speed) may significantly differ in a particular simulation. It is important to know all the advantages and limitations of all the cell types to choose an appropriate cell type in a simulation. [30] Table 1 shows the advantages and limitations of all types of mesh cells.

Table 1 Advantages and Limitations of All Types of Mesh Cells [36]

Removed due to Non-disclosure Agreement

2.11. Rotating Motion

There are a variety of engineering problems involving rotational parts. Consider a rotating propeller behind a ship, to compute the interaction between a propeller and hull the sliding interface is required to provide the exchange of information between non-matching parts of the cells. Another solution is to use reference frames Therefore, it is not feasible to perform the computation as steady by choosing a computational domain which rotates with the rotor or impeller. There are different approaches to solve these kinds of problems. In this thesis, we applied moving reference frame (MRF) and sliding mesh approaches. [43]

2.11.1. Multiple Reference Frame Model or Moving Refrence Frame MRF (Frozen Rotor)

The multiple reference frame model or MRF in which the flow is assumed steady and cell zones move at different rotational/translational speeds. The cells in the rotational domain are static and their positions don't have to be recalculated in each time step. It is the model of choice where the rotor-stator interaction is relatively weak or an approximation is required. It gives acceptable time-averaged consequences for many engineering problems. We can also model a problem with MRF to compute a flow field that can be used as initial condition of a transient sliding mesh calculation. [43] Steady-state flow conditions are assumed at the interface between the two reference frames. That is, the velocity at the interface must be the same (in absolute terms) for each reference frame. The grid does not move.

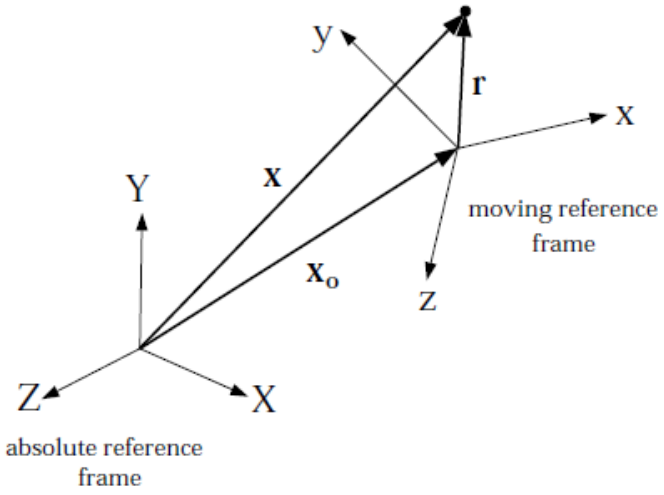

Figure 14 Coordinate System for Relative Velocity [44]

In MRF implementation, the computational domain is divided into two subdomains that can be assumed as rotating or translating according to the initial frame. The governing equations in each sub-domain are obtained on the sub-domain's reference frame. When the relative velocity formulation is used, velocities in each subdomain are computed relative to the motion of the subdomain. Velocities and velocity gradients are converted from a moving reference frame to the absolute inertial frame as described below. The position vector relative to the origin of the zone rotation axis is defined as

$$\vec{r} = \vec{x} - \overrightarrow{x_0} \tag{66}$$

Let $\vec{x}$ and $\overrightarrow{x_0}$ be the position of the absolute Cartesian coordinate system and the origin of the zone rotation axis respectively.

To obtain the absolute velocity, the relative velocity in the moving reference frame can be augmented to the velocity in the rotational zone using the following equation:

$$\vec{v} = \overrightarrow{v_r} + (\vec{\omega} \times \vec{r}) + \overrightarrow{v_t} \tag{67}$$

where $\vec{v}$ is the velocity in the absolute inertial reference frame, $\overrightarrow{v_r}$ is defined as the velocity in the relative reference frame and $\overrightarrow{v_t}$ is the translational velocity of non-inertial reference frame.

2.11.2. Sliding Mesh

The sliding mesh is a computational unsteady technique to model the CFD problems. It is performed, as the interaction between stator and rotor is strong and more accurate computation is desired. When a time-accurate solution for rotor-stator interaction (rather than a time-averaged solution) is desired, we must use the sliding mesh model to compute the unsteady flow field. The sliding mesh model is the most accurate method for simulating flows in multiple moving reference frames, but also the most computationally demanding.

Most often, the unsteady solution that is sought in a sliding mesh simulation is time-periodic. That is, the unsteady solution repeats with a period related to the speeds of the moving domains. In the sliding mesh technique two or more cell zones are used. Each cell zone is bounded by at least one "interface zone" where it meets the opposing cell zone. The interface zones of adjacent cell zones are associated with one another to form a grid interface. The two cell zones will move relative to each other along the grid interface.

During the calculation, the cell zones slide (i.e., rotate or translate) relative to one another along the grid interface in discrete steps. The sliding mesh model allows adjacent grids to slide relative to one another. In doing so, the grid faces do not need to be aligned on the grid interface. This

situation requires a means of computing the flux across the two non-conformal interface zones of each grid interface.

In the example shown in Figure 15, the interface zones are composed of faces A-B and B-C, and faces D-E and E-F. The intersection of these zones produces the faces a-d, d-b, b-e, etc. Faces produced in the region where the two cell zones overlap (d-b, b-e, and e-c) are grouped to form an interior zone, while the remaining faces (a-d and c-f) are paired up to form a periodic zone. To compute the flux across the interface into cell IV, for example, face D-E is ignored and faces d-b and b-e are used instead, bringing information into cell IV from cells I and III, respectively. [44]

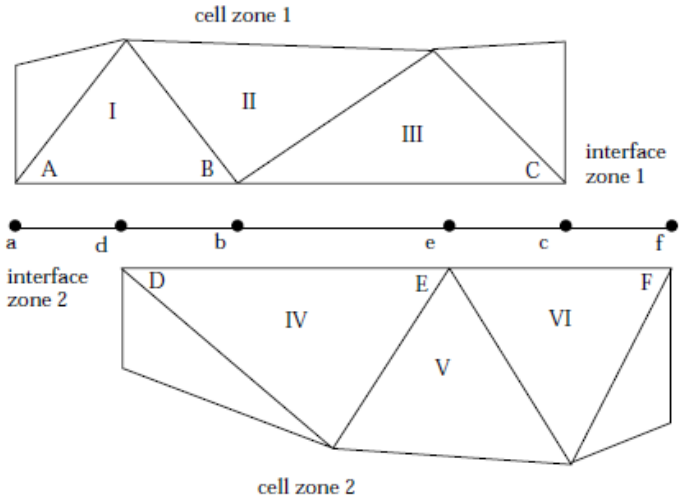

Figure 15 Two-Dimensional Grid Interface [44]

3. NUMERICAL PROPULSION SIMULATION IN MODEL SCALE

3.1. Workflow of Numerical Propulsion Simulation Procedure

The primary objective of this thesis is to investigate the propulsive efficiency and the hydrodynamics performance of the propeller behind the ship by changing the propeller position. In order to evaluate and investigate these results, we needed to perform the numerical propulsion simulation in model scale.

When propeller operates behind the hull form and then the fluid flow passed the hull form creating the wake behind the hull, the performance of propeller is changed because of the interaction with the hull. There are two ways to perform numerical test: full-scale test and model scale test. In this thesis, we performed the model scale numerical test for propulsion test. Morever, then we can extrapolate the propulsion results from the model scale to full scale results according to the ITTC 1978 Service Performance Prediction. As the experimental propulsion test is carried out with propeller, ship and rudder (the appendage), we also need to perform the numerical test with hull (including rudder) and propeller together. Therefore, it is necessary to make model of hull, propeller and rudder and simulate all together.

According to the work flow of numerical CFD technique as we mentioned in *Section 2.5*, the Pre-processing, Solving and Post-processing of numerical propulsion simulation has to be done. There are many steps in creating computational fluid dynamics simulations, each being typically performed with separate, specialized pieces of software. However, this is not always necessarily the case as some CFD packages are available that provide all the necessary tools to generate geometry, mesh the domain, solve the equations and post-process the results. [31]

MMG have the accessibility of ANSYS Product License to use ANSYS Workbench. In this thesis, the Pre-processing, Solving and Post-processing of numerical propulsion simulation will be done by using ANSYS Workbench.

The numerical propulsion simulation takes the viscous flow effects into account. Therefore, a commercial viscous flow solver, ANSYS CFX solver (RANS software package) will be used for the simulation. This solver is based on the discretization of finite volume method (FVM).

When we performed the numerical simulation, the numerical domain is divided into two domains: the ship domain and propeller domain. They will be modeled individually and separately. The ship domain is the rectangular tank domain which includes the hull, rudder and the cylindrical shape container. This cylindrical shape container was located at the propeller position behind the hull.

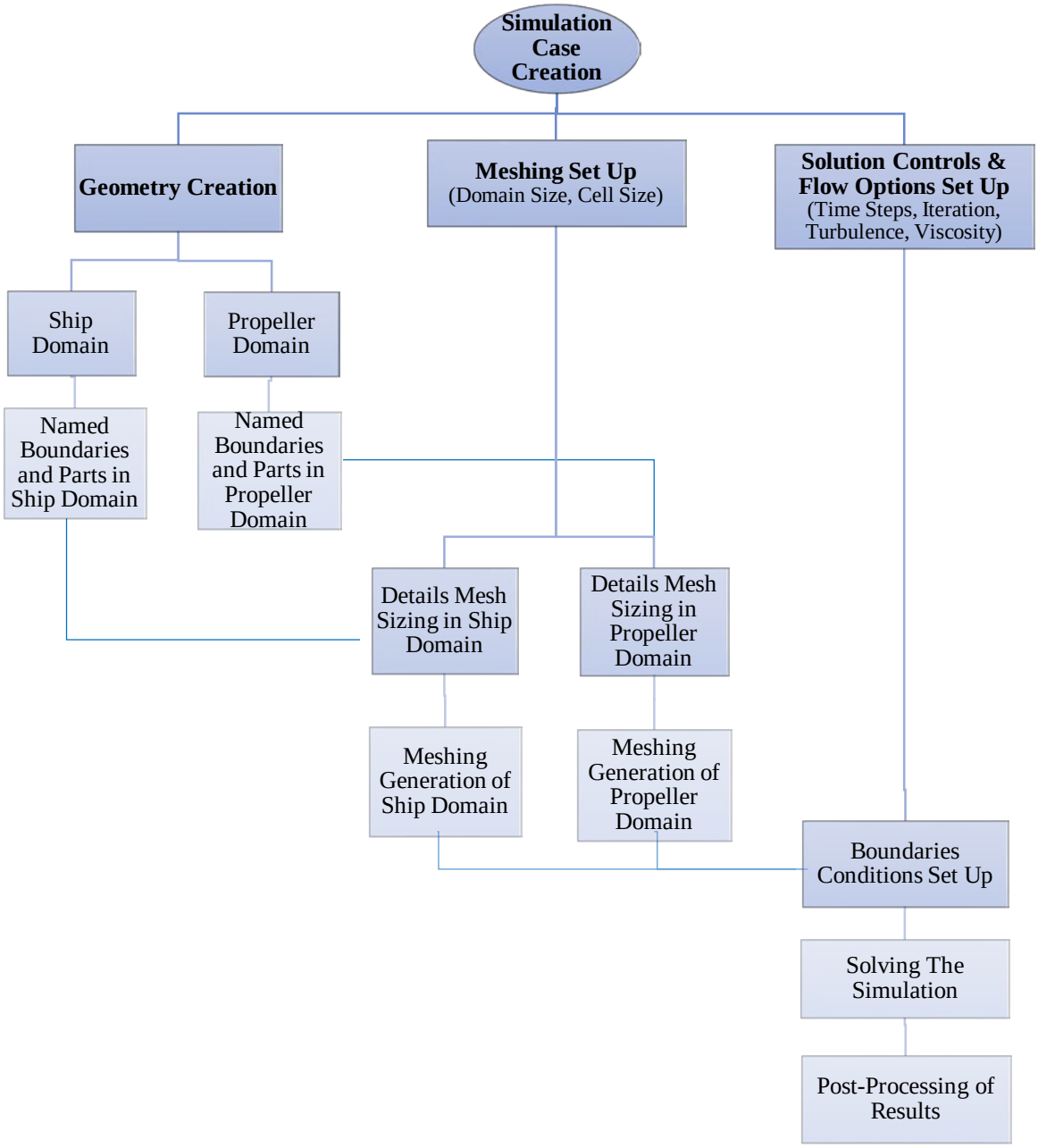

Figure 16 Workflow of Numerical Propulsion Simulation Procedure

The propeller domain is the cylindrical shape container that includes the propeller model. Therefore, these two domains will be combined to perform the simulation that means the mesh grid in the propeller domain rotates with the propeller revolution while the mesh grid in the ship domain remains the stationary. The simulation technique is used sliding mesh approach in order to accommodate this idea for two domains. The simulation will be done in unsteady condition (transient state). An unstructured tetrahedral grid with approximately 2.24 millions elements is used. The workflow plan for the numerical simulation is shown in Figure 16.

3.2. Test Data Description

This section deals with the main ship particulars and the propeller in full scale and model scale that used for numerical simulations in this thesis work. The vessel used as test data in this thesis work is the modern research and training vessel. The ship is equipped with the controllable pitch propeller (left handed). Experimentally, to model the full-scale ship, it is important to consider a model-scale vessel by reasonably small dimensions. The scale factor λ is considered small with inherent advantages of the accuracy experimental values. As a consequence, the model scale is manufactured corresponding scale factor λ equals to 10. [28] Main geometrical characteristics, full scale and model scale data, of the reference ship are presented in Table 2.

Table 2 Main Dimensions of Test Case Ship in Full Scale and Model Scale

Removed due to Non-disclosure Agreement

The CAD representations of the test case vessel in full scale are presented in Figure 17 and Figure 18.

Removed due to Non-disclosure Agreement

Figure 17 CAD Representation of Test Case Vessel in Full Scale(Profile View)

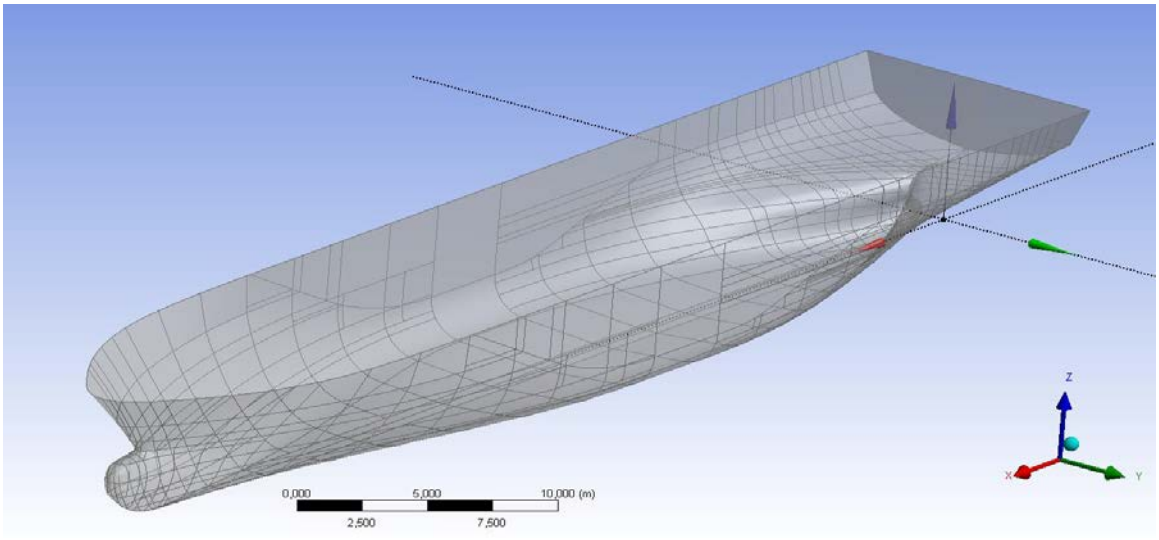

Figure 18 CAD Representation of Test Case Vessel in Full Scale(Perspective View)

The main dimensions of test case propeller in full scale and model scale are shown in Table 3 . This propeller is left-handed propeller with four blades. The CAD representations of the whole propeller in full scale are presented in Figure 19.

Table 3 Main Dimensions of Test Case Propeller in Full Scale and Model Scale

Removed due to Non-disclosure Agreement

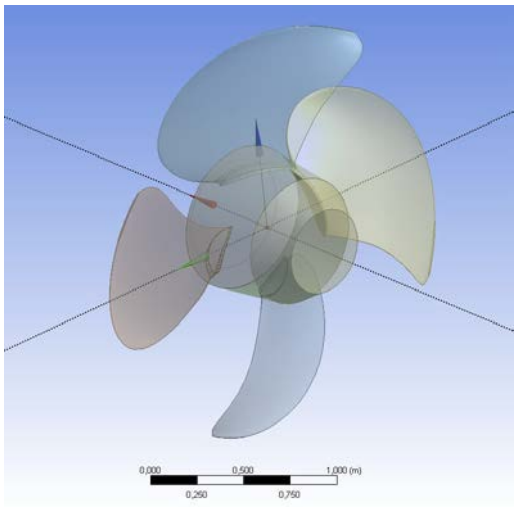

Figure 19 CAD Representation of Test Case Propeller in Full Scale in Perspective View

3.3. Geometry Creation of Computational Domains in DesignModeler

As mentioned in *Section 3.1*, the numerical propulsion simulation has two computational domains. The viscous flow computations are carried out with these computational domains. These domains can be named as ship domain and propeller domain. The ship domain is the stationary domain while the propeller domain is the rotatory domain. The geometry creation for each domain is described briefly below.

3.3.1. Computational Ship Domain Creation

In the computational ship domain, this domain includes the rectangular boxed-shape enclosure, ship hull, rudder and propeller cylinder. The non-dimensional domain dimensions of computational ship domain are as described below, and presented in Figure 20.

Removed due to Non-disclosure Agreement

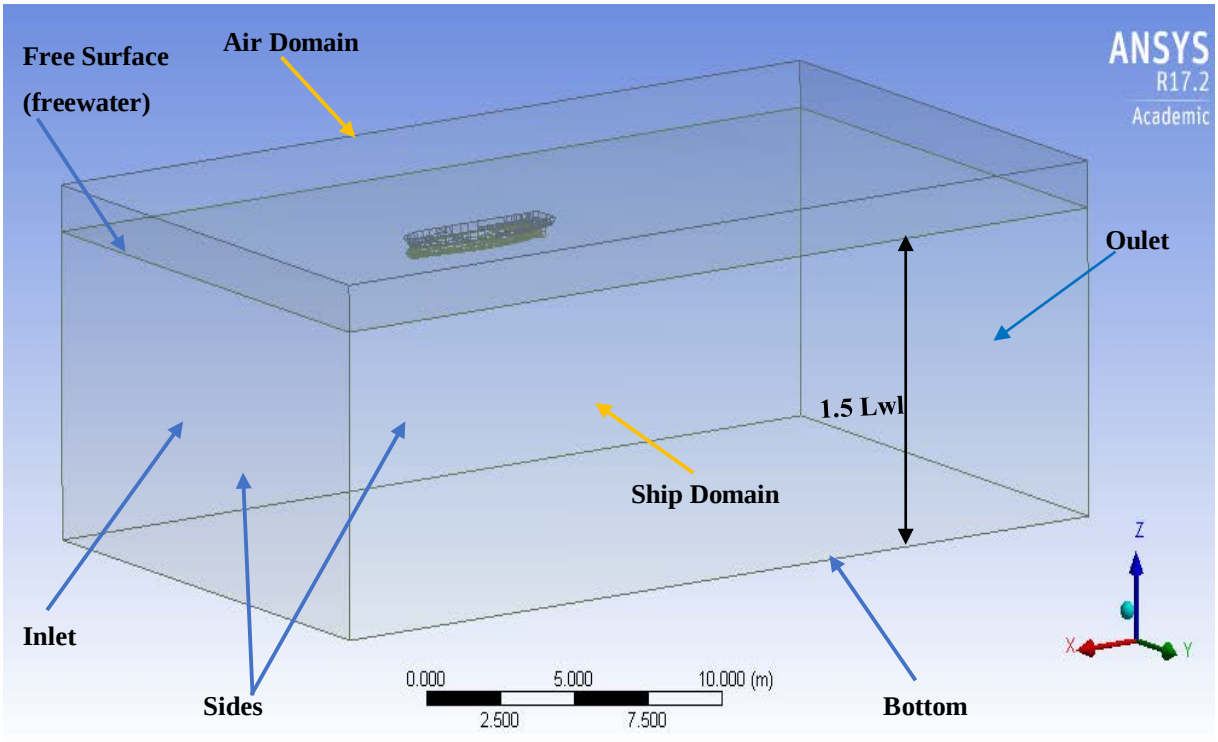

Figure 20 Computational Domain Size and Patch Descriptions of Ship Domain (Stationary Domain)

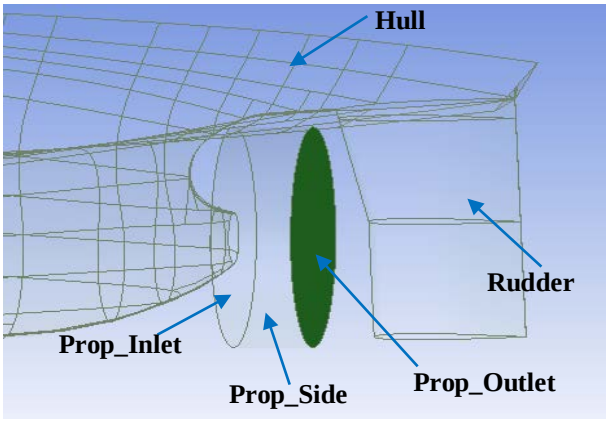

Figure 21 Computational Domain Size and Patch Descriptions in Stern View of Ship Hull in Ship Domain

In Figure 21, the cylindrical shaped container called propeller cylinder which is located at the propeller position behind hull in order to accommodate the rotating of Propeller Domain (Rotating Domain). The computational dimensions of this cylinder will be described details in the next *Sub-section 3.3.2.*

DesignModeler (DM) in ANSYS Workbench is used for the creation of this whole geometry since it provides a good connection. As shown in Figure 20, the fluid domain above the free surface is called air domain since the actual condition above the draft of ship is exposed to air. This air domain was not included in the numerical propulsion simulation in this thesis work.

The fluid domain below the free surface is called Ship Domain where the numerical viscous flow simulation took place.

3.3.2. Computational Propeller Domain Creation

The computational propeller domain includes the propeller blades, propeller hub and the propeller cylinder. For constructing the Propeller Domain, DesignModeler is also used in ANSYS Workbench. The non-dimensional domain dimensions of computational propeller domain are as described below

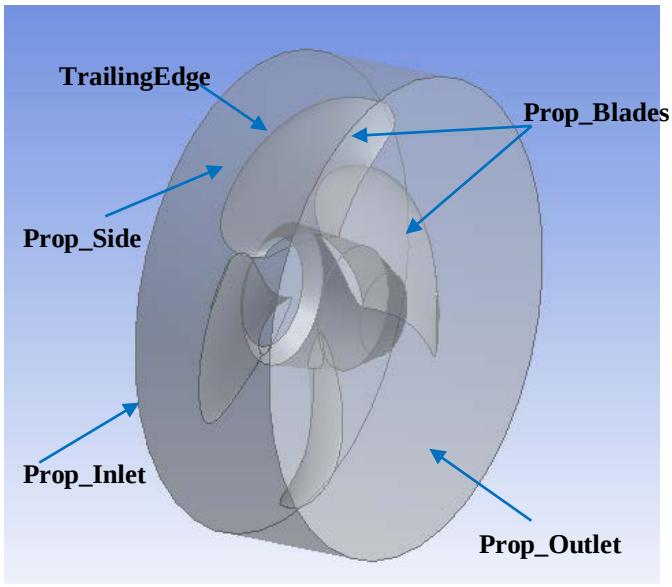

Figure 22 Computational Domain Size and Patch Descriptions in Propeller Domain [Perspective View (Left) & Side View (Right)]

Propeller Cylinder Dimensions: **Removed due to Non-disclosure Agreement**

3.4. Meshing Implementation of Computational Domains in ANSYS Workbench Meshing

Some of the theoretical point of meshing and mesh types are already mentioned in *Sub-section 2.1.2*. The overview of meshing controls set up and the implementation of mesh generation for the computational domains by using ANSYS Workbench Meshing are described in this section. Mesh generation is one of the most important steps to simulate numerical problems. Fundamentally, numerical CFD simulations are affected by the quality of the mesh. A high-quality mesh makes CFD simulations accurately and converges quickly whereas the poor

quality of the mesh can approach poor results. [28] The mesh of the fluid domain has to be of high quality to have faster convergence and to capture the flow characteristics. To resolve the boundary layer, the y^+ value has to be chosen with respect to the turbulence model. [38]

The meshing for numerical propulsion simulation is really complex and time-consuming task since the ship hull, rudder and propeller have to mesh together. However, the approach that we used to make numerical propulsion simulation simply this complexity task by dividing the rectangle and cylinder domains. The meshing for two domains can be done individually and then combined these meshing domains together for simulation set up.

The meshing generation for Ship Domain and Propeller Domain was implemented by using ANSYS Workbench Meshing. Meshing in ANSYS Workbench is to provide robust, easy to use meshing tools that will simplify the mesh generation process. These tools have the benefit of being highly automated along with having a moderate to high degree of user control.

In ANSYS Workbench, the geometries can be imported into the Meshing and then this Meshing can provide the meshing objects to perform the numerical simulations in CFX solver.

Since the numerical propulsion test is simulated by using RANS viscous solver, ANSYS CFX, the governing equations are discretized with Finite Volume Method. Therefore, the volume mesh elements has to be chosen for these computational domains. According to Table 1 and the standard set up of meshing in this thesis work, the simulations are carried out on the unstructured volume mesh of tetrahedrons.

ANSYS Workbench offers various strategies for CFD/Fluids meshing such as Assembly Level Meshing vs. Part/Body Level Meshing, Meshing by Algorithm, Meshing by Element Shape. For each strategy, certain defaults are in place to target the particular needs of an analysis. Among them, Meshing by Algorithm strategy is used for this study.

Tetra mesh method is a Delaunay tetra mesher with an advancing-front point insertion technique used for mesh refinement. The Patch Conforming Tetra mesh method provides support for 3D inflation and Built-in growth and smoothness control. The mesher will try to create a smooth size variation based on the specified growth factor. [45]

3.4.1. Mesh Generation of Ship Domain

Firstly, we imported the geometry of ship domain from DesignModeler into Meshing in ANSYS Workbench. The meshing of whole Ship Domain was executed with the default settings of tetrahedron elements by using Patch Conforming Tetra Mesh algorithm method. We used inflation for some area of interest for boundary layer resolution. Meshing generation of

Ship Domain is shown in Figure 23. The total 1.34 millions of tetrahedral elements were generated for Ship Domain (Stationary Domain).

Removed due to Non-disclosure Agreement

Figure 23 Tetrahedral Volume Mesh Implementation of Ship Domain (Stationary Domain)

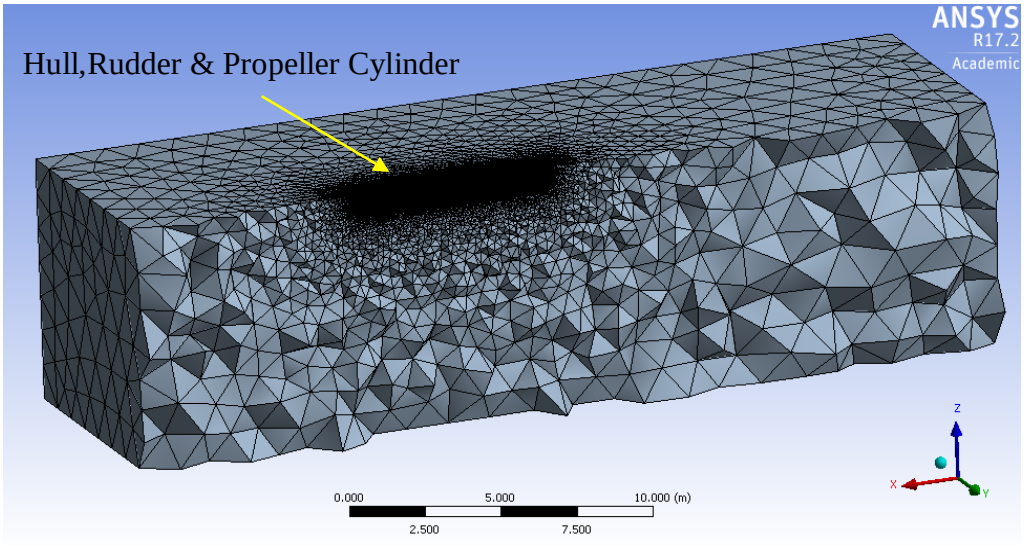

Figure 24 Tetrahedral Volume Mesh Implementation of Ship Domain (Stationary Domain) Half View

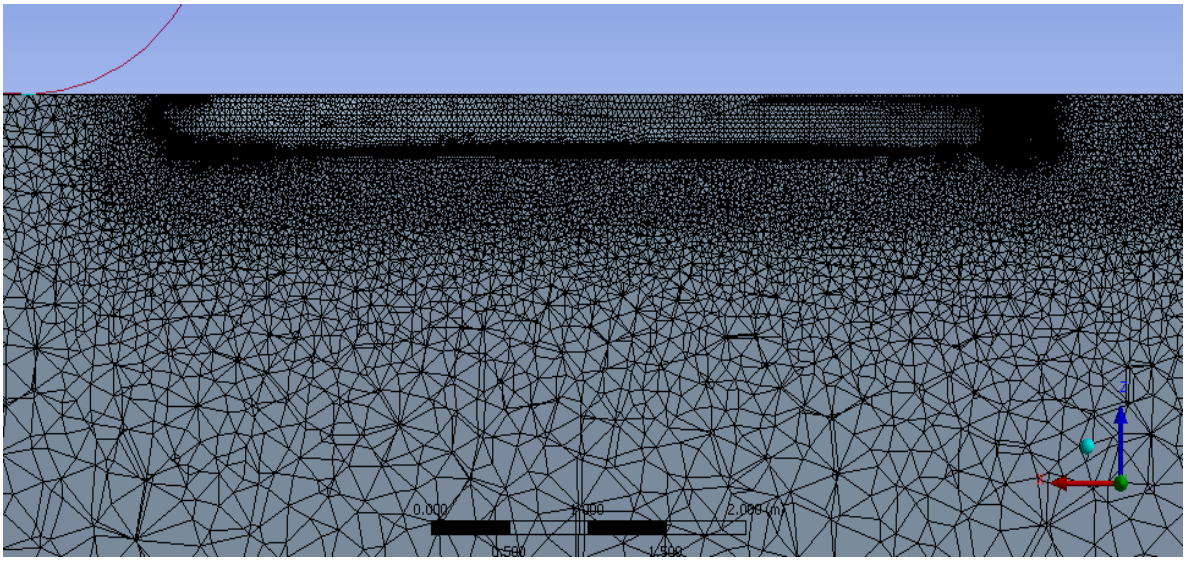

Figure 25 Mesh Generation of Ship Domain Near Hull

According to Figure 26, the mesh refinement around hull and rudder were applied. The inflation layers can be seen along the hull and rudder. Since these two parts (hull and rudder) will be defined as Wall in computational setup. The inflation layer provided reliable definition of boundary layer and the values of wall y+ near hull and rudder can be observed in Post-processing of simulation. The inflation layer is used to improve the accuracy of viscous flow solution.

Removed due to Non-disclosure Agreement

Figure 26 Refinement Meshing Implementation of Hull and Rudder in Ship Domain [Top (Stern View) & Bottom(Bow View)

The total number of unstructured tetrahedral elements generated was 1.34 millions. And the generated elements for each parts in Ship Domain is shown in Table 4.

Table 4 No. of Nodes and Elements Generated in Ship Domain

Removed due to Non-disclosure Agreement

3.4.2. Mesh Generation of Propeller Domain

For meshing implementation of Propeller Domain, the procedure was the same of Ship Domain's meshing generation. Meshing generation of Propeller Domain is shown in Figure 27. The total 0.9 millions of tetrahedral elements were generated for Propeller Domain (Rotating Domain).

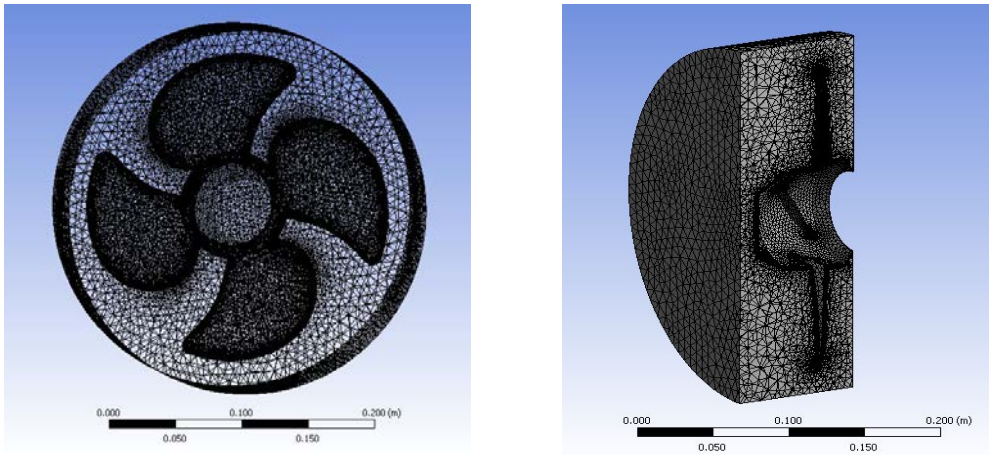

Figure 27 Tetrahedral Volume Mesh Implementation of Propeller Domain (Rotating Domain)

Different zones with refined meshes have been applied around the cross section of the blade at the hub intersection and near blade tip where high velocity gradients have been expected to enhance the accuracy of the solution. The propeller blades and propeller hub were refined with inflation layers as seen in Figure 28.

Removed due to Non-disclosure Agreement

Figure 28 Refinement Meshing Implementation around Hub and Blades of Propeller in Propeller Domain

The generated elements for each part in Propeller Domain is shown in Table 5.

Table 5 No. of Nodes and Elements Generated in Propeller Domain

Removed due to Non-disclosure Agreement

3.5. Numerical Propulsion Simulation Set Up

This section deals with the numerical simulation set up for propulsion test by using ANSYS CFX.

According to Table 2 & Table 3 of the test data description in *Section 3.2*, the self-propulsion test has been performed at vessel's service speed of 12 knots. Therefore, the numerical propulsion simulation has to be performed at model speed of Vs = 3.795 knots (1.95 m/s). By using British Method of Propulsion test, the self-propulsion point for propeller model was predicted. Therefore, the model propeller revolution was operated at 11.61rps and 11.81rps when the model vessel speed was Vs = 1.95 m/s.

As mentioned in *Section 3.1*, the propeller model has to be operated behind the model vessel's hull. In order to perform this simulation, the approach (which Propeller Domain including propeller model is combined with Ship Domain including hull, rudder and propeller cylinder) is adopted. Referring to this approach, the geometries and meshing of these two domains has been built independently in ANSYS Workbench workflow. The implemented meshing of these two domains were imported into ANSYS CFX workplace.

The ANSYS CFX can simulate the fluid behaviour in these computational domains. The self-propulsion numerical simulation is necessary to give rotation motion of propeller. For dynamic simulation, unsteady (transient type) model has to be used.

3.5.1. Simulation Setup Details in ANSYS CFX

In CFX case set up, the flow analysis type was chosen as "Transient" for this simulation. The maximum timesteps has been set as 1000 starting from initial time 0s.

For Ship Domain and Propeller Domain, the analysis of fluid domain is set as water with density of 998.5 kg/m^3. The viscosity and the model used for the working fluid are set as Continuous Fluid with kinematic viscosity of 1.06 x 10^{-6} m^2/s . The Propeller Domain was set as Rotating Motion with angular velocity of defined rps while the Ship Domain was set as Stationary.

For solving the Navier-Stokes equation, Unsteady RANS is used for transient simulation. In this propulsion simulation, the Shear Stress Transport SST k-ω model is used as the turbulence model because of the good behavior for adverse pressure gradient flows. The detailed governing equations and theoretical description are represented in *Chapter 2*.

For the treatment of viscous flow near wall which was applied the refinement meshing of inflation layers, the Automatic Wall Treatment option was chosen.

Boundary Conditions Setup

The consideration of the boundary is a critical part in computational fluid flow simulation which can affect the solution. The detailed boundary treatment is represented as shown in Figure 29 and described in Table 6 & Table 7.

The flow toward the vessel can then be defined by an inlet boundary condition, where the water velocity is specified, and an outlet boundary condition, where the average static pressure of the boundary surface is defined. The other bounding surfaces of the Ship Domain including freewater (freesurface) obtain a frictionless wall boundary condition as free slip condition. [46] The wall with no-slip boundary condition is applied on the surface of the hull, the propeller and the rudder, while around the propeller cylinder domain interface condition is applied. This no-slip boundary condition is by default, indicating that the fluid sticks to the wall and moves with the same velocity at the wall.

Table 6 Boundary Condition Assignment in Inlet and Outlet of Stationary Domain

Patch/Boundary Name (Domain)	Inlet (Ship Domain/Stationary)	Outlet (Ship Domain/Stationary)
Boundary Type	Inlet	Outlet
Velocity Components U,V,W [m/s]	V_x,0,0	-
Average Static Pressure[Pa]	-	P

Table 7 Boundary Condition Assignment in Stationary and Rotating Domains

Patch/Boundary Name (Domain)	**Boundary Type**
Hull (Ship Domain/Stationary)	No Slip Wall

Rudder (Ship Domain/Stationary)	No Slip Wall
Freewater/Freesurface, Sides, Bottom (Ship Domain/Stationary)	Free Slip Wall
Propeller Blades (Propeller Domain/Rotating)	No Slip Wall (with Rotating Frame Type)
Propeller Hub (Propeller Domain/Rotating)	No Slip Wall (with Rotating Frame Type)
Propeller Inlet, Propeller Outlet, Propeller Side (Both Domains)	Interface

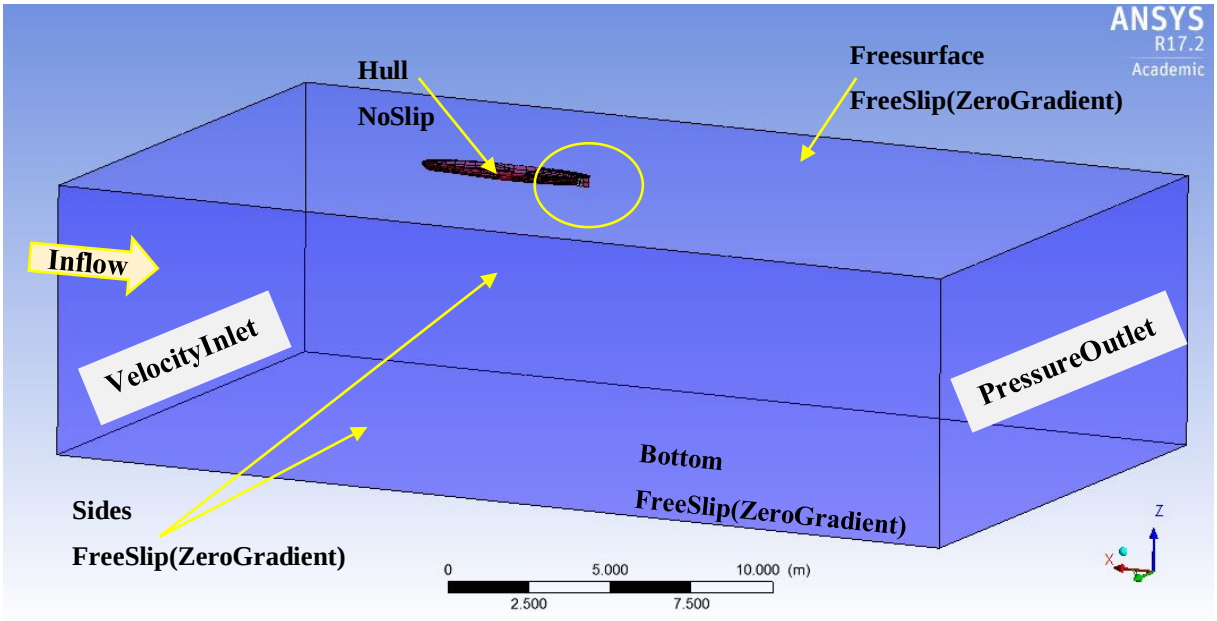

Figure 29 Boundary Assignment of Ship Domain

Transient Rotor Stator Mixing Model of Domain Interface

The sliding mesh approach was used in order to simulate the rotating propeller. This means that the whole propeller domain rotates with a speed equivalent to the defined propeller's speed of rotation. The transient rotor stator is chosen as Mixing model.

A control surface approach is used to perform the connection across a GGI attachment or periodic condition. If transient rotor-stator is set up, then the current relative position of each

side of a sliding interface is first computed at the start of each timestep. Each frame change model then proceeds by discretizing the surface fluxes along each side of the interface in terms of nodal dependent variables, and in terms of control surface equations and control surface variables. Each interface surface flow is discretized using the standard flux discretization approach, but employs both the nodal dependent variables on the local side of the interface and control surface variables in the interface region. [32]

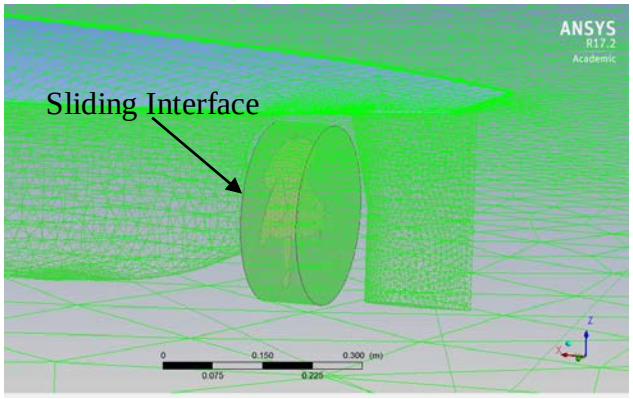

Figure 30 Meshing in Propeller Cylinder as Sliding Interface

3.6. Solving Simulation in ANSYS CFX

The simulation was solved using ANSYS CFX (17.2). The commercial CFD code ANSYS CFX was used to the RANS equations with Finite Volume discretization scheme using two equations SST k-ω turbulence modeling. A criterion is implemented in such a way that the variation in a chosen calculated value (residuals or force monitors) is evaluated for each time step and when the criterion meets the assigned residual tolerance for 1000 iterations, the solution is evaluated as converged. In this propulsion simulation, there are two indications for converged results. If all the residuals, which show the difference of the value (pressure, velocity, etc.) between the current iteration and the previous one, go down with every iteration or the overall trend for the residuals are going down, that means a good convergence is achieved. Another indication of a good convergence is the behavior of one of the key parameters (output controls) such as forces at X direction exerted on hull, propeller hub and propeller blades and torque at propeller blades. These parameters should be constant at every iteration step when convergence is achieved. The convergence can be monitored by checking residuals. The maximum number of iterations was 1000 in order to have an acceptable level of solution convergence. The convergence criteria for residual is at $1x10^{-6}$ for momentum equations.

3.7. Test Case Definition

This section describes the cases definitions for numerical propulsion simulation. The main objective of this study is to investigate the numerical results of propulsion simulation mainly on the propeller efficiency when the operated propeller position was changing behind hull. In this thesis, the numerical propulsion simulations were performed with four different cases that mean four different propeller allocation. The propeller blade is defined about a line normal to the shaft axis called either the 'propeller reference line' or the 'directrix'/'genetrix'. In the case of the controllable pitch propeller the term 'spindle axis' is frequently synonymous with the reference line or directrix/genetrix. The terms spindle axis, directrix and reference line relate to the same line, as can be seen in Figure 31. [47]

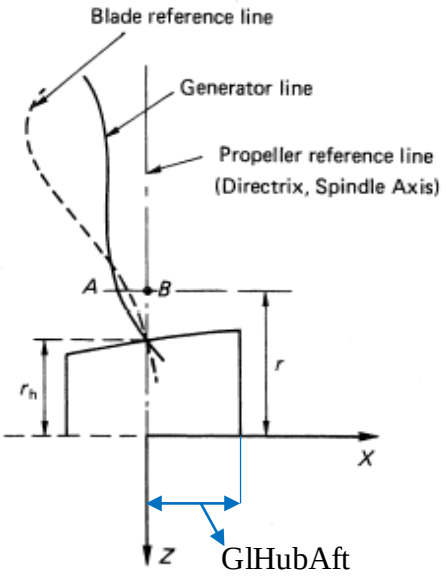

Figure 31 Blade Reference Line [47]

One propeller blade is developed into full propeller geometry on the hub. These propeller blades were developed with the regular interval angle based on the propeller reference line called genetrix. In order to perform four different locations of propeller positions behind hull, the development of propeller blades were accomplished with the different locations of genetrix.

According to Figure 31, the distance between the aft end of the propeller hub and the directrix/genetrix line is called GlHubAft. By changing the values of GlHubAft, the propeller blades were generated with different propeller genetrix position. Therefore, four different propeller positions were set behind hull according to the different values of GlHubAft. The four cases of propeller blades positions can be seen in Figure 32 and the values of GlHubAft for each case is described as follow;

- For Case 1, GlHubAft = 0.28 m
- For Case 2, GlHubAft = 0.234 m
- For Case 3, GlHubAft = 0.13m
- For Case Orig, GlHubAft = 0.2655m

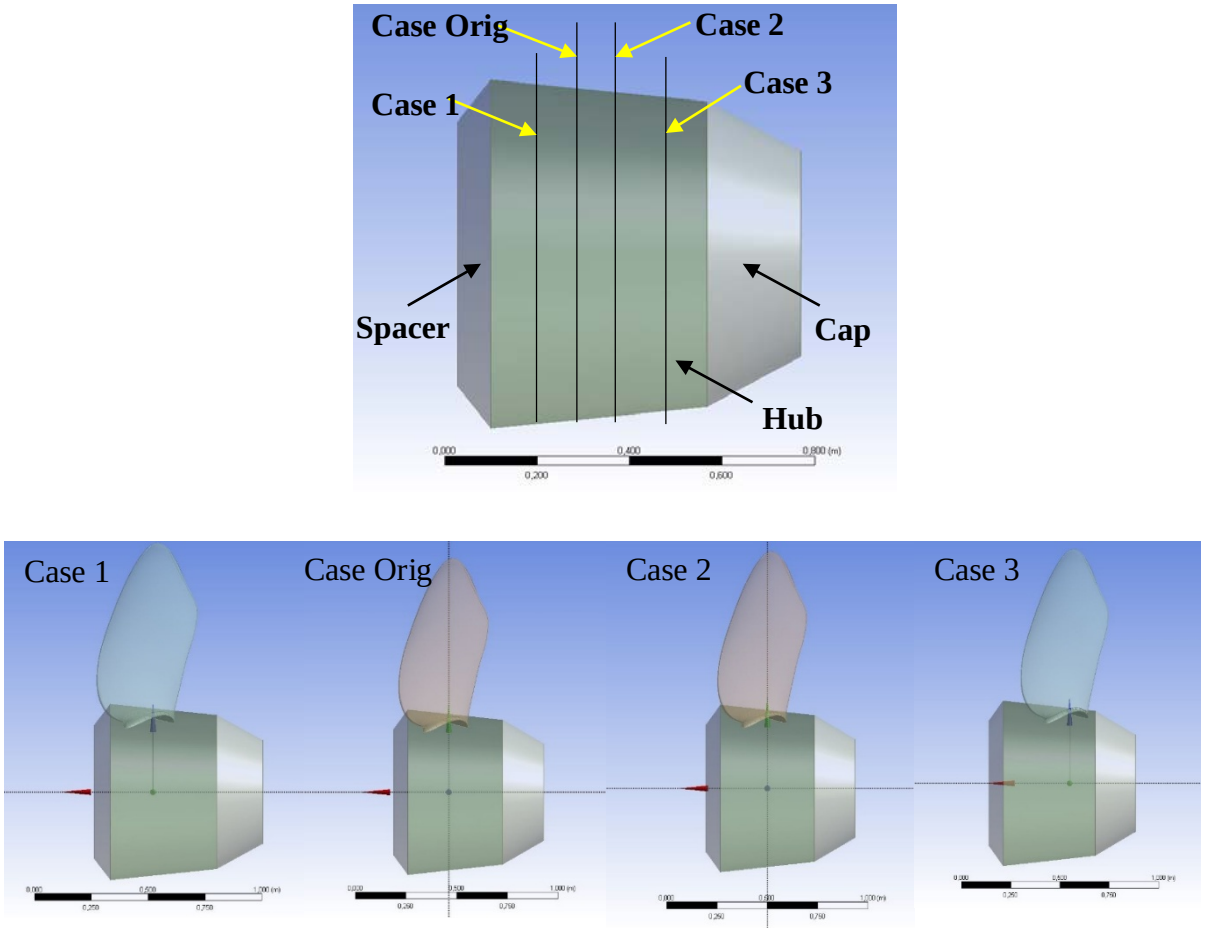

Figure 32 Propeller Blades Position for Four Cases along The Hub

The CaseOrig is taken as the reference position of the propeller and the other propeller positions are relocated referring to this CaseOrig. Therefore, the numerical propulsion simulations was performed in order to evaluate the results for four cases; Case1, Case2, Case3, CaseOrig. There were two simulation running conditions for each case that can be represented in Table 8.

Table 8 Numerical Propulsion Simulation Running Conditions for Each of Four Cases

	V_S [knots] (Full Scale Vessel Speed)	n_M [rps] (Model Propeller Revolution)
Simulation Run 1	12	11.61
Simulation Run 2	12	11.81

When we got the results of these two simulations with different propeller model revolution at constant vessel's speed for each case, we evaluated the self-propulsion point for each case. After evaluating the self-propulsion point for each case, we performed the numerical simulation with self-propulsion point of model propeller revolution at constant vessel's speed for each of four cases in order to compare the post-processing results. Firstly, these propulsion simulations were performed with the hull, propeller rudder together that will be used as the term "Simulations with Rudder Condition". Afterward, the numerical propulsion simulations in condition of hull, propeller together (without rudder) for all cases were carried at the model propeller revolution of 11.71 rps. These simulations were referred as the term "Simulations without Rudder Condition". Therefore, there were two self-propulsion simulations that have to be computed in this thesis work i.e. self-propulsion simulations with rudder condition and without rudder condition. These simulation results are purposed to observe the rudder influence in the propulsion simulations and the fluid flow form of rotating propeller behind hull.

4. NUMERICAL REVERSE OPEN WATER SIMULATION OF PROPELLER IN MODEL SCALE

This Chapter deals with the numerical simulation for reverse open water test of propeller. In order to evaluate the self-propulsion point of the propeller, non-dimensional open water chart of propeller is used. Therefore, the full-scale and model scale open water chart data is required for extrapolating the parameters for full scale conditions of propulsion characteristics in this thesis.

When the numerical simulation for propeller performance in open water condition, there are two ways to make simulation .i.e. Open Water Simulation and Reverse Open Water Simulation according to the literature and research papers. The experimental set up of open water test of propeller is mentioned details in *Section 2.2*. In this thesis, Reverse open water numerical simulation of propeller model (which will be referred from now on as "ROW") was performed. The test case propeller data for reverse open water simulation has been described in Table 3, and the model propeller with scale ratio λ=10 was used to perform numerical ROW simulation. When propeller is working in the open water condition, the propeller is in the uniform inflow field. Therefore, the numerical ROW simulation was performed in steady state mode. The rotation of the propeller is accounted by using Moving Reference Frame (MRF) approach. The RANS solver, ANSYS CFX was also used for numerical ROW simulation. An unstructured tetrahedral grid with approximately 1.46 million elements is used.

4.1. Geometry Creation Of Computational Domains In DesignModeler

Removed due to Non-disclosure Agreement

Figure 33 Computational Domain Size and Patch Descriptions of OWT Domain (Stationary Domain)

Removed due to Non-disclosure Agreement

Figure 34 Computational Domain Size and Patch Descriptions of Propeller Domain (Rotating Domain)

4.2. Meshing Implementation of Computational Domains in ANSYS Workbench Meshing

Removed due to Non-disclosure Agreement

Figure 35 Tetrahedral Volume Mesh Implementation of OWT Domain (Stationary Domain)

Removed due to Non-disclosure Agreement

Figure 36 Refinement Meshing Implementation of Propeller Shaft in OWT Domain

Removed due to Non-disclosure Agreement

Figure 37 Tetrahedral Volume Mesh Implementation of Propeller Domain (Rotating Domain)

Removed due to Non-disclosure Agreement

Figure 38 Refinement Meshing Implementation around Hub and Blades of Propeller in Propeller Domain

4.3. Numerical Reverse Open Water Simulation Set Up

Removed due to Non-disclosure Agreement

Figure 39 Boundary Assignment of OWT Domain and Propeller Domain

Table 9 Boundary Condition Assignment in Inlet and Outlet of Stationary Domain

Removed due to Non-disclosure Agreement

Table 10 Boundary Condition Assignment in Stationary and Rotating Domains

Removed due to Non-disclosure Agreement

4.4. Solving and Post-Processing Of ROW Simulation Results

When the simulation was finished, the thrust and torque around the propeller blades have been executed from the results.

Like the experiment model test, the computed thrust and torque on the propeller are converted into the dimensionless thrust coefficient K_T, torque coefficient K_Q and the open water coefficient η_o is calculated. The advance ratio J and the three coefficients can be evaluated by using the Equation (8), (9) & (10) that has been mentioned in *Sub-section 2.2.1*. The model open water chart can be represented as shown in Figure 40.

According to the ITTC 2014 Procedure, the scale effect corrections for propeller performance must be done in order to extrapolate the full-scale open water parameters from the model scale. The steps and equations has been described in *Sub-section 2.4.3*. The full scale open water chart can be illustrated as Figure 41.

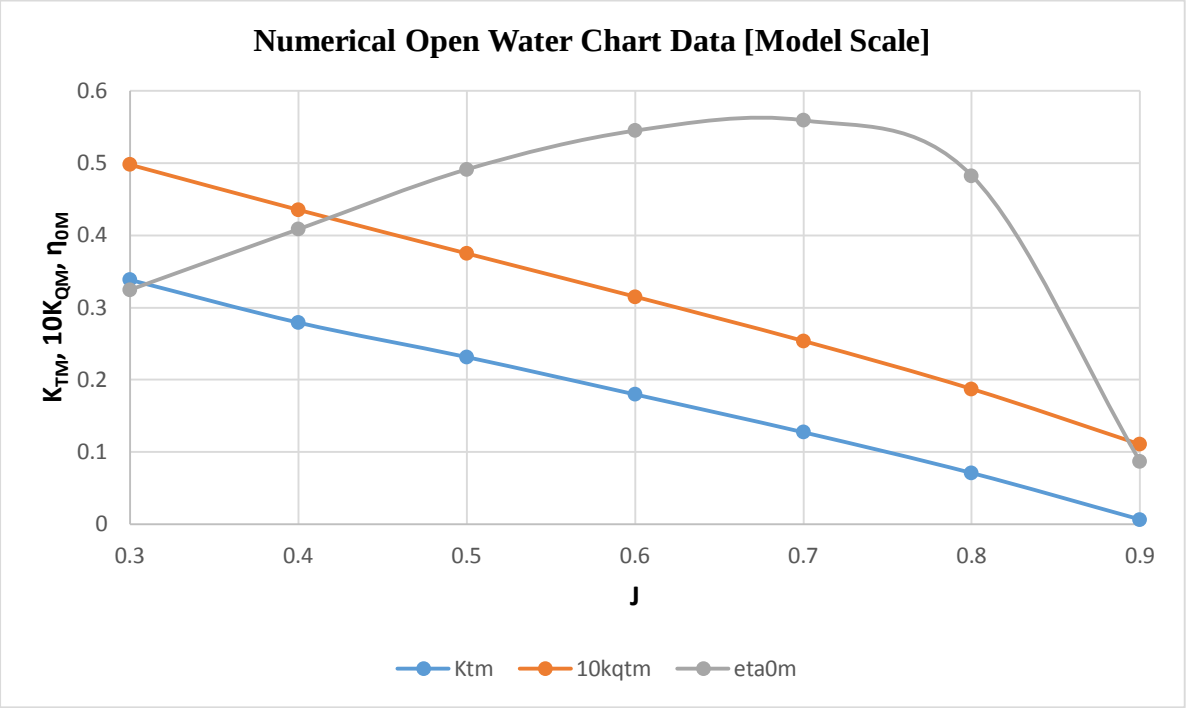

Figure 40 Numerical Open Water Chart Data in Model Scale

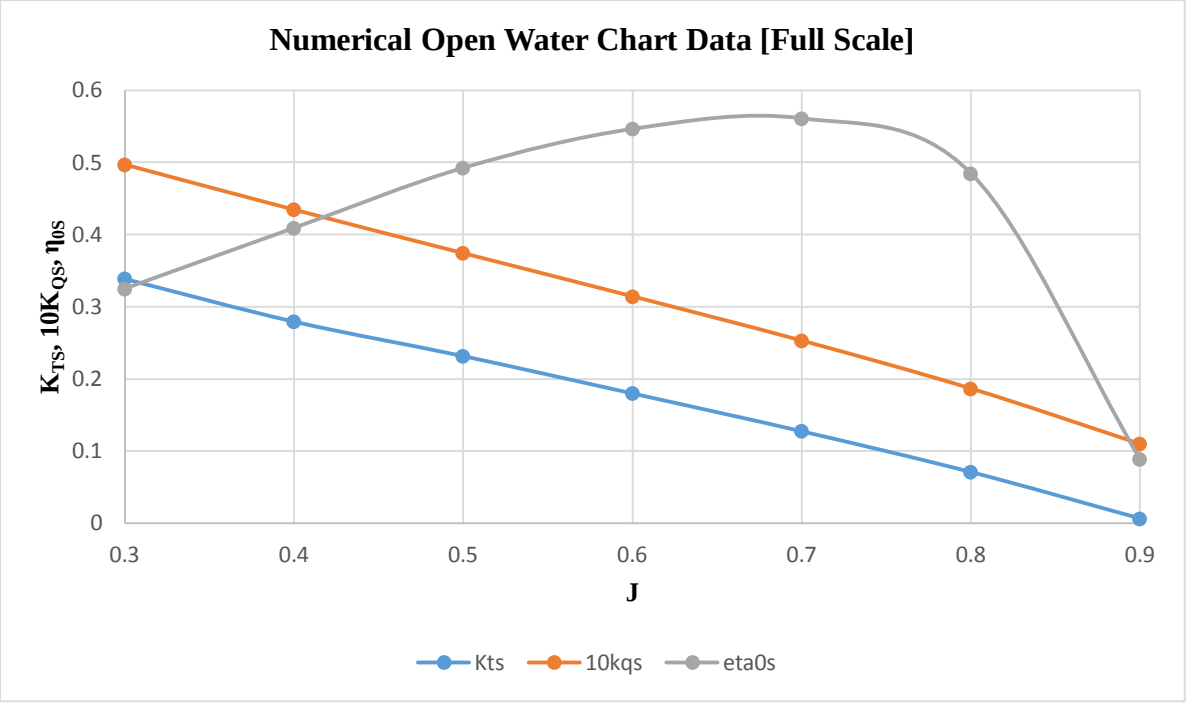

Figure 41 Numerical Open Water Chart Data in Full Scale

5. NUMERICAL INVESTIGATION ON RESULTS OF PROPULSION SIMULATIONS

This chapter deals with the numerical investigation on the results of propulsion simulations. After running the propulsion simulations for different four cases as described in *Chapter 3*, the results from the model propulsion simulations were extrapolated to the full scale propeller operated conditions behind hull by determining the parameters such as thrust deduction fraction, wake fraction, relative rotative efficiency, thrust, torque, delivered power, hull efficiency and propulsion efficiency. The comparison of these parameters has to be done between Case1, Case2, Case3 and Case Orig. The pressure exerted on the hull at certain points were shown and compare for different cases. Afterward, flow field of different position was described and compared for all cases.

5.1. Determination of Full-Scale Propulsion Results By Using ITTC 1978 Service Performance Prediction Method

This section describes the evaluation of full-scale propulsion conditions from the numerical model propulsion simulations for four cases. In order to achieve the results for full scale propulsion condition, we applied the ITTC 1978 service performance prediction method that has been mentioned in *Section 2.4*.

5.1.1. Computed Results from Numerical Propulsion Simulations for Four Cases

As we mentioned in *Section 3.1*, we used the load varying self-propulsion test or British method for numerical propulsion simulations for four cases. Using the British method involved interpolating the self-propulsion point by towing at forces around that of the expected self-propulsion point and interpolating to find the actual self-propulsion point. This is effectively achieved by varying the propeller revolutions. [17]

For each case of four cases, we decided to choose fixed ship model speed with two appropriate propeller revolutions. These two values are important to be selected to cover the area around the estimated self-propulsion point since the results of experimental propulsion tests are already known and the self-propulsion point is already predicted from that experimental results. Therefore, we run the numerical propulsion simulations for four cases at constant vessel's speed V_s = 12knots with two propeller revolutions n_M = 11.61rps and n_M = 11.81rps. For each

simulation run, the thrust (T_M) and torque (Q_M) on the propeller blades and the force exerted on the model hull (F_{XHull}) are measured during the simulation.

Since the free surface was omitted in the numerical propulsion simulations that means the under-water part of the hull was only considered and the free surface condition is assumed as the still water boundary condition. Therefore, the measured F_{XHull} cannot be regarded as resistance (R_T) of the hull. In real propulsion simulation, the free surface elevation (wave) will occur along the ship hull. Hence, the F_{XHull} measured from the numerical propulsion simulations was necessary to be corrected for added resistance of wave on hull. The correction value of Δwave (in N) was added to the F_{XHull} by adjusting the self-propulsion point.

Table 11 Computed Results For Model Scale of Numerical Propulsion Simulations for Four Cases

Removed due to Non-disclosure Agreement

5.1.2. Performance Prediction Method

The details of ITTC 1978 performance prediction method (IPPM78) described in *Section 2.4*. The results of the analysis from resistance test, open water test and propulsion tests are inputs to the performance prediction analysis. The thrust identity approach was adopted for IPPM78 calculation.

In this thesis, the numerical resistance test did not performed. Therefore, the required resistance test data was used from the experimental resistant towing tank test results. For open water test data, we used both of the experimental open water chart and the numerical open water chart. The required propulsion data took from the numerical propulsion simulations.

By using the data results from the two simulation runs, towing force ($F_{carriage}$) curve against the thrust measured(T_M) is plotted for vessel's speed of 12 knots. According to Holtrop (2001) the towing force against thrust curve should follow a linear trend regression, hence a linear trendline should be a good representation of the mean value of the data.

If the model propeller balances the model resistance and fully self-propels the model then it will be working at a higher thrust loading than the full scale. This is due to the difference in frictional coefficients between the model and full-scale and the allowance at the full scale for roughness and still-air through the correlation allowance. In order to compensate for this difference the model is pulled with a force ($F_{carriage}$) that is equa1 in magnitude to F_D that is said to be at the ship self-propulsion point. 'Friction deduction force, F_D was calculated already with the data from resistance test using the following equation [17];

$$F_D = \frac{1}{2}\rho_M V_M^2 S_M [C_{FM} - C_{FS} - C_A] = 2.98\ N \qquad (68)$$

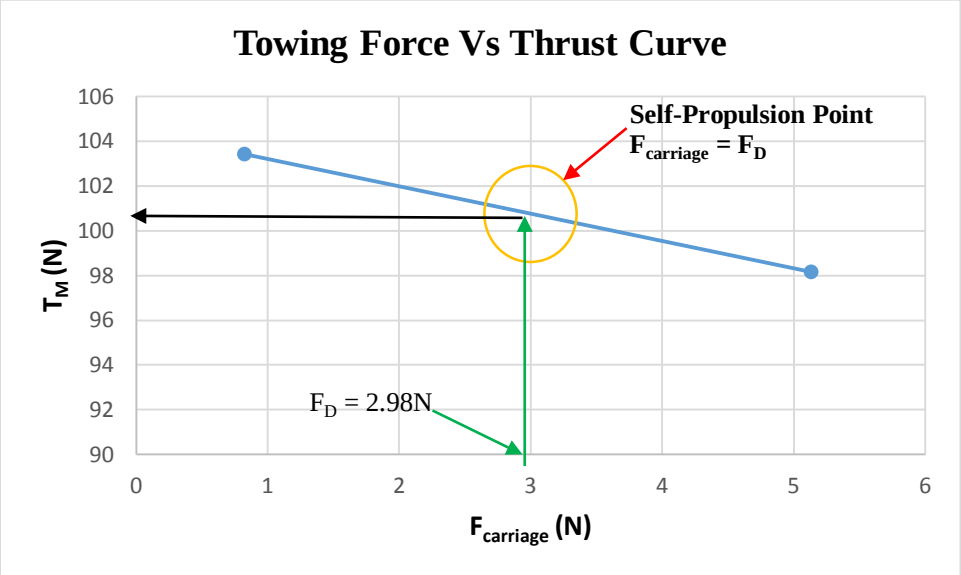

Figure 42 Towing Force Vs Thrust Curve for Model Self-propulsion Results

The self-propulsion point is defined as the point where the applied towing force is equal to the increased frictional resistance experienced by the model hull, due to the wrongly scaled viscous effects in model scale. It is important to get a good estimation of this point, as it is the main basis for the following extrapolation procedure. In this procedure the thrust identity approach is used to determine this point. [15]

From Figure 42, the self-propulsion point found at the point where $F_{carriage}$ (calculated from Table 11) is equal to F_D = 2.98 N. At the point, the corresponding values of model thrust (T_M) (can be read from the Figure 42), torque (Q_M) and propeller revolution (n_M) was calculated from the results of model self-propulsion simulations. With this read data, the non-dimensional propeller characteristics for thrust coefficient (K_{TM}) and torque coefficient (K_{QM}) was evaluated at the self-propulsion point.

Thrust identity is assumed, i.e. K_{TM} (Self-Propulsion Test) = K_{TM} (Open Water Test). Using thrust identity with K_{TM} as input data, J_{TM} and K_{QTM} are read off from the model propeller open water diagram as shown in Figure 43, and the corresponding model wake fraction (w_{TM}) and the relative rotative efficiency (η_R) can be calculated by following Equations (12) and (13) (that has been described in *Sub-section 2.4.1*).

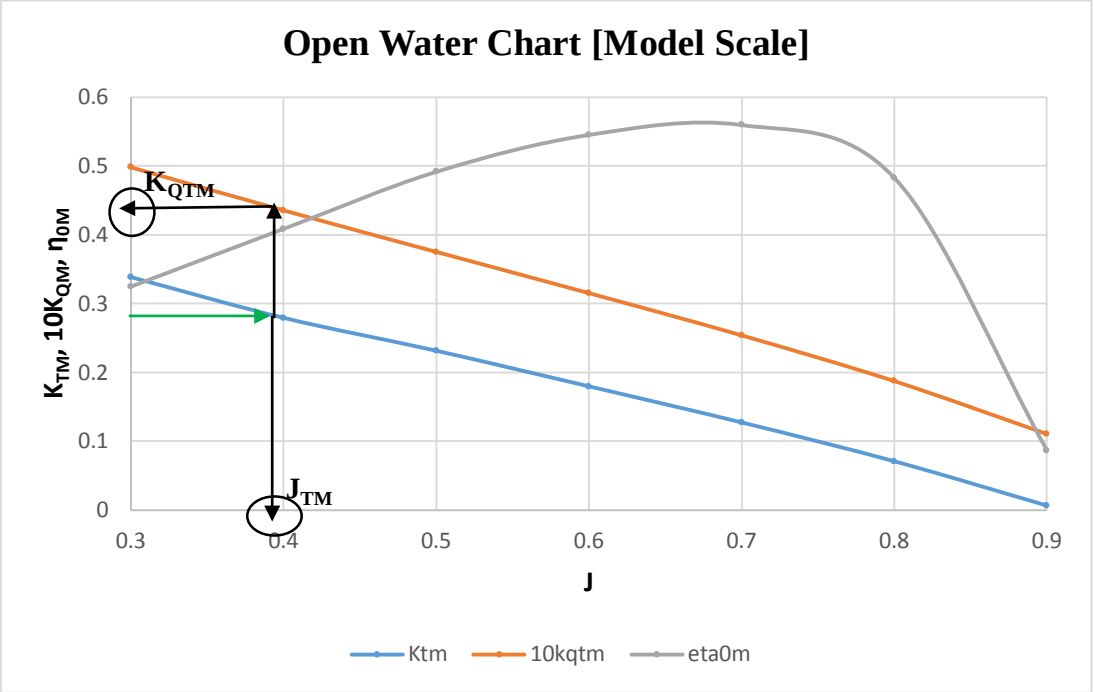

Figure 43 Example of Open Water Chart in Model Scale

The thrust deduction (t) was calculated by using the values of model thurst (T_M) and towing force or friction deduction force (F_D) (that was read at self-propulsion point) and the model vessel resistance R_{TM} and R_C (was taken from experimental resistance test results) according to Equation (14).

As mentioned in *Sub-section 2.4.2*, the full scale correction for total resistance coefficients of ship was evaluated by using the data from the experimental resistance model test results. And then, the scale effect correction for propeller characteristics were calculated by using model open water results from both numerical simulation that was performed in Chapter 4. The steps for correction of scale effect of propeller was followed according to *Sub-section 2.4.3*. The characteristics of the full-scale propeller K_{TS} and K_{QS} with respect to corresponding J values were obtained from the model characteristics. The full-scale open water chart can be seen in Figure 44.

The full-scale wake fraction (w_{TS})was evaluated by the following formula using the model wake fraction (w_{TM}), and the thrust deduction fraction (t) obtained as the analyzed results of self-propulsion test by using Equation (29).

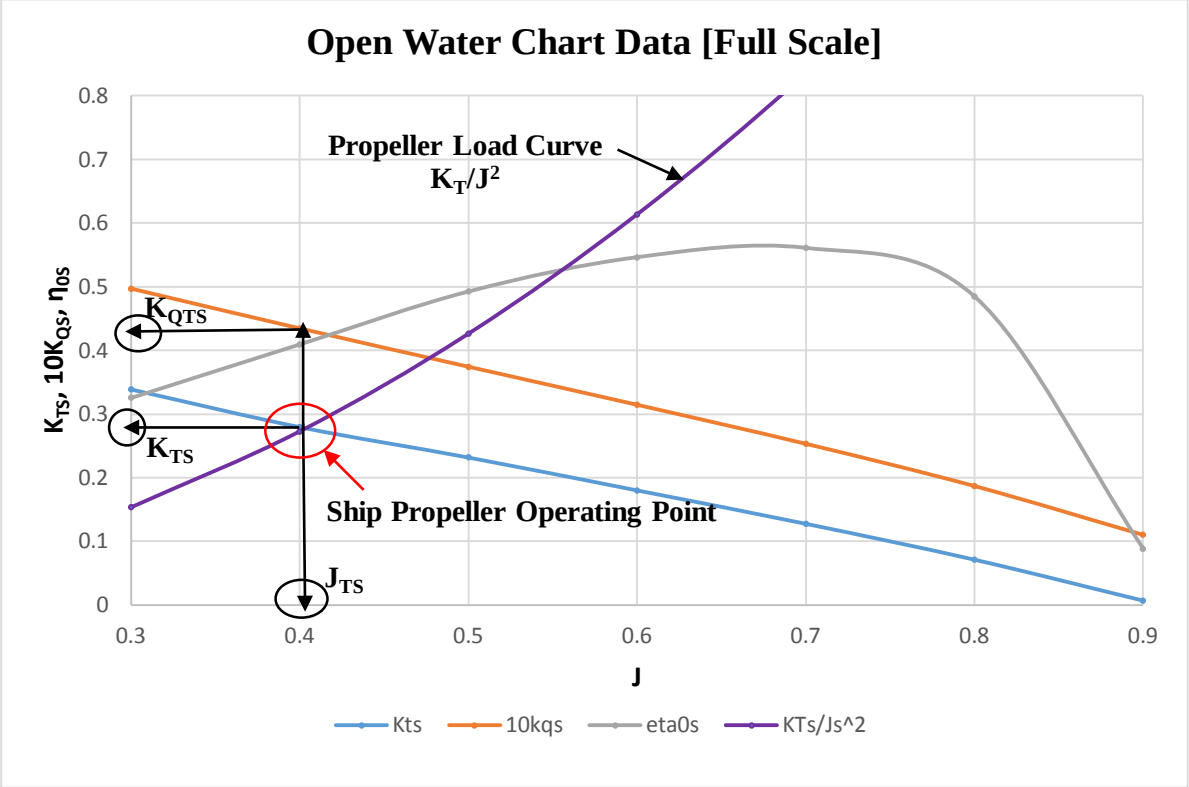

Figure 44 Example of Open Water Chart Data (Full Scale) with Propeller Load Curve

The propeller load curve K_T/J^2 (K_T as function of J) was plotted in the full scale open water chart that is represented in Figure 44. The load of the full-scale propeller was evaluated from Equation (30). The ship propeller operating point was interpolated using the intersection of the K_{TS} curve and the propeller load curve K_T/J^2 that was shown in Figure 44. The K_{TS} and K_{QS} curves are the open water propeller data corrected for full-scale Reynolds number. From this intersection point, we read the values of J_{TS}, K_{QTS} and K_{TS} for the full scale ship operating condition.

Based on the full scale propulsion point, the full scale propeller revolutions (n_s) was obtained from the advance coefficient formula according to Equation (31). The full scale torque (T_S) and thrust (Q_S) values were evaluated according to the Equations (33) & (34) by using the values of K_{TS} and K_{QTS} at self-propulsion point. At that point, the estimated delivered power (P_{DS}), propulsive efficiency (η_D) , hull efficiency (η_H) and effective power (P_E) were determined by using the Equations (32), (36), (37) and (35) that was mention in *Sub-section 2.4.4*.

For four cases: Case1, Case2, Case3 and CaseOrig with different propeller positions behind hull, the service performance prediction tasks mentioned above have to be done for each case with corresponding results. Therefore, the Excel Sheet was prepared for evaluating and performing these steps. The numerical propulsion simulation results (thrust(T_M), torque (Q_M) and force exerted on model hull (F_{XHull})) at vessel's speed (Vs) for two model propeller

revolutions (n_M), were given as input to that Excel Sheet and the following values were evaluated;

- n_M, revolutions of model propeller running at self-propulsion point
- T_M , thrust of model propeller running at self-propulsion point
- K_{TM}, thrust coefficient of model propeller at self-propulsion point (Thrust Identity)
- Q_M , thrust of model propeller running at self-propulsion point
- $K_{QM,}$ torque coefficient of model propeller at self-propulsion point (from Self-propulsion test results)
- $J_{TM,}$ advance coefficient of model propeller at self-propulsion point (Thrust Identity)
- $K_{QTM,}$ torque coefficient of model propeller at self-propulsion point (from open water chart data in model scale)
- η_R , relative Rotative Efficiency
- w_{TM} , model wake fraction
- t, thrust deduction fraction
- w_{TS} , full scale wake fraction
- K_{TS}, thrust coefficient of full scale propeller at self-propulsion point (from open water chart data in full scale)
- T_S , thrust in full scale propeller operating condition at self-propulsion point
- $J_{TS,}$ advance coefficient in full scale propeller operating condition at self-propulsion point
- $K_{QTS,}$ torque coefficient of full scale propeller at self-propulsion point
- Q_S , torque in full scale propeller operating condition at self-propulsion point
- n_S, revolutions of full scale propeller operating condition at self-propulsion point
- η_o , open water efficiency for model scale and full scale condition
- P_{DS} , deliver power in full scale operating condition
- P_E , effective power
- η_H , hull efficiency for model scale and full scale conditions
- η_D, propulsive efficiency

When performing the calculation steps, the determination of model thrust values at self-propulsion point (as shown in Figure 46) was done by using linear interpolation of the line regression. The determination of intersection values (from Figure 47 & Figure 44) was obtained by finding the intersection values of polynomial curves fitted in Excel.

5.2. Investigation on Results of Propulsion Simulations

This section shows the computed results of propulsion simulations, comparison between four cases for propulsion parameters of ship, the investigation on the propulsion efficiency by influence of propeller positions behind hull with and without rudder conditions.

When we performed the evaluating of the propulsion parameters of ship in the full scale operating conditions by the procedures of ITTC'78 performance prediction method, the propulsion results were evaluated from the numerical propulsion simulation results by using the open water chart data results from numerical reverse open water simulation that has been performed in Chapter 4.

In this thesis, the comparisons are not concerning on the experimental results and cannot be done since the propeller position is changed for four cases. The main objective is to study and compare the results of Case1, 2 and 3 with the results of CaseOrig as the CaseOrig is the original propeller position behind the ship hull. Therefore, we interested to investigate what parameters of propulsion results and fluid flow characteristics will change from that of the CaseOrig when the propeller position was changed behind ship hull. The influence of rudder existence on hull and propeller is also investigated with respect to changing of propeller positions. Table 12 shows the calculated propulsion results of full scale extrapolation at self-propulsion point from model scale by using numerical propulsion simulation results with/without rudder conditions and numerical open water simulation chart data. The self-propulsion point for numerical propulsion simulation with rudder condition was predicted approximately at n_M = 11.71 rps (model propeller revolution) for all cases with the vessel's speed of 12 knots. Due to insufficient time, the numerical propulsion simulation without rudder condition was performed at n_M = 11.71 rps for all cases with the vessel's speed of 12 knots and the results were evaluated to compared to the simulation with rudder condition.

Table 12 Propulsion Results of Full Scale Prediction from Model Scale by using Numerical Propulsion Simulation Results with/without Rudder and Numerical Open Water Simulation Results

Removed due to Non-disclosure Agreement

5.2.1. Importance of Propulsive Coefficient Prediction for Powering and Propulsion of Ship

The power estimate for propulsion unit is obtained by comparison with an existing similar vessel or from model tests. In either case it is necessary to derive a power estimate for one size of craft from the power requirement of a different size of craft. That is, there is a need to be able to scale powering estimates. The different components of the powering problem scale in various ways and it is therefore necessary to estimate each component separately and apply the correct scaling laws to each.

One fundamental division in conventional powering methods is to distinguish between the effective power (P_E) required to drive the ship and the power delivered (P_D) to the propulsion unit(s). The power delivered to the propulsion unit exceeds the effective power by virtue of the efficiency of the propulsion unit being less than 100%. The main components considered when establishing the ship power comprise the ship resistance to motion, the propeller open water efficiency and the hull– propeller interaction efficiency as shown in Figure 45.

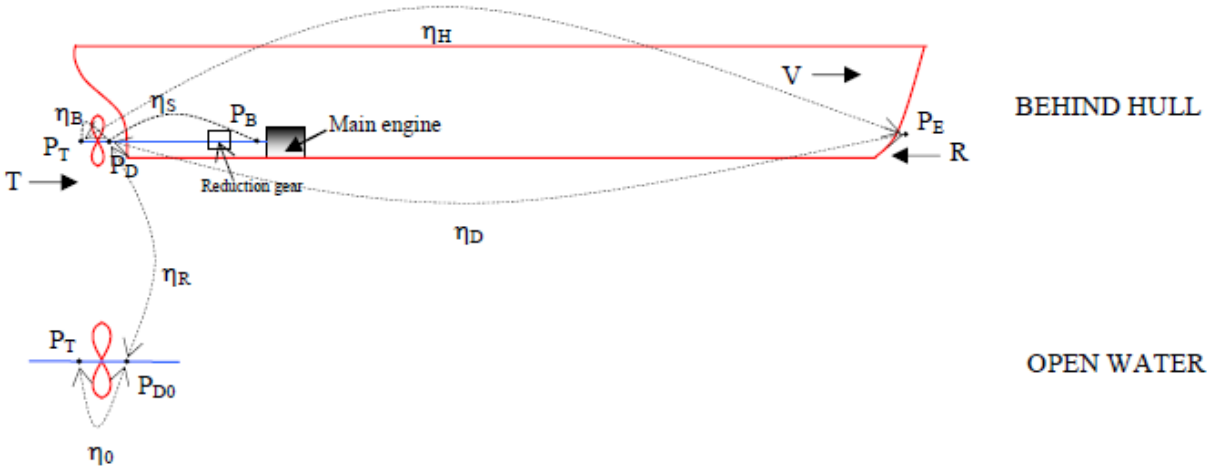

Figure 45 Components of Ship Powering and Efficiencies – Main Consideration [50]

A fundamental requirement of any ship propulsion system is the efficient conversion of the power (P) available from the main propulsion engine(s) [prime mover] into useful thrust (T) to propel the ship at the required speed (V_s). [25]

The general definition ‘power = force x speed’ yields the effective power

$$P_E = R_T \,.V_S \tag{69}$$

R_T is the total calm-water resistance of the ship excluding resistance of appendages related to the propulsive organs. Sometimes the rudder is also excluded and treated as part of the propulsion system. (This gives a glimpse of the conceptual confusion likely to follow from different conventions concerning the decomposition. Remember that in the end the installed power is to be minimized. Then ‘accounting’ conventions for individual factors do not matter.

What is lost in one factor will be gained in another.) V_s is the ship speed. P_E is the power we would have to use to tow the ship without propulsive system. We can also define a power formed by the propeller thrust and the speed of advance of the propeller, the so-called thrust power:

$$P_T = T \,.\, V_A \tag{70}$$

The thrust T measured in a propulsion test is higher than the resistance R_T measured in a resistance test (without propeller). V_A is the speed of advance of propeller i.e. the propeller inflow. [18]

From a propulsion point of view, the performance of a ship and propulsion system can be analyzed by means of propulsion efficiency (η_D) or Quasi-propulsive coefficient (QPC) and its components. The propulsion efficiency (η_D) can be established as

$$\eta_D = \frac{Effective\ Power}{Delivered\ Power} = \frac{P_E}{P_D} = \frac{R_T . V_S}{2\pi n Q_S} \tag{71}$$

It can be also expressed as

$$\eta_D = \eta_H \,.\, \eta_0 . \eta_R = \frac{1-t}{1-w} \,.\, \eta_0 . \eta_R \tag{72}$$

where P_E = Effective Power

P_D = Power Delivered to Propeller

R_T = Total Resistance of Hull without Propeller

V_S = Speed of Vessel

n = Propeller Rate of Revolution

Q_S = Propeller Torque

η_H = Hull Efficiency

η_0 = Propeller Open water Efficiency

η_R = Propeller Relative Rotative Efficiency

t = Thrust Deduction Factor

w = Wake Fraction

As we can see in above two equations, the propulsion efficiency is the ratio between effective power, P_E and the necessary power delivered to the propeller, P_D. Moreover, it can also expanded as the product of the hull efficiency, η_H, the open water propeller efficiency, η_0 and the relative rotative efficiency, η_R. Therefore, the propulsive efficiency is dependent on these components, and these components are in turn depending on the other factors of ship hull and propulsion system. The variation in those factors can lead to the changes in propulsion

efficiency. Hence, the analysis of the propulsion efficiency was also the investigation on these components throughout the propulsion test, open water test and resistance test as all of the components which can be evaluated from these test results took part in the propulsion efficiency, η_D. The value of propulsive efficiency could give the idea about the main engine power installation and then the losses between the parts through the propulsion system of the ship. The following sub-sections describes the comparison between components that can lead to becoming difference in the value of propulsion efficiency for different cases when the propeller position was changed behind hull with and without rudder conditions.

5.2.2. Investigation on Results of Propeller Hydrodynamics Performance in Model Scale and Full-Scale Prediction

The efficiency of the propulsion system is strongly dependent on propeller performance, thrust force, torque of propeller and its efficiency. Therefore, the simple method for investigation of marine propeller hydrodynamic performance is used to getting graphs of the propeller performance coefficient (K_T, K_Q, η_0) with respect to advance coefficient (J). In this thesis, the numerical reverse open water simulation was performed and the open water graph was evaluated and extrapolated into full scale open water graph with scale effect considerations. The results of K_T, K_Q and η_0 for model scale and full scale were assessed according to ITTC 1978 procedure and determined at self-propulsion point (n_M = 11.71 rps) for each case of four cases from the numerical propulsion simulations with and without rudder conditions at constant vessel's speed V_S = 12knots.

As shown in Figure 46, the model thrust coefficient (K_{TM}) was calculated from the model propeller thrust operating behind hull at self-propulsion point. For propulsion simulation with rudder condition, the model propeller thrust at Case1 is slightly lower than that at CaseOrig while Case2 is almost the same value as that of CaseOrig. The model propeller thrust is produced more less at Case3 compared to CaseOrig. The trend line of difference in model propeller thrust for Case1,2,3 and Orig for propulsion simulations without rudder condition is the same as that for all cases in propulsion simulation with rudder condition. The propeller thrusts for all cases are significantly reduced when the propulsion simulations were performed without rudder.

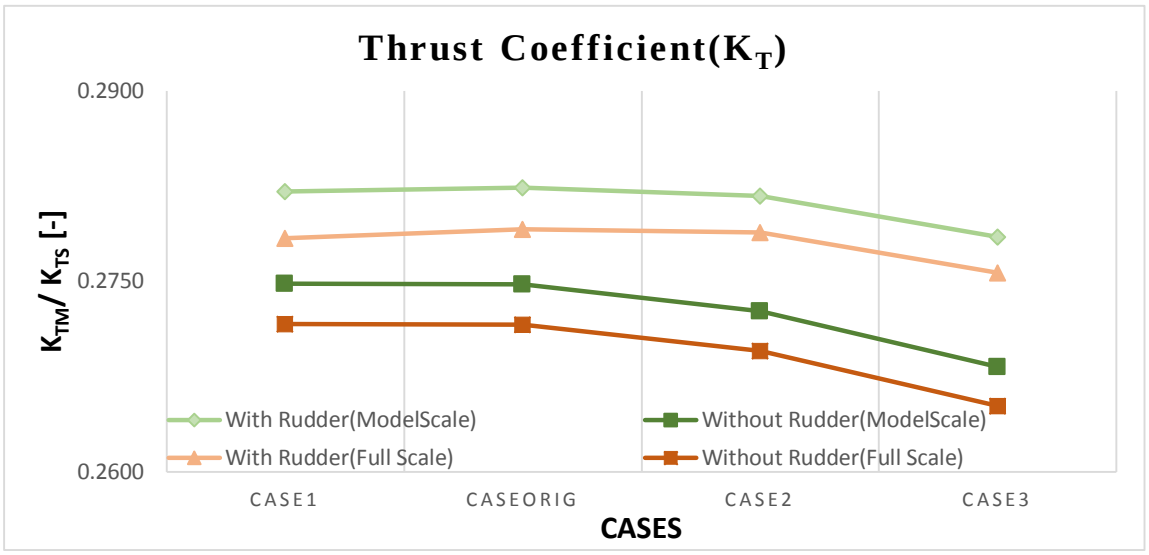

Figure 46 Thrust Coefficient K_T Results of Model Scale and Full-Scale Prediction for Propulsion Simulation With/Without Rudder Conditions

The advance coefficient for model scale is depending on the thrust coefficient since the thrust identity approach is adopted. The model advance coefficient (J_M) was read at the model thrust coefficient (K_{TM}) on the model propeller open water graph. Therefore, the larger value of model thrust coefficient leads to the smaller value of model advance coefficient as can be seen in Figure 47. With rudder condition, J_M value for Case1 and Case2 have slight changed compared to CaseOrig while J_M value for Case3 has larger valve than that of CaseOrig. Without rudder condition, the similar shape of difference in J_M values occurred for all cases as the simulation with rudder condition. The values of JM for simulations without rudder are larger than that for simulations with rudder because of smaller propeller thrust coefficient in model scale without rudder condition.

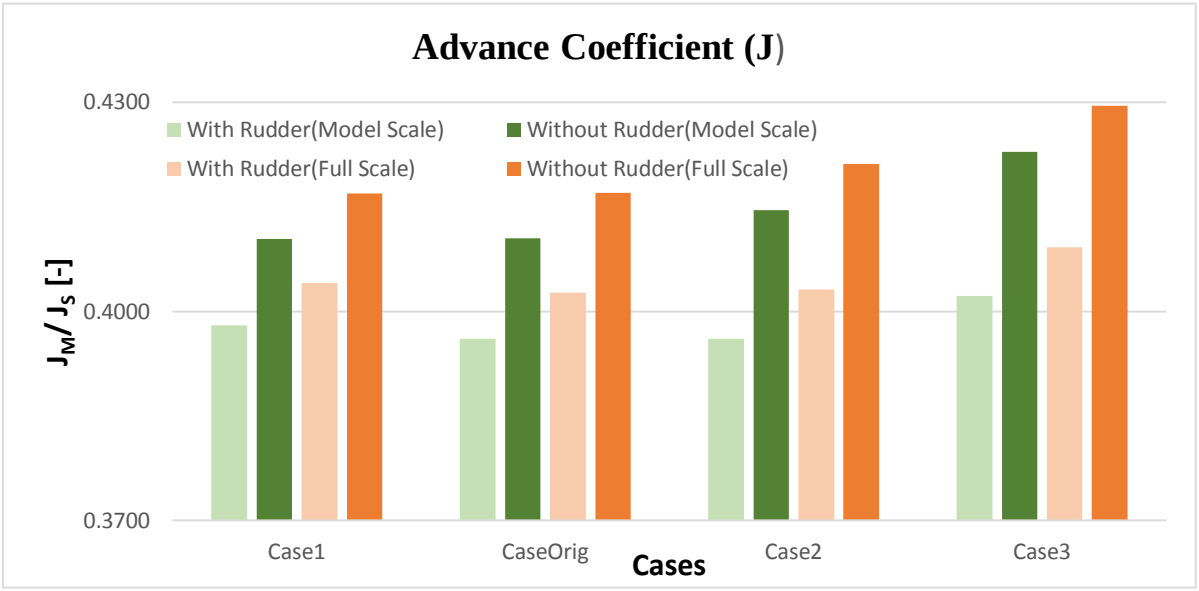

Figure 47 Advance Coefficient J Results for Model Scale and Full-Scale Prediction for Propulsion Simulation With/Without Rudder

Prediction for full-scale propeller thrust coefficient (K_{TS}) values at self-propulsion point for all cases were evaluated by intersecting the scaled K_{TS} curve and the load curve K_T/J^2 ratio plotted on the full scale open water graph which is mentioned details in *Section 4.4*. The full scale advance coefficient J_S value is read according to the intersection point. The propeller load curve K_T/J^2 is depending on the full scale effective wake fraction w_{TS} (which is described in *Sub-section 2.4.4*) and the total resistance coefficient of the hull C_{TS}. The variations in w_{TS} could lead the changes in K_{TS} values. The smallest value is occurred at the Case3 regarding to CaseOrig for simulations with and without rudder condition. The difference between values of K_{TS} for Case1 and Case2 comparing to CaseOrig can be observed in Figure 46. The lower values of K_{TS} are also found in propulsion simulations without rudder condition than these with rudder condition. The full scale advance coefficient values increased with decreasing full scale thrust coefficient for all cases in with and without rudder conditions. Krasilnikov et al (2011) [48] mentioned that the analysis of calculation results shows that blockage of propeller slipstream by rudder results not only in increase of thrust produced by the blades, but also in change of hub contribution into the total thrust.

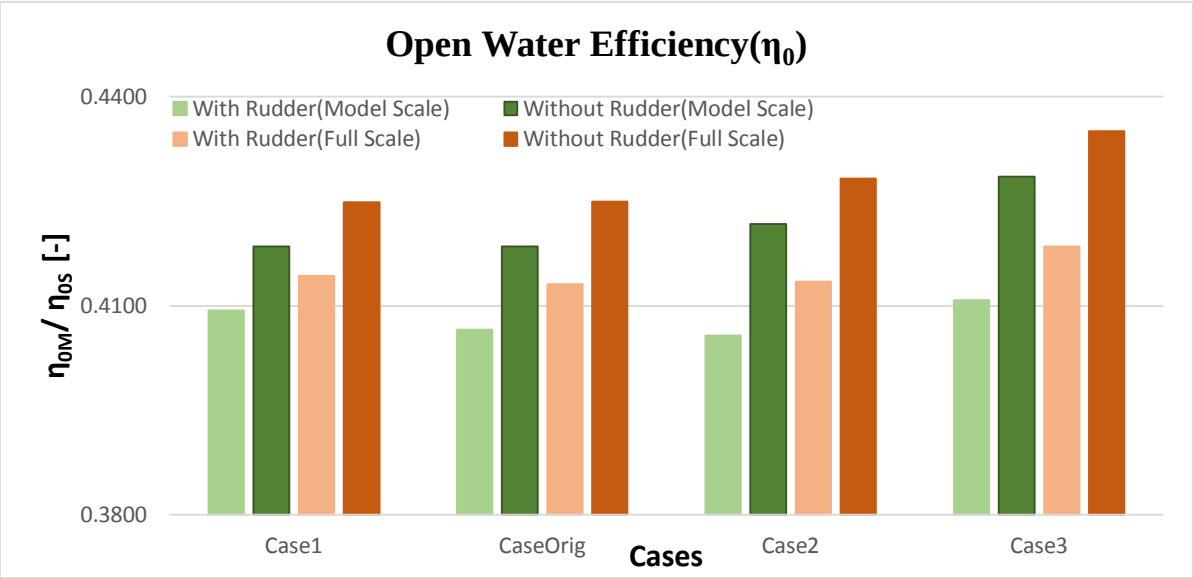

Figure 48 Comparison of Open Water Efficiency (η_0) Between Model Scale and Full Scale Prediction for Propulsion Simulation With/Without Rudder Conditions

In addition to the thrust, torque and advance coefficients, another open water characteristics, the open water efficiency η_0 can be expressed as

$$\eta_0 = \frac{P_T}{P_{D0}} = \frac{T.V_A}{2\pi nQ} = \frac{J}{2\pi} * \frac{K_T}{K_Q} \qquad (73)$$

The obtained open water efficiency is a function of thrust, torque and advance coefficients. The comparison of open water efficiency in model and full scale between four cases for with and

without rudder condition can be seen in Figure 48. The open water efficiency of Case3 is higher than that of CaseOrig and the other cases, Case1 and 2 has slightly deviations with CaseOrig. The model propeller open water efficiency (η_{0M}) is lower than full scale propeller open water efficiency (η_{0S}) for all cases with/without rudder since the advance coefficients in model scale are smaller than that in the full scale because of scale effects.

5.2.3. Investigation on Results of Relative Rotative Efficiencies (η_R) for Four Cases With/Without Rudder Conditions

The actual velocity of the water flowing to the propeller behind the hull is neither constant nor at right angles to the propeller's disk area, but has a kind of rotational flow. This rotation of the water has a beneficial effect. Therefore, compared with when the propeller is working in open water, the propeller's efficiency is affected by the η_R factor – called the propeller's relative rotative efficiency. [49] The efficiency of a propeller in the wake behind a hull is not the same as the propeller operating in open water. This is because:

- ❖ Level of turbulence in the flow is very low in an open water condition whilst it is very high in the wake behind the hull.
- ❖ The flow behind a hull is very non-uniform so that flow conditions at each radius at the propeller plane are different from the conditions in open water case. [50]

The propeller in open water, with a uniform inflow velocity at a speed of advance V_A, has an open water efficiency given by

$$\eta_0 = \frac{P_T}{P_{D0}} = \frac{T\,V_A}{2\pi n Q_0} \qquad (74)$$

where Q_0 is the torque measured in open water when the propeller is delivering thrust T at n rotations. Behind the hull, at the same effective speed of advance V_A, the thrust T and revolutions n will be associated with some different torque Q, and the efficiency behind the hull, η_B will be

$$\eta_B = \frac{P_T}{P_D} = \frac{T\,V_A}{2\pi n Q} \qquad (75)$$

The ratio of behind hull to open efficiencies under these conditions is called the relative rotative efficiency, being given by

$$\eta_R = \frac{Efficiency\ Behind\ Hull}{Efficiency\ in\ Open\ Water} = \frac{\eta_B}{\eta_0} = \frac{P_{D0}}{P_D} = \frac{Q_0}{Q} \qquad (76)$$

where P_{D0}: Delivered power in open water condition

P_D : Delivered power in behind condition

In this study for cases, the thrust identity approach was assumed when ITTC78 performance prediction was used to evaluate the propulsion parameter. Therefore, the model torque coefficient (K_{QM}) was evaluated at the self-propulsion point from the model propulsion simulations with/without rudder condition which in turn $Q_{M,}$ torque behind hull condition can be calculated. And then the model torque coefficient (K_{QTM}) was determined by using the model open water graph. The model propeller torque Q_{0M} in open water condition can be calculated by using K_{QTM} value. The results of K_{QM} and K_{QTM} evaluated for four cases can be seen in Figure 49. It is evident that the greater torque is produced in open water condition than that in behind hull condition as the difference in torque found behind hull and in open water is owing to two main reasons: the heterogenous wake, and the fact that the amount of turbulence in the water behind the hull is greater than in open water.

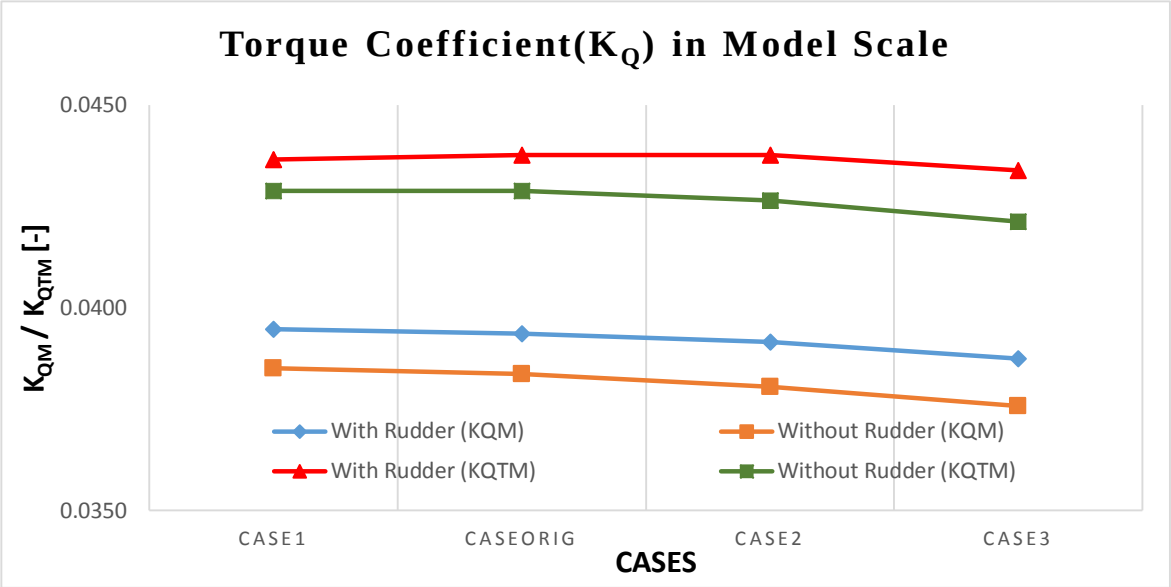

Figure 49 Results of Torque Coefficient K_Q for Model Propeller in Open Water Condition and Behind Hull Condtion of With/Without Rudder Conditions

In generally, we can say that the results of K_{QM} and K_{QTM} evaluated from propulsion simulations with rudder condition for all cases are larger than that without rudder condition since the values are depending on the thrust identity value K_{TM} and the larger values of K_{TM} are found simulations with rudder condition than without rudder condition. These differences between K_{QM} and K_{QTM} lead to the variation in relative rotative efficiency η_R for all cases.

The relative rotative efficiency η_R is defined as the ratio of the power delivered to a propeller producing the same thrust in open water (P_{D0}) and in behind (P_D) conditions and calculated by using model scale value of simulations in this study since the relative rotative efficiency is the

same for model scale and full scale condition. The comparison between relative rotative efficiency η_R for four cases with/without rudder conditions can be observed in Figure 50.

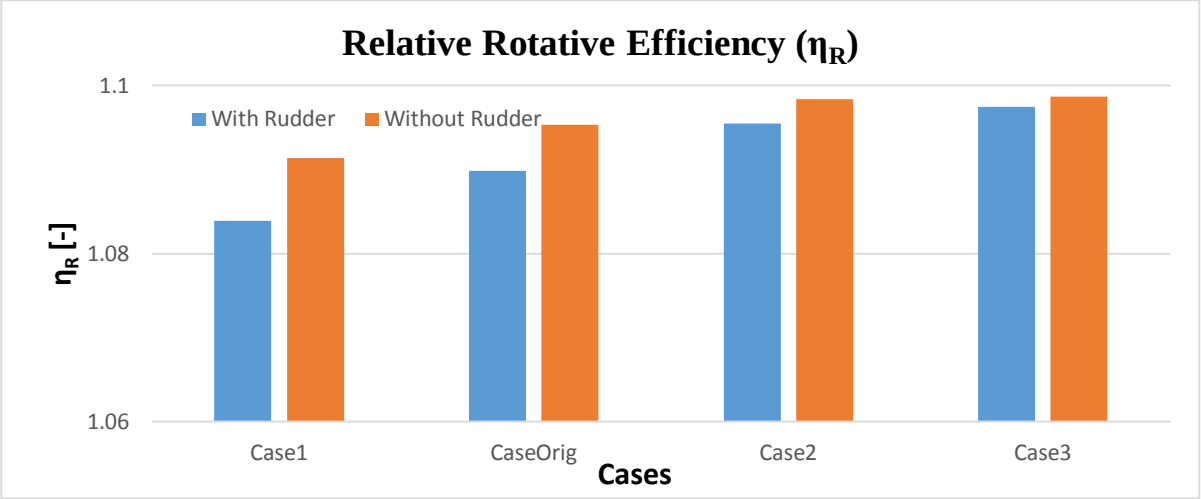

Figure 50 Comparison between Relative Rotative Efficiency η_R for Four Cases With/Without Rudder Conditions

According to above figure, the maximum relative rotative efficiency can be found in Case3 compared to CaseOrig for with/without rudder condition while that of Case1 is lower value than that of CaseOrig and that of Case2 has larger value than CaseOrig. Indeed, the higher efficiency values for all cases achieved without rudder condition than with rudder condition.

5.2.4. Investigation on Results of Hull Efficiency (η_H) for Four Cases With/Without Rudder Conditons

Thrust Deduction Fraction

When a hull is towed, there is an area of high pressure over the stern which has a resultant forward component reducing the total resistance. With a self-propelled hull, however, the pressure over some of this area is reduced by the action of the propeller in accelerating the water flowing into it, the forward component is reduced, the resistance is increased. [51] That means the propeller accelerates the flow ahead of itself, thereby (a) increasing the rate of shear in the boundary layer and, hence, increasing the frictional resistance of the hull and (b) reducing pressure (Bernoulli) over the rear of the hull, and hence, increasing the pressure resistance. In addition, if separation occurs in the afterbody of the hull when towed without a propeller, the action of the propeller may suppress the separation by reducing the unfavorable pressure gradient over the afterbody. [25]

Because of the above reasons, the action of the propeller is to alter the resistance of the hull (usually to increase it) by an amount which is approximately proportional to the thrust. This

means that the thrust (T) developed by the propeller must exceed the towed resistance of the hull (R_T). [50] Physically, this is best understood as a resistance augment.

In practice, it is taken as a thrust deduction, where the thrust deduction factor *t* is defined as

$$t = \frac{T - R_T}{T} = 1 - \frac{R_T}{T} \qquad (77)$$

The thrust deduction depends on streamlining and propeller clearances relative to the hull and rudder. It also increases with fullness. Thrust deduction, t is usually assumed to be the same for model and ship, although the friction component introduces a certain scale effect.

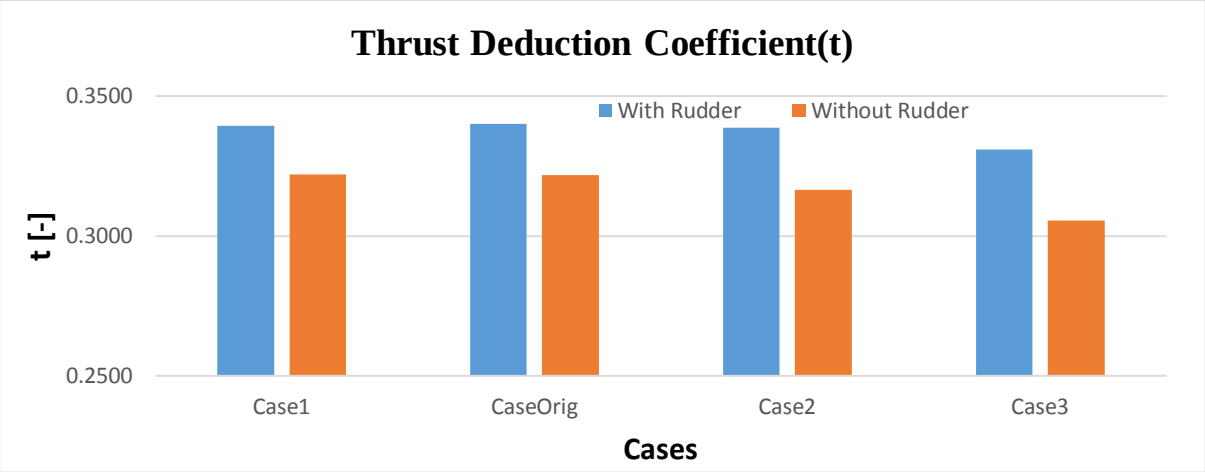

Figure 51 Comparison of Thrust Deduction Coefficient t for Four Cases With/Without Rudder Conditions

Figure 51 shows the evaluated values of thrust deduction for four cases with and without rudder conditions in this study. In simulations in this thesis, the thrust was produced differently according to the different propeller position while the resistance still remain the same. The thrust deduction became smaller when the less thrust is produced as can be seen in the Figure 51 & Figure 46. The lowest thrust is generated at Case3 compared to CaseOrig which leads to the lowest thrust deduction evaluated. The thrust deduction is smaller in simulations with rudder conditions for all cases compared to that without rudder.

Wake Fraction

When the ship is moving, the friction of the hull will create a so-called friction belt or boundary layer of water around the hull. In this friction belt the velocity of the water on the surface of the hull is equal to that of the ship, but is reduced with its distance from the surface of the hull. At a certain distance from the hull and, per definition, equal to the outer “surface” of the friction belt, the water velocity is equal to zero.

The thickness of the friction belt increases with its distance from the fore end of the hull. The friction belt is therefore thickest at the aft end of the hull and this thickness is nearly proportional

to the length of the ship. This means that there will be a certain wake velocity caused by the friction along the sides of the hull. Additionally, the ship's displacement of water will also cause wake waves both fore and aft. All this involves that the propeller behind the hull will be working in a wake field. The flow field around a propeller close to the hull is affected by the presence of the hull both because of the potential (non-viscous) nature and viscous nature (boundary layer growth) of the flow.

Therefore, and mainly originating from the friction wake, the water at the propeller will have an effective wake velocity V_w which has the same direction as the ship's speed V_S. This means that the velocity of arriving water V_A at the propeller, (equal to the speed of advance of the propeller) given as the average velocity over the propeller's disk area is V_w lower than the ship's speed V_S. The effective wake velocity at the propeller is therefore equal to $V_w = V_S - V_A$ and may be expressed in dimensionless form by means of the wake fraction coefficient w. The normally used wake fraction coefficient w given by Taylor is defined as:

$$w = \frac{V_W}{V_s} = \frac{V_s - V_A}{V_S} = 1 - \frac{V_A}{V_S} \qquad (78)$$

The value of the wake fraction coefficient depends largely on the shape of the hull, but also on the propeller's location and size, and has great influence on the propeller's efficiency. [49]

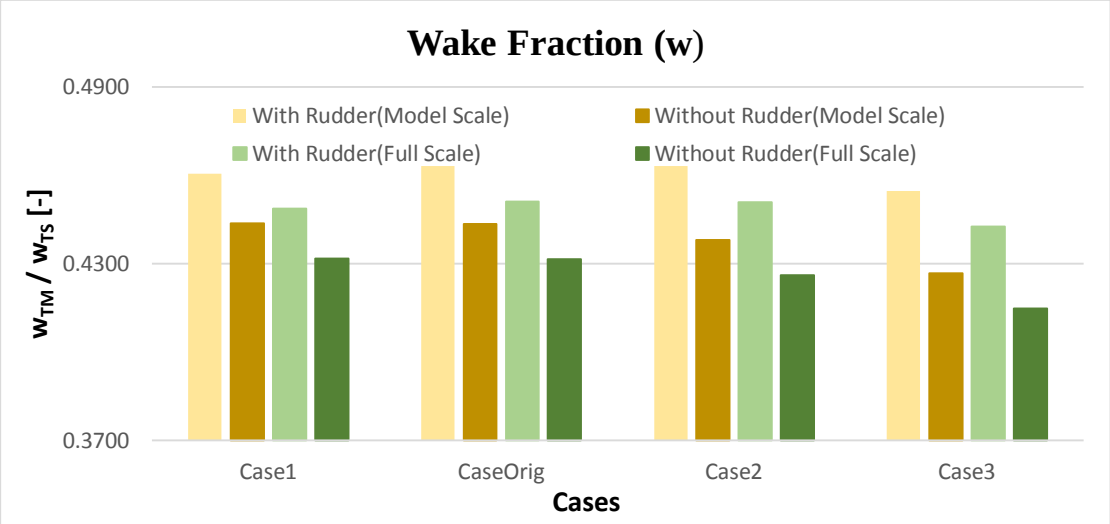

Figure 52 Comparison between Wake Fraction w in Model and Full Scale for Propulsion Simulations With/ Without Rudder Conditions

The wake fraction in model scale and full scale are different due to scale effects since the boundary layer in ship scale relatively thinner than in model scale that makes the viscous wake in ship scale is smaller. In this study, the model wake fraction w_{TM} and full scale wake fraction w_{TS} were evaluated and scaled by using ITTC78 procedure. Figure 52 shows the comparison between the wake fraction in model and full scale at self-propulsion point for propulsion

simulations with/without rudder conditions. Model wake fraction w_{TM} mainly depends on the advance velocity that means the model advance coefficient (J_M) values. The model wake fraction decreases with the increasing J_M values.

The full scale wake fraction w_{TS} is dependent on the thrust deduction factor t, model wake fraction w_{TM} and frictional resistance coefficient in model and full scale. The friction resistance coefficient for model and full scale is the same for all cases. The model wake fraction and thrust deduction factors are varying with respect to propeller positons and rudder consideration for four cases. Definitely, the wake fractions in model and full scale for all cases from propulsion simulations with rudder condition are reduced than these with rudder condition as can be seen in Figure 52. The wake fractions in model and full scale for Case3 are lower than that for CaseOrig. Case1 has higher value than CaseOrig while Case2 has less value compared to CaseOrig.

Hull Efficiency (η_H)

The work done in moving a ship at a speed V_S against a resistance R_T is proportional to the product R_T V_S or the effective power P_E. The work done by the propeller in delivering a thrust T at a speed of advance V_A is proportional to the product T V_A or the thrust power P_T . The ratio of the work done on the ship by that done by the propeller is called the hull efficiency, η_H, so that

$$\eta_H = \frac{P_E}{P_T} = \frac{R_T V_S}{T\, V_A} = \frac{1-t}{1-w} \qquad (79)$$

For most ships this is greater than one. At first sight this seems an anomalous situation in that apparently something is being obtained for nothing. It can, however, be explained by the fact that the propeller is making use of the energy which is already in the wake because of its forward velocity. [51]

Since hull efficiency η_H depends on the thrust deduction and wake fraction, the difference between the values of hull efficiency η_H for Case1, 2 and 3 comparing to CaseOrig for with/without rudder conditions can be observed in Figure 53. Due to the model wake fractions difference between four cases, the full scale wake fractions changes which results in the diversity of hull efficiency. It caused because of the variations of thrust deduction fraction. The hull efficiency reduces for simulations without rudder compared to these with rudder condition. Values at Case3 is the smallest compared to CaseOrig while that at Case2 got the highest value.

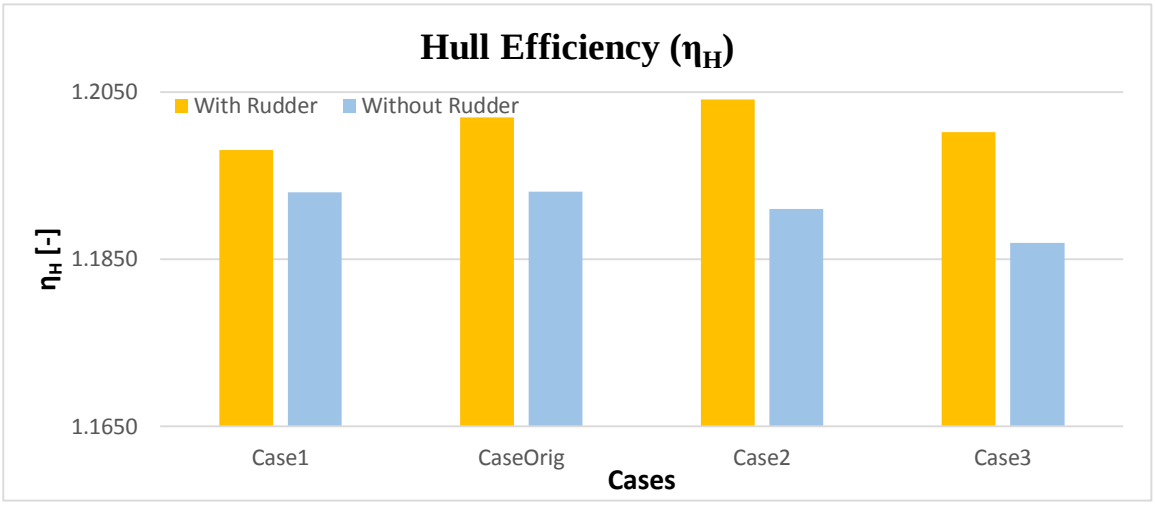

Figure 53 Comparison of Hull Efficiency η_H between Four Cases for Simulaions With/Without Rudder Conditions

Knutsson and Larsson(2011) [7] achieved the similar trend for the results of thrust deduction, wake fraction and hull efficiency as the results obtained in this present thesis work when the propeller is moving aft behind the hull. The thrust deduction factor t and wake fraction w_{TM} drops when moving the propeller away from the hull. The drop for wake fraction w_{TM} is not large as that of t.

5.2.5. Investigation on Results of Delivered Power (P_D) and Propulsion Efficiency (η_D) for Four Cases With/Without Rudder Conditions

The power delivered at the propeller can be expressed by the torque and the rpm;

$$P_D = 2\pi n Q \qquad (80)$$

In this study, delivered power P_D can be calculated by using full scale revolution of propeller N_S ,rpm and full scale torque Q_S at the self-propulsion point for all cases. The results for P_D is shown in Figure 54 evaluated for four cases from propulsion simulations with/without rudder condition.

This power is less than the 'brake power' directly at the ship engine P_B due to losses in shaft and bearings. These losses are comprehensively expressed in the shafting efficiency η_S : $P_D = \eta_S \, . \, P_B$. The ship hydrodynamicist is not concerned with P_B and can consider P_D as the input power to all further considerations of optimizing the ship hydrodynamics. [18]

From the Figure 54, the results from propulsion simulations with rudder conditions for all case are lower than that from simulations without rudder conditions. The larger delivered power P_D occurred in Case1 compared to CaseOrig while the smaller delivered power P_D found in Case2.

The Case3 has the lowest delivered power P_D than CaseOrig. This happens due to the deviations in torque occurred in propeller revolution.

The powering estimation for main engine installation into three parts:

(1) The estimation of effective power

(2) The estimation of propulsion efficiency (η_D)

(3) The estimation of required power margins.

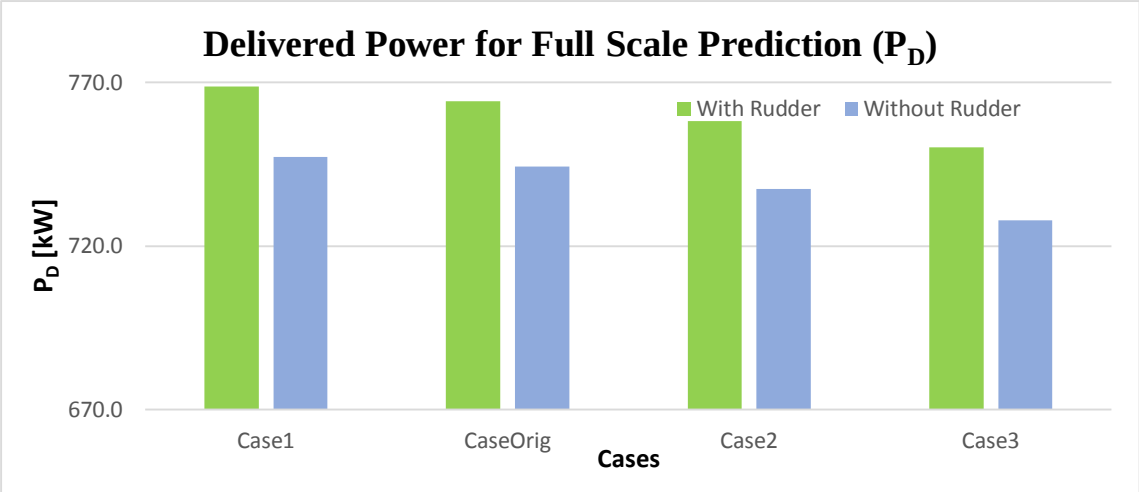

Figure 54 Results of Delivered Power P_D in Full Scale Prediction for Four Cases from Propulsion Simulations With/Without Rudder Conditions

The total installed power will exceed the delivered power by the amount of power lost in the transmission system (shafting and gearing losses), and by a design power margin to allow for roughness, fouling and weather, i.e.

$$Transmission\ Efficiency(\eta_T) = \frac{Delivered\ Power, P_D}{Power\ Required\ at\ Engine} \quad (81)$$

$$Installed\ Power\ (P_l) = \frac{P_E}{\eta_D} x \frac{1}{\eta_T} + margin \quad (82)$$

Once the propulsion efficiency is defined as

$$\eta_D = \frac{P_E}{P_D} = \eta_H \eta_0 \eta_R \quad (83)$$

The propulsion efficiency η_D has a major role for installed power estimation. By analyzing η_D values, the difference between Case1, 2 and 3 against CaseOrig can be found. The propulsion efficiency η_D is also a function of delivered power P_D and effective power P_E. In this study, effective power remains the same for all cases while the delivered power P_D differ in Case1, 2 and 3 from CaseOrig as can be seen in Figure 54 which leads to occur the deviations in propulsion efficiency η_D between four cases as shown in Figure 55.

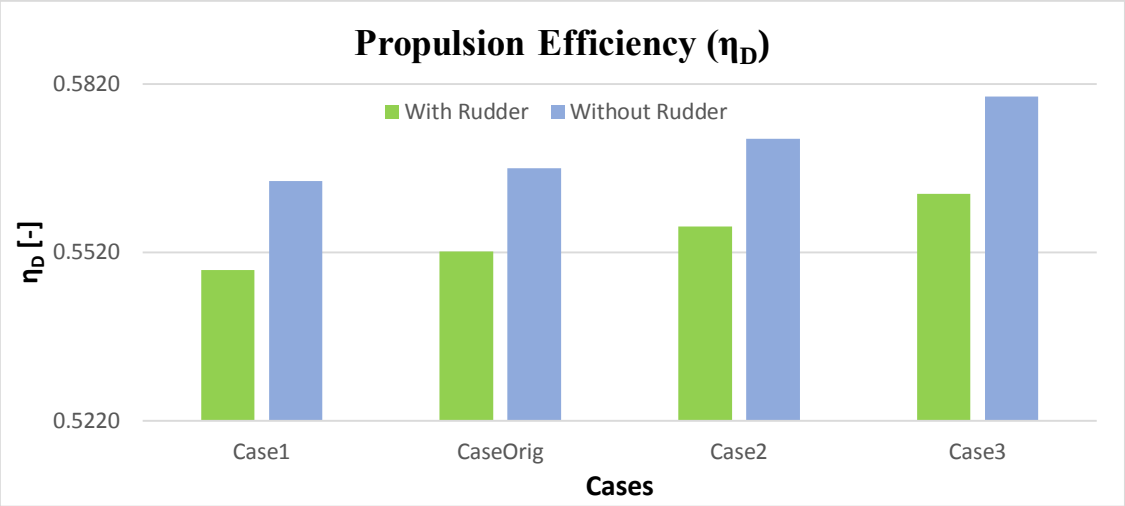

Figure 55 Comparison of Propulsion Efficiency η_D between Four Cases from Propulsion Simulations With/Without Rudder Conditions

According to Figure 54 & Figure 55, the higher delivered power P_D results in the lower propulsion efficiency. Generally, it can be seen that the propulsion simulations with rudder conditions for all cases achieve the smaller value of propulsion efficiency η_D than that without rudder conditions. As the investigation of propeller open water efficiency η_0 , relative rotative efficiency η_R and hull efficiency η_H gives the idea about changes in propulsion efficiency η_D. These three components have an effect on the propulsion efficiency η_D. Under these circumstances, the following summary can be made;

η_D [Case1] < η_D [CaseOrig] < η_D [Case2] < η_D [Case3]
with P_D [Case1] > P_D [CaseOrig] > P_D [Case2] > P_D [Case3]
η_D [With Rudder] < η_D [Without Rudder] {for all cases}
P_D [With Rudder] > P_D [Without Rudder] {for all cases}

For the propulsion simulations with rudder condition, the propulsion efficiency η_D of Case3 surpassing about 2% than that of CaseOrig. And then η_D of Case1 reduced about 0.6% than that of CaseOrig while Case2 achieved higher efficiency about 0.8% compared to that of CaseOrig.
The delivered power P_D is reduced about 2% in Case3 against CaseOrig while that in Case2 has lower delivered power P_D about 0.8% than that of CaseOrig. The achieving of lower delivered power P_D allows the smaller installation engine power required which can reduce the cost for main engine and the fuel consumption. The propulsion simulations without rudder condition gain the higher propulsion efficiency about 3% than simulations with rudder condition since

the required installation engine power is reduced with decreased delivered power P_D evaluated in simulations without rudder condition.

A.B.Phillips [52] replicated experiments performed by MOERI for the KVLCC2 operating at a Fn of 0.14 as numerical simulations by means of coupled RANS-BEMT approach. The numerical self-propulsion RANS simulations for this KVLCC2 hull and its corresponding propeller in model scale were carried out with&without rudder conditions, neglecting the free surface effects. The self-propulsion results with&without rudder conditions from his work has the same trend with the results of this thesis work. The propulsion efficiency is increased when the rudder is removed from the simulations.

He mentioned that the action of the propeller accelerates the flow and induces a swirl component. This travels downstream where it flows onto the rudder, significantly changing the flow around the rudder. The net result of the propeller action is an increase in the velocity and an effective angle of incidence, leading to an increase in rudder drag and the production of rudder lift with the rudder at zero incidence. The presence of the rudder modifies the flow upstream into the propeller, influencing the performance of the propeller. Blockage from the rudder reduces the flow velocity into the propeller, increasing the mean wake fraction resulting in an increase in the thrust and torque coefficients.

Krasilnikov et al (2011) [48] addressed that the numerical predictions confirm increase of propeller characteristics due to blockage of the slipstream by rudder, as registered in the tests. Both the thrust and torque of propeller become larger with increasing rudder angle, as the rudder blocks a greater part of the slipstream.

Therefore, the simulations with and without rudder conditions give the understanding of the influence of the rudder on the propeller and hull.

There are some ways to improve the propulsion efficiency since it depends propeller open water efficiency η_0 , relative rotative efficiency η_R and hull efficiency η_H . The propulsion efficiency can achieve with a hull form giving a high wake fraction coefficient w, and hence a high hull efficiency η_H, will also provide the best propulsive efficiency η_D. However, as the open water propeller efficiency η_0 is also greatly dependent on the speed of advance V_A and advanced coefficient J that is decreasing with increased w, the propulsive efficiency η_D will not, generally, improve with increasing w, quite often the opposite effect is obtained. Generally, the best propulsive efficiency is achieved when the propeller works in a homogeneous wake field. Indeed, the propeller position in the Case3 and Case2 is the suitable for increasing the propulsion efficiency in this study.

6. RESULTS FOR FLUID FLOW CHARACTERISTICS AND HULL PRESSURE DETERMINATION OF NUMERICAL PROPULSION SIMULATION IN MODEL SCALE

After performing the numerical propulsion simulations for four cases with constant model vessel's speed 3.8 knots at two model propeller's revolutions 11.61 rps and 11.81 rps, the self-propulsion point for each case was predicted at model propeller's revolution 11.71 rps and the full scale propulsion results were evaluated according to ITTC'78 performance prediction procedure. The propulsion simulations without rudder condition were performed at model propeller's revolution 11.71 rps with model vessel's speed 3.8 knots for all cases in order to compare and investigate the performance between propulsion simulations with and without rudder conditions. The investigation for propulsion efficiency was done for Case1, 2 and 3 compared to CaseOrig from the propulsion simulations with and without rudder condition. Therefore, this chapter will describe concerning the study of the fluid flow characteristics and hull pressure determination at certain points for numerical propulsion simulations operating at self-propulsion points for four cases with and without rudder conditions.

6.1. Results of Fluid Flow Characteristics in Numerical Propulsion Simulations in Model Scale

In this section, the fluid flow field in the numerical self-propulsion simulations in model scale for four cases with and without rudder condition is investigated when the simulations were carried out at the inflow velocity is at 1.95 m/s with operating model propeller revolution 11.71rps.

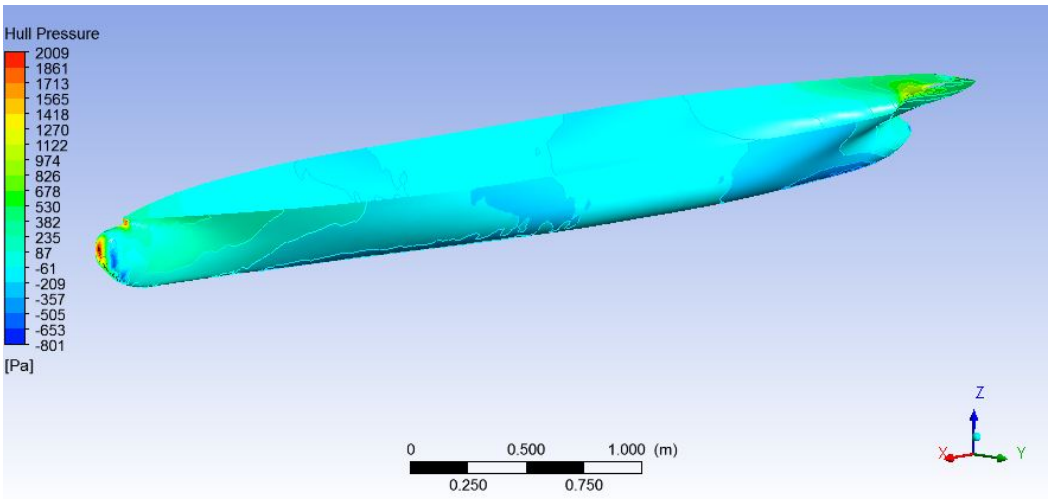

Figure 56 Pressure Distribution on Model Hull with Inflow Velocity 1.95 m/s

For every cases, the flow field on the hull can be summarized as the high pressure distribution is found in the bow region of the hull where the fluid flow is decelerated, and the pressure reduces along the body of ship hull. And then the pressure decreases again near the stern region of the hull starting to flow into the wake. The pressure rises in the stern region by forming the wake field with lesser velocities. The pressure around the hull can be seen in Figure 56.

These numerical self-propulsion simulations were carried out by adopting the sliding mesh approach with RANSE solver. The sliding mesh approach is a time-dependent approach in order to simulate the behaviour of the fluid flow field around the rotating propeller. In order to see the flow around the propeller, the non-dimensional axial velocity (wake) is measured at the upstream plane (x/R=0.3) and downstream plane (x/R=-0.5) around the propeller region as shown in Figure 57.

Removed due to Non-disclosure Agreement

Figure 57 Determination of Propeller Plane Positions and Hull Pressure Point Locations

When the flow reaches the stern region of hull, the flow separation causes in the stern region which effects the inflow fluid into the propeller. The upstream wake distribution for all cases with rudder condition and without rudder condition are as shown in Figure 58 & Figure 59. When the fluid flow past the upstream plane from the propeller plane, the effective wake in axial direction is observed that is resulted from the acceleration of the fluid flow because of propeller rotating action. According to Figure 58 & Figure 59, it is noted that the fluid is sucked by the propeller which can be seen from the contour inside the circle. The more fluid is sucked in Case1,2 and Orig compared to CaseOrig as the propeller blades are near to the hull in Case1,2 and Orig.

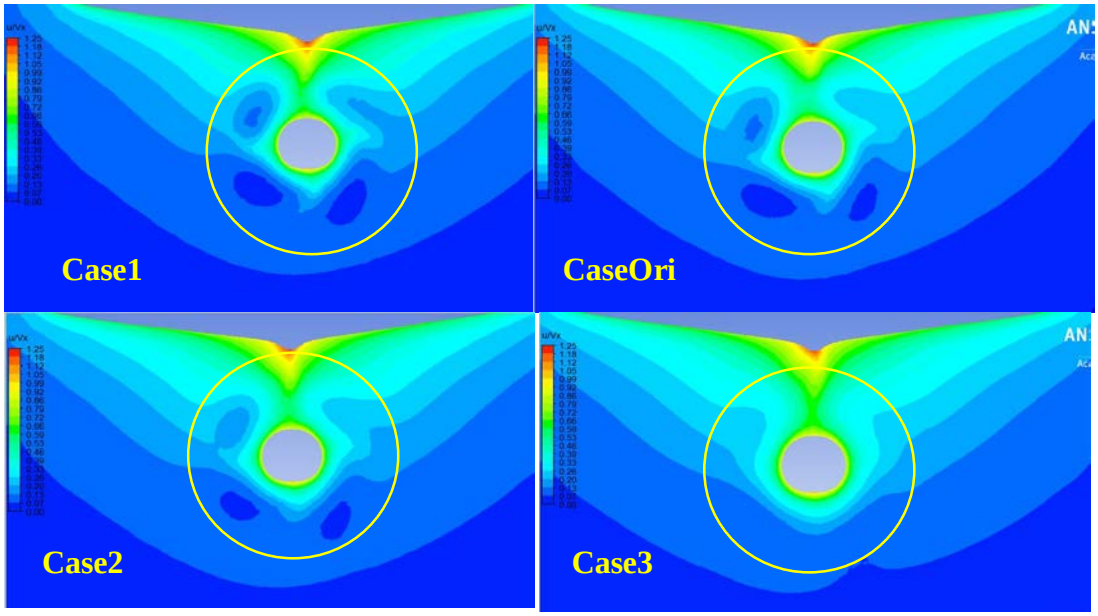

Figure 58 Axial Wake Distribution at Upstream Plane (x/R=0.3) from Propeller Plance in Model Scale For Four Cases (With Rudder Condition)

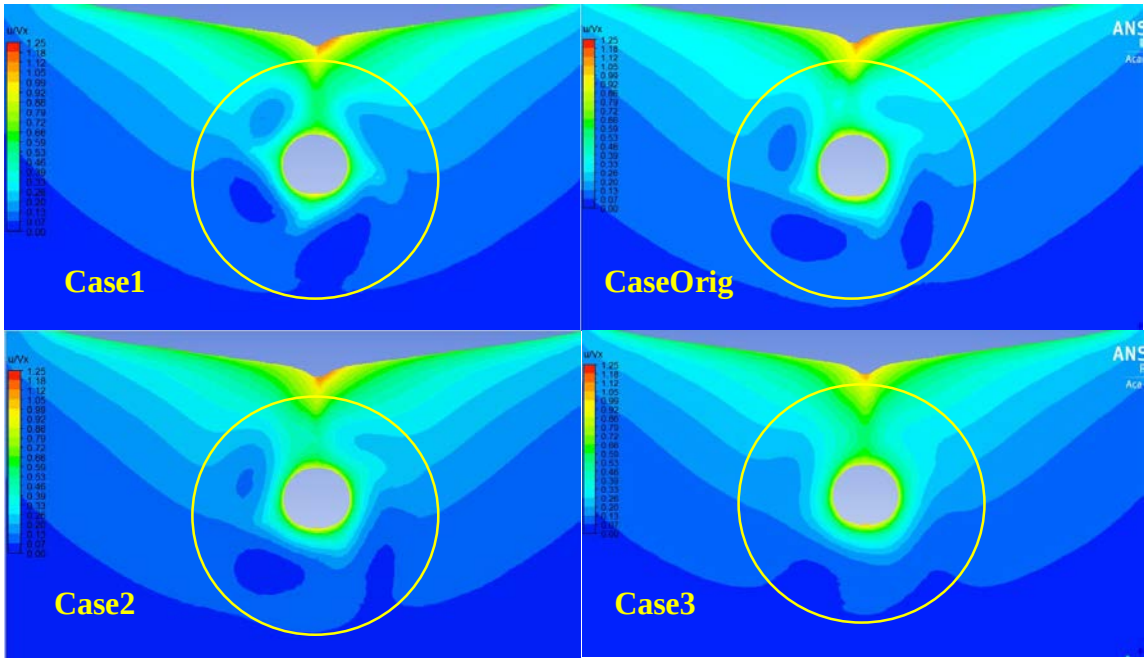

Figure 59 Axial Wake Distribution at Upstream Plane (x/R=0.3) from Propeller Plance in Model Scale For Four Cases (Without Rudder Condition)

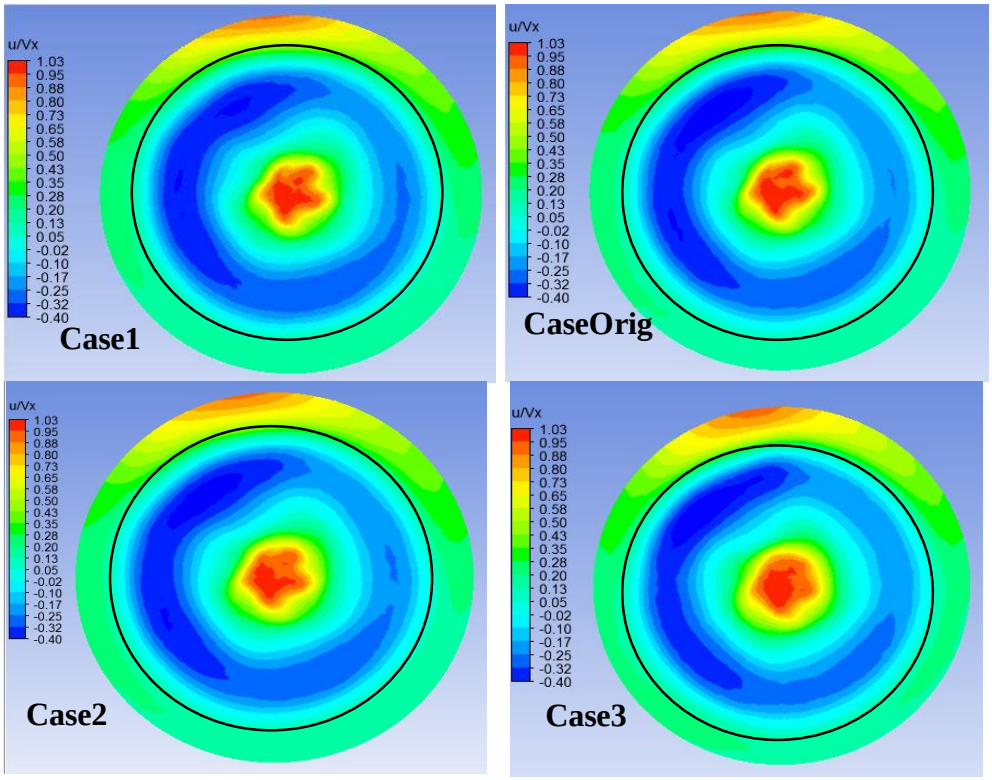

Figure 60 Axial Wake Distribution at Downstream Plane (x/R=-0.5) from Propeller Plance in Model Scale For Four Cases (With Rudder Condition)

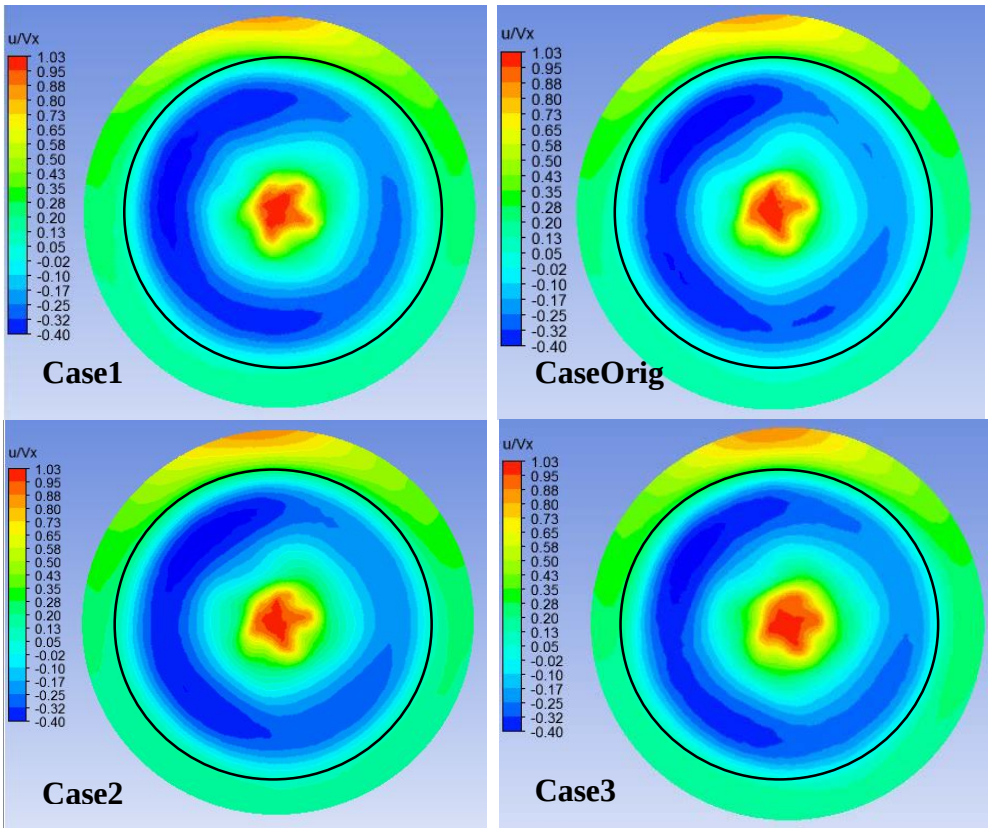

Figure 61 Axial Wake Distribution at Downstream Plane (x/R=-0.5) from Propeller Plance in Model Scale For Four Cases (Without Rudder Condition)

The downstream wake distribution in axial direction for all cases with rudder condition and without rudder condition are presented in Figure 60 & Figure 61. It is noticeable that the fluid flow has the effect of the asymmetric geometry by observing the axial wake distribution for both upstream and downstream plane. But, there is more asymmetry occurred when the fluid flow passes the downstream of the propeller than the upstream of the propeller.

The difference of the fluid flow pattern and axial wake distribution between four cases is agreeable with the investigation on the wake fraction that has been described in *Sub-section 5.2.4*. The lesser thrust is produced when the propeller moves away from the hull such as Case3. The simulation results without rudder condition gave less thrust than that with rudder condition. The higher thrust of the simulations results from the increasing axial velocity that can be observed in Figure 60 & Figure 61. The smaller wake distribution gave the lower thrust in the simulations.

The inflow into the propeller is markedly different in the upper and lower of the propeller plane. Above and upstream of the propeller axis, most of the inflow comes from the hull wake and the axial inflow velocity is small, closer to the propeller plane the flow is accelerated rapidly by the action of the propeller. The influence of the swirl results in asymmetric axial velocity inflow

conditions either side of the vertical centre axis. The asymmetric inflow conditions may potentially lead to cavitation, noise and pressure fluctuations on the hull. [52]

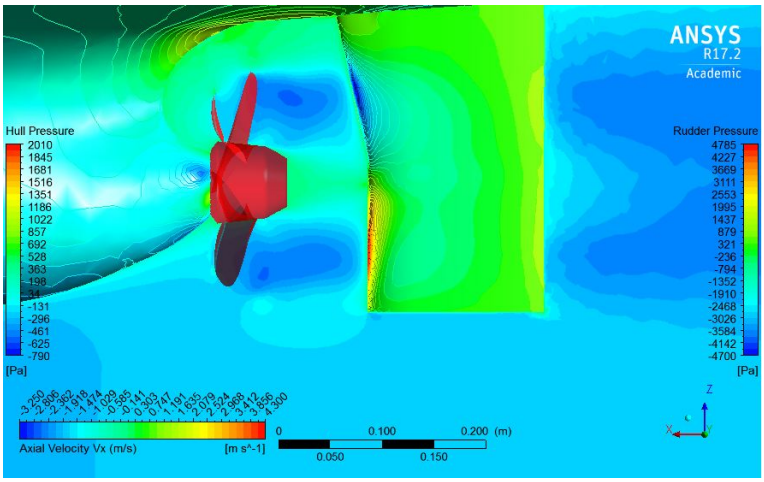

Figure 62 Pressure Distribution on Stern of The Hull and Rudder with Axial Velocity Field in Mid Plane (Port Side View) For Case1 with Rudder Condition

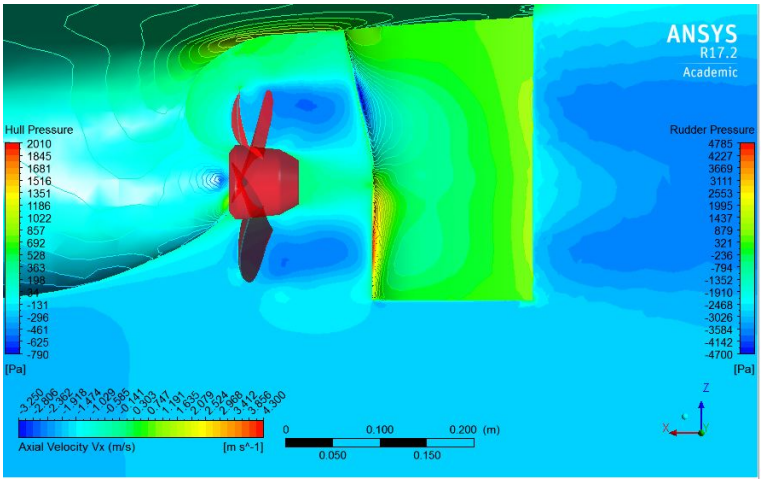

Figure 63 Pressure Distribution on Stern of The Hull and Rudder with Axial Velocity Field in Mid Plane (Port Side View) For CaseOrig with Rudder Condition

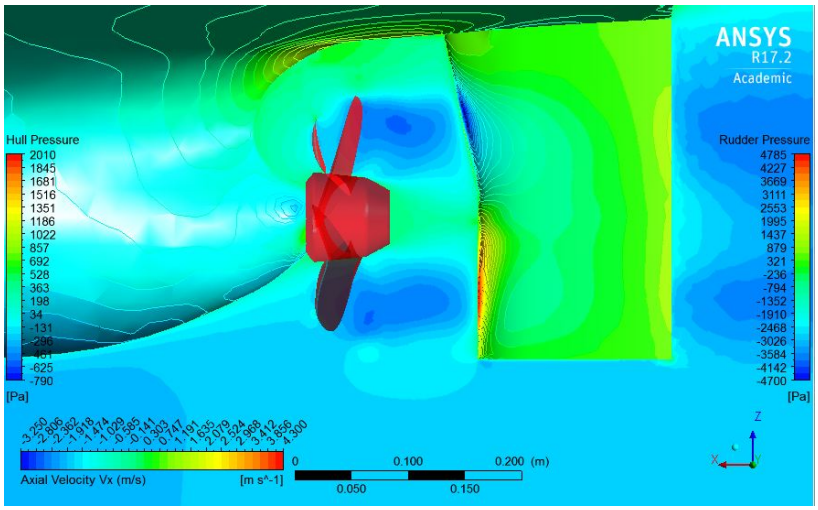

Figure 64 Pressure Distribution on Stern of The Hull and Rudder with Axial Velocity Field in Mid Plane (Port Side View) For Case2 with Rudder Condition

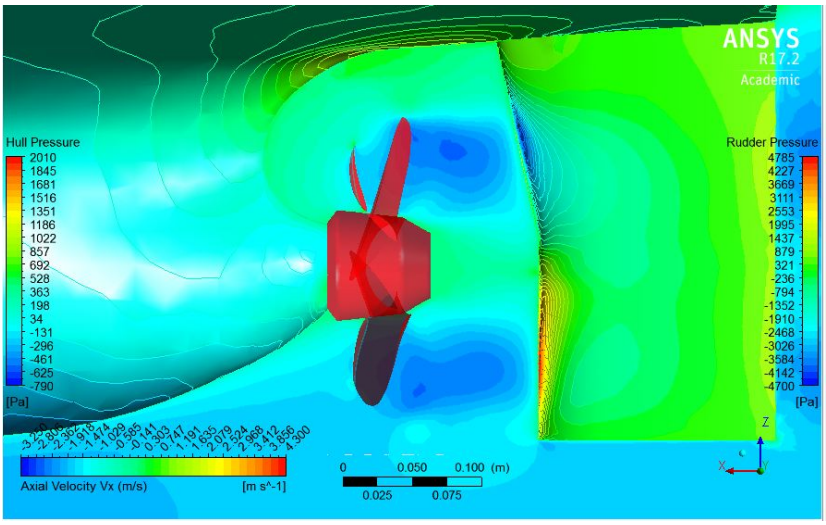

Figure 65 Pressure Distribution on Stern of The Hull and Rudder with Axial Velocity Field in Mid Plane (Port Side View) For Case3 with Rudder Condition

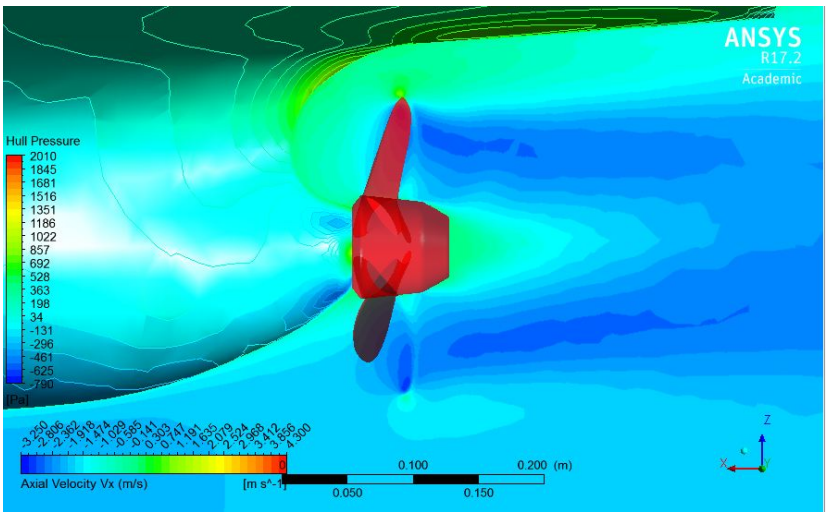

Figure 66 Pressure Distribution on Stern of The Hull with Axial Velocity Field in Mid Plane (Port Side View) For Case1 without Rudder Condition

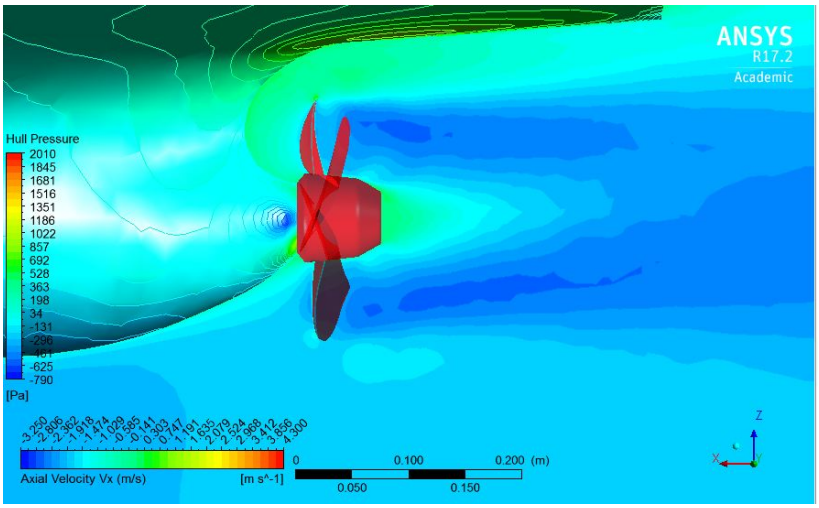

Figure 67 Pressure Distribution on Stern of The Hull with Axial Velocity Field in Mid Plane (Port Side View) For CaseOrig without Rudder Condition

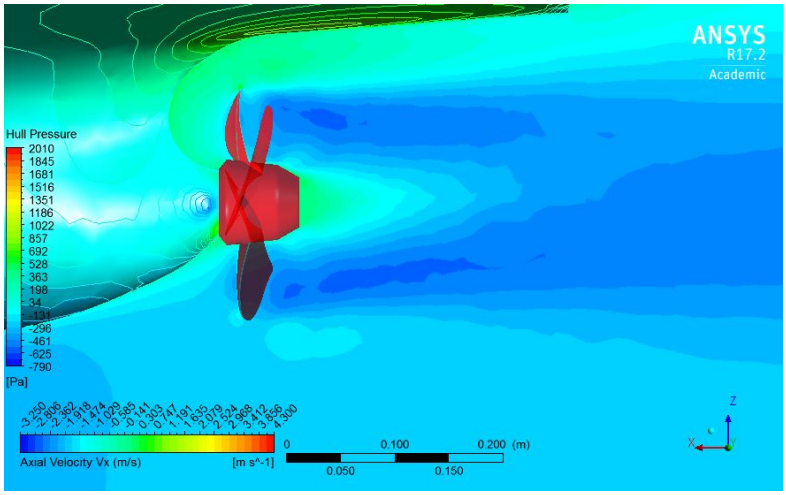

Figure 68 Pressure Distribution on Stern of The Hull with Axial Velocity Field in Mid Plane (Port Side View) For Case2 without Rudder Condition

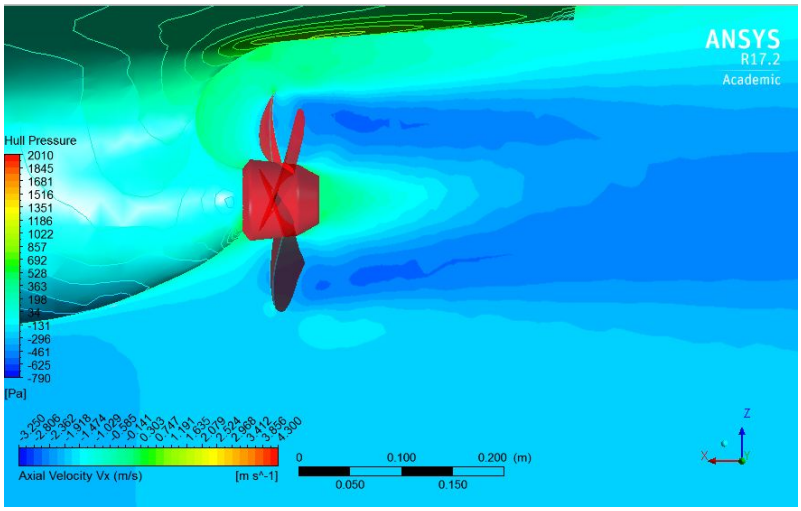

Figure 69 Pressure Distribution on Stern of The Hull with Axial Velocity Field in Mid Plane (Port Side View) For Case3 without Rudder Condition

A study of the field quantities, i.e. velocities and pressure in the stern region shows a time varying, but periodic flow field, which to a high degree is related to the blade frequency of the rotating propeller. Above figures (Figure 62 to Figure 69) show the pressure field in the stern region and the axial velocity contours in a cross section at the rudder position. With respect to the velocity field, it shows that the propeller accelerates the flow and introduces swirl in the flow downstream of the propeller.

Consequently, the rudder sees an accelerated rotating flow field, which results in varying angles of attack along the span of the rudder. The pressure field on the propeller blades themselves varies with the blade position due to the non-uniform inflow field in the wake field. Also the loading depends on whether the blades move upwards in the wake (starboard side) or downward (port side). The reason is that the cross flow, which has an upwards direction on both sides

results in different angles of attack for the blades which consequently experience different loadings.

The highest loading occurs on starboard side where the cross-flow and propeller motion have opposite directions. As seen the wake deficit of the hull strongly influences the propeller, but the propeller also influences the hull flow. The influence is most clearly seen in the pressure field. Upstream of the propeller the hull experiences suction, which reduces the pressure and increases the resistance. The effect is usually expressed as the thrust deduction.

Another region of the hull that feels the presence of the propeller is the region above the propeller. In this region the passing blades will introduce pressure pulses on the hull, which in critical cases can lead to noise or vibration problems in the structure. [5]

In the simulations without rudder condition, the flow field behind the propeller obviously differs from the simulations with rudder condition. In the simulations with rudder condition, the flow bounce back to the propeller because of rudder blockage that leads the increasing pressure on propeller and hull surface. This also causes the changes in thrust and torque produced from propeller between simulations with/without rudder conditions.

For simulations with rudder conditions, the Case3 contributes the more pressure distribution on rudder because the propeller position in Case3 is away from the stern of hull and near to the rudder in the simulations with rudder condition. This propeller position allows the lesser pressure exerting on the hull surface comparing to other cases. The Case1, 2 and Orig has the same fluid flow quantities for both conditions.

The propeller action also results in an increase of the resistance force acting on the hull due to the pressure decrease at the hull in the region upstream of the propeller. This is usually expressed as the thrust deduction fraction which has been investigated in *Sub-section 5.2.4.* The thrust deduction fraction is mainly influenced by this pressure decrease, but also by the altered shear stress distribution due to the propeller action.

There will be an increased mass flow through the volume of fluid where the propeller acts due to the propeller action, and a decrease of mass flow in the region around the propeller Figure 66, Figure 67, Figure 68 and Figure 69 . This means that the already low velocities in front of the top of the propeller reduce even further. In some cases, there is even a small region of flow separation on the hull directly above the propeller. [37] The velocity magnitude in tip of blades is higher than other region of blade surfaces. Because of the higher rotation in tips of blades, the momentum of fluid particles is very greater than near hub. [53]

The pressure distribution on the blades for all cases from simulations with and without conditons can be seen in below figures (Figure 70 to Figure 77).

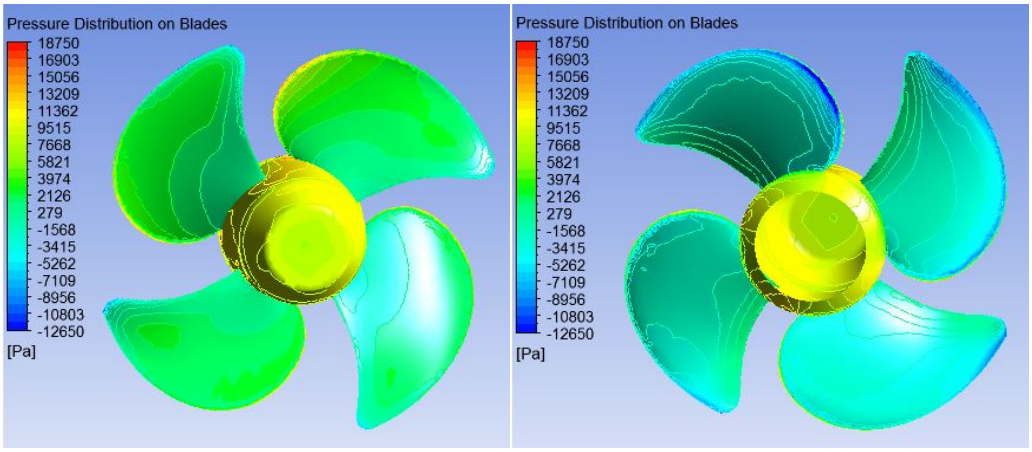

Figure 70 Pressure Distribution on Blades Resulted form Case1 Simulation with Rudder Condition [Left(Face) & Right(Back)]

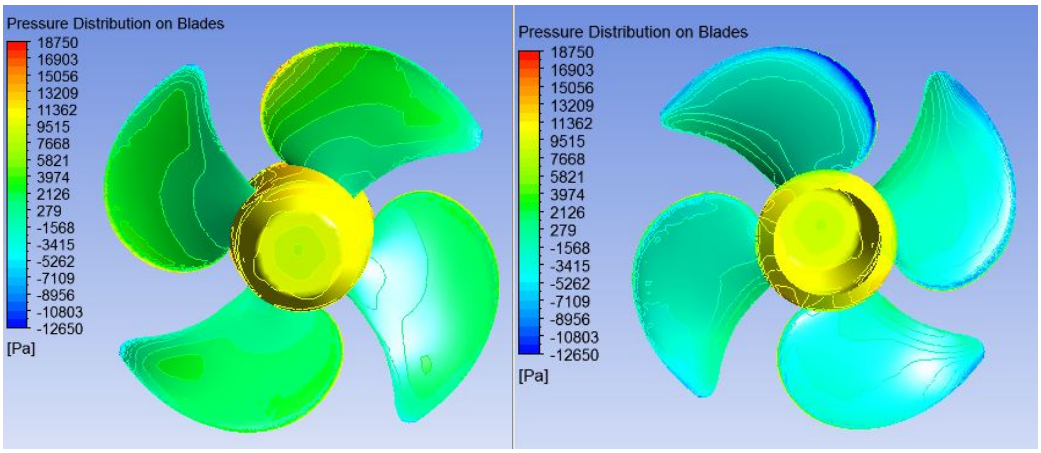

Figure 71 Pressure Distribution on Blades Resulted form CaseOrig Simulation with Rudder Condition [Left(Face) & Right(Back)]

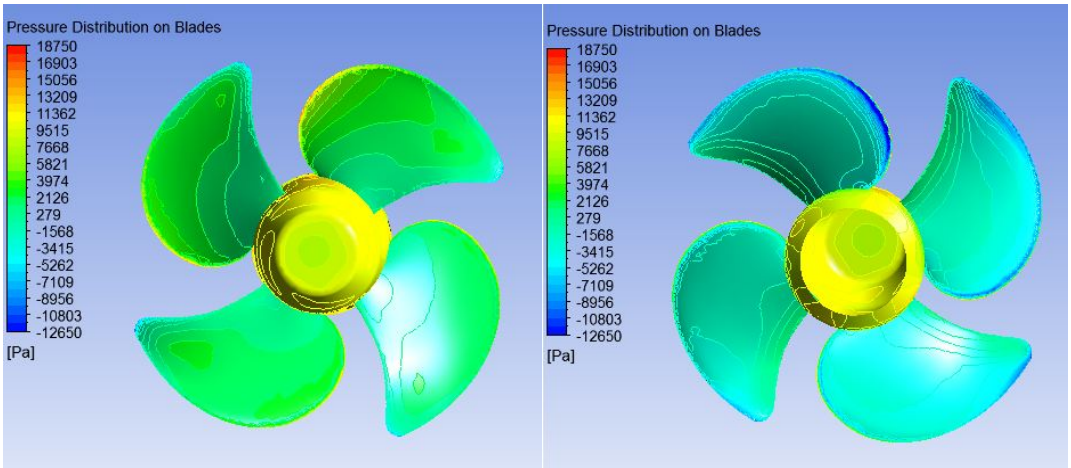

Figure 72 Pressure Distribution on Blades Resulted form Case2 Simulation with Rudder Condition [Left(Face) & Right(Back)]

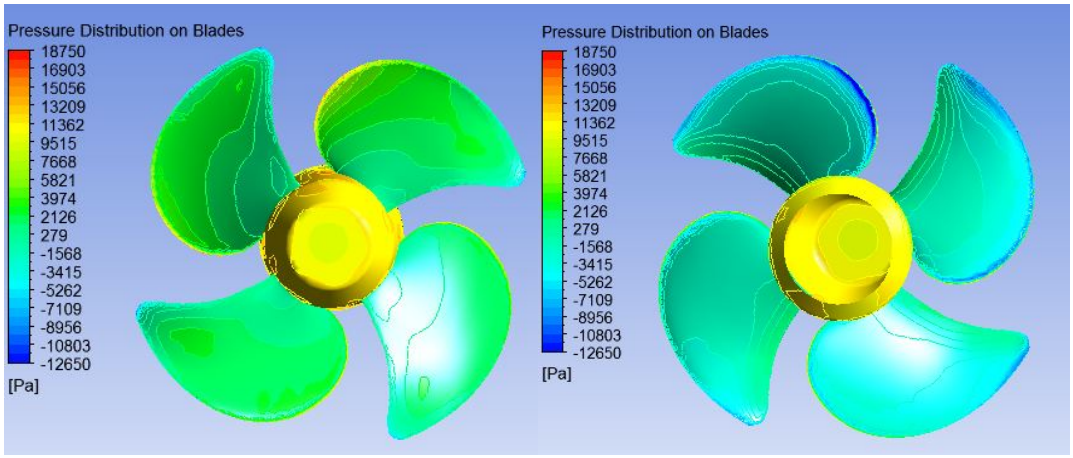

Figure 73 Pressure Distribution on Blades Resulted form Case3 Simulation with Rudder Condition [Left(Face) & Right(Back)]

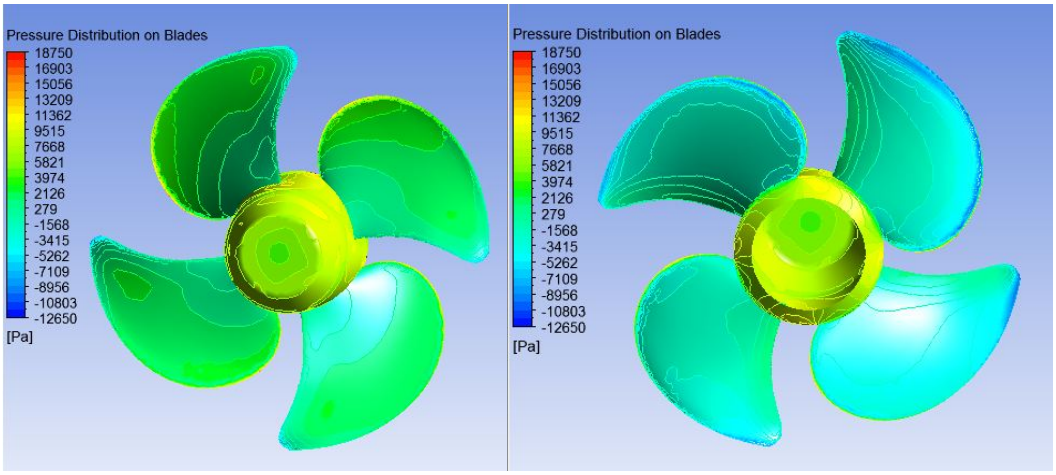

Figure 74 Pressure Distribution on Blades Resulted form Case1 Simulation without Rudder Condition [Left(Face) & Right(Back)]

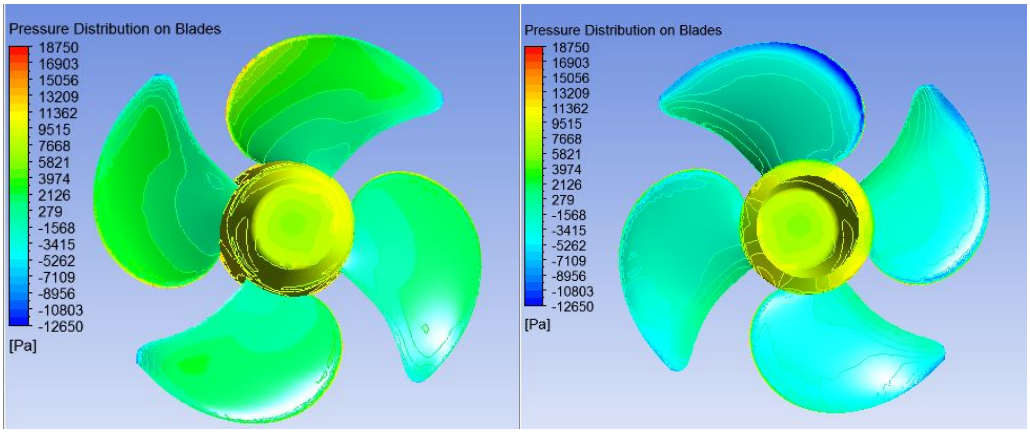

Figure 75 Pressure Distribution on Blades Resulted form CaseOrig Simulation without Rudder Condition [Left(Face) & Right(Back)]

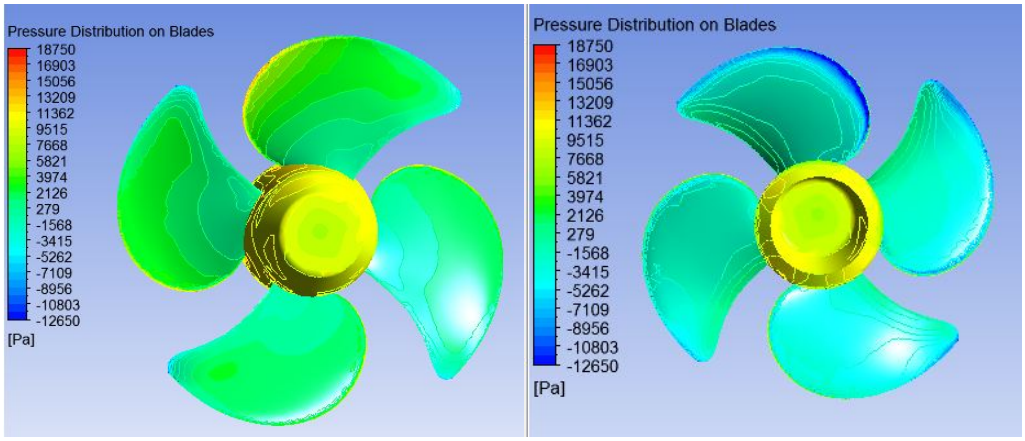

Figure 76 Pressure Distribution on Blades Resulted form Case2 Simulation without Rudder Condition [Left(Face) & Right(Back)]

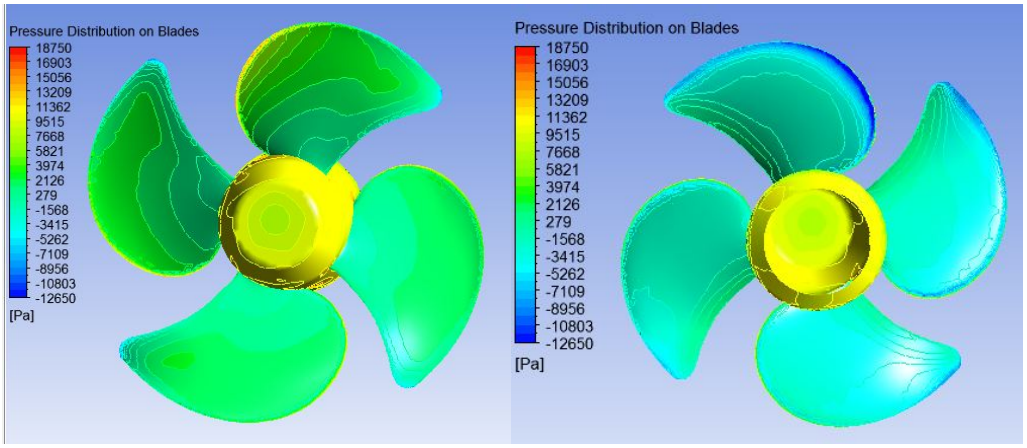

Figure 77 Pressure Distribution on Blades Resulted form Case3 Simulation without Rudder Condition [Left(Face) & Right(Back)]

According to the above figures (Figure 70 to Figure 77), it is evident that the pressure distribution between the face and back of the pressure shows the pressure gap between these two sides. The face is experiencing the high pressure while back is experiencing the low pressure. These pressure distribution explains the development of thrust produced by the propeller. The maximum value of the pressure on the blade at blade leading edge as it is the first point meets water for all cases. In the leading edge on the face and back, the high pressure values are captured. Therefore, in the leading edge area, the large pressure deduction will produce efficient thrust force for the propellers. According to the pressure distribution, it is important to outline that the cavitation probability on the tip blades on the back side of the propeller is noticeable. The flow field in the region around the stern of the hull, the propeller velocities and pressures display a time varying flow field. And the pressure distribution on the propeller back is mostly the negative pressures while the propeller face has predominantly the positive pressures. On the individual blades the pressure varies with the blade position due to the non-uniform propeller inflow field in the wake field.

For the propellers running behind hull without rudder condition, the lower pressure on the face is found that the propellers operation with rudder condition to the axil velocity changes. In evidence, the lower pressure exerted on the back of the propeller when the propeller is placed away from the hull region that can be seen in the Case3. The lower pressure exerted on the back is observed in Case3 compared to other cases.

6.2. Determination of Hull Pressure at Pressure Tapping Points in Model Scale

This section describes about the prediction of the propeller-induced hull-pressure-fluctuations and the predicted values of hull pressure at pressure tapping points from the numerical simulations of the test cases in this thesis work.

The ship propeller acts as a source in various ways. One way is that time-varying shaft forces and moments directly excite the ship through the driving train (viz., the bearings and thrust block). Another way, the propeller causes pressure fluctuations in the surrounding water, which are transmitted as hydroacoustic waves to the hull plating above the propeller, which they excite. Propeller blades passing underneath the afterbody cause pressure fluctuations by their displacement effect as well as by the load they carry. When the local pressure in the water is low enough for it to evaporate, a phenomenon called cavitation, vapor pockets are generated. These vapor pockets are known as cavities. Due to variations in ambient pressure and blade loading during a revolution, the cavities may rapidly change in volume and location over time, thus causing pressure fluctuations in the surrounding water.

In order to meet comfort requirements for passengers and crew, propeller cavitation must be reduced by making adjustments to the ship and propeller design. This is often accompanied by a reduction of propulsive efficiency. Therefore, the prediction of efficiency and propeller-induced hull-pressure and excitation forces is essential in the assessment of the ship design. [54]

6.2.1. Hull Pressure Prediction

The hydrodynamic interaction between the propeller and the hull originates from the passage of the blades beneath or in the vicinity of the hull and also from the cavitation dynamics on the surfaces of the blades. The pressure differences caused by these two types of action are then transmitted through the water to produce a fluctuating pressure over the hull surface which, due

to its acting over a finite area, produces an excitation force to the vessel. Consider only the pressures produced by the rotating propeller rather than the resultant force on the hull, which is the integration of the pressure field over the hull surface, taking into account the curvature and form of the hull in the region of the propeller. Thus, the pressure on the propeller and its distribution as well as the resulting torque and thrust fluctuate during a revolution. These variations may evoke vibration of the propulsion system and a further transfer of the induced vibration into the hull structure can take place.

Model measurement methods of predicting hull surface pressures can be conducted in either cavitation tunnels or specialized facilities such as depressurized towing tanks. [47] It is the task of ship model basins to assist the ship designer, yard and ship owner in testing the ship design with regard to specific contract requirements. For this purpose model basins have developed prediction capabilities, which involve tests on scale models of ships as well as computational simulations of the hydrodynamics involved. [54]

Originally the arrangement in a cavitation tunnel comprised a simple modelling of the hull surface by a flat or angled plate above a scale model of the propeller. Although this technique is still used in some establishments a more enlightened practice is to use a dummy model with a shortened center body, as shown in Figure 78; however, in some large facilities the towing tank model is used. The advantage of using a model of the actual hull form is twofold: first it assists in modelling the flow of water around the hull surface and requires wake screens, which are essentially arrangements of wire mesh, for fine tuning purposes of the wake field, and secondly it makes the interpretation of the measured hull surface pressures easier since the real hull form is simulated. [47]

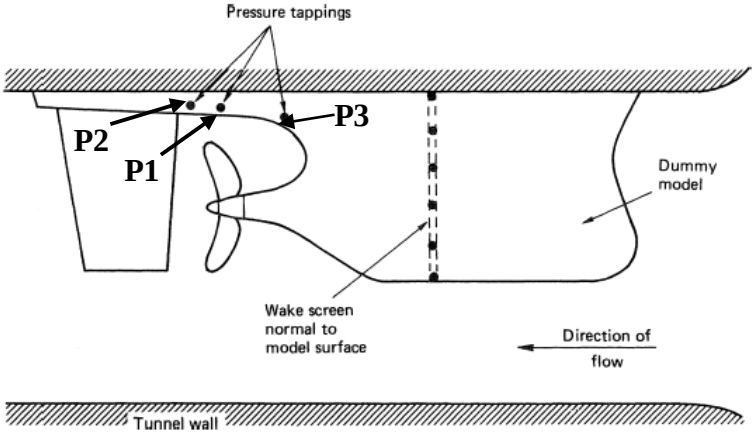

Figure 78 Dummy Model and Propeller in A Cavitation Tunnel [47]

In order to interpret model test results appeal can be made to dimensional analysis, from which it can be shown that the pressure at a point on the hull surfaces above a propeller has a dependence on the following set of dimensional parameters:

$$p = \rho n^2 D^2 \varphi\{J, K_T, \sigma, Rn, Fn, \left(\frac{z}{D}\right)\} \quad (84)$$

in which J is the advance coefficient, K_T is the propeller thrust coefficient, σ is the cavitation number, Rn is the Reynolds number, Fn is the Froude number and z is the distance from the propeller to the point on the hull surface.

As a consequence of this relationship a pressure coefficient K_p can be defined as

$$K_p = \frac{P}{\rho n^2 D^2} \quad (85)$$

which has the functional dependence defined in equation *(92)*. Equation *(92)* defines the hull surface pressure as a function of propeller loading, cavitation number, geometric scaling and Reynolds and Froude identity. The value of K_p between model and full scale are assumed as identity. [47]

6.2.2. Evaluation and Comparison of Hull Pressure at Pressure Tapping Points for Four Cases with/without Rudder Condition

In this study, the numerical self-propulsion simulations with and without rudder conditions are already carried out. Therefore, the mean hull pressure results from the numerical propulsion simulations were used to evaluate the hull pressure coefficient (K_P). The hull pressure values are measured at the points P1, P2 and P3 as shown in Figure 78 during the self-propulsion simulations were carried with the model propeller revolution of 11.71 rps at constant model vessel's speed 3.795knots for conditions of with and without rudder. The mean hull pressure fluctuations in model scale at three points are presented in Figure 79.

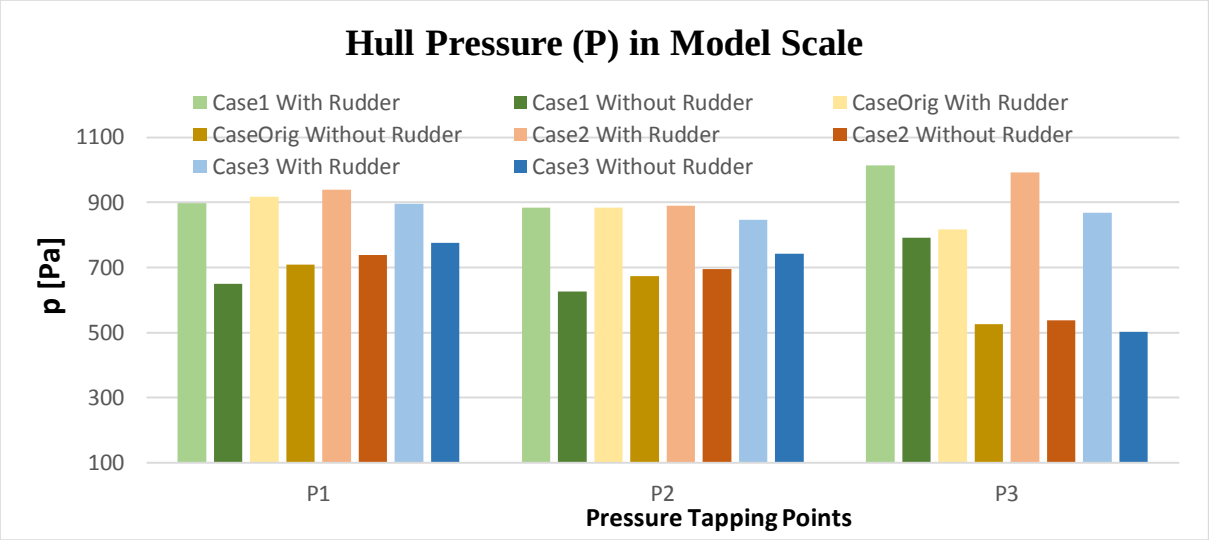

Figure 79 Comparison of Hull Pressure on Pressure Tapping Points For Four Cases with/without Rudder Condition

The evaluated non-dimensional pressure coefficient can be seen in Figure 80.

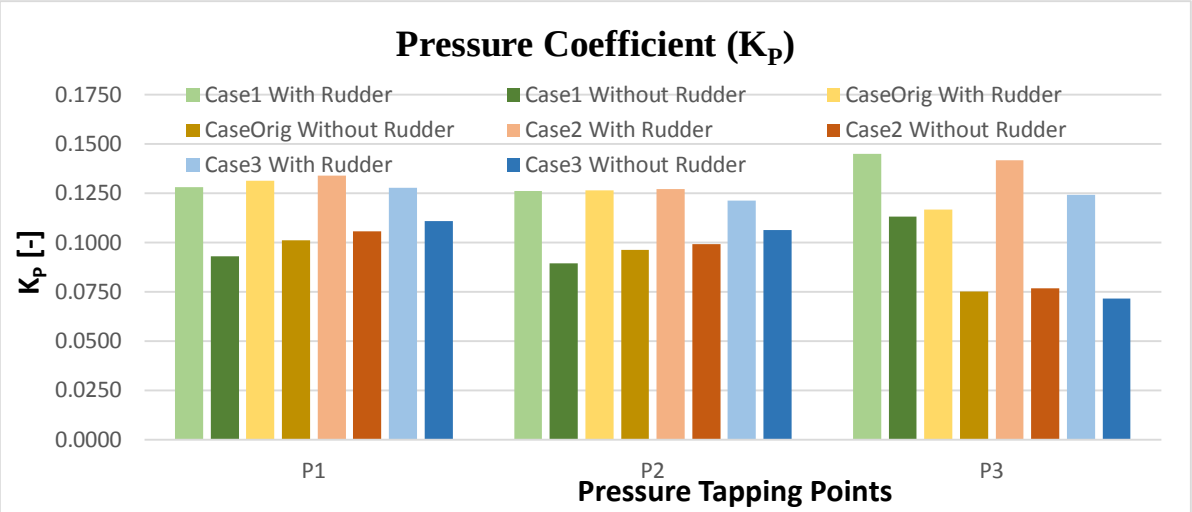

Figure 80 Comparison of Pressure Coefficient on Pressure Tapping Points For Four Cases with/without Rudder Condition

In accordance with Figure 79 & Figure 80, the pressure tapping point P3 has the highest pressure fluctuation. At that point, the model hull is experiencing the highest pressure when the propeller is located in the nearest position of the stern of the hull which is the Case1. The Case3 give the lowest value because the propeller is away from the hull curvature. Simulations without rudder achieve lesser hull pressure values as the fluid flow is swirling from the propeller downstream and rotating with high axial velocities from tip of the blade as shown in Figure 66. CaseOrig and Case2 has the similar pressure values on hull when the rudder is removed from the simulations.

The pressure tapping point P1 and P2 are located near the tip of the propeller blade which may suffer the pressure from the rotation of the tip of the propeller blade. As we can observe that the pressure fluctuations are reduced around 30% on the hull surface when the simulations were performed without rudder rather than these with rudder condition. Wijngaarden [54] found out that the maximum pressure fluctuations were occurred at the middle points located on the hull surface near the tip of the propeller blade.

Takafumi Karamuwa [55] mentioned that the distribution of the magnitude of the pressure fluctuation is almost symmetrical in non-cavitating condition. This is because the source of the pressure fluctuation in non-cavitating condition is the pressure field around the propeller blades, which rotates with the propeller. In this case, the magnitude of the fluctuation is dominated by the distance from the propeller blades and the shape of the hull. The magnitude of the fluctuation increases and the shape of the distribution changes in cavitating condition. The peak of the magnitude is shifted to the starboard side. This is because the propeller rotates in the

clockwise direction and the main source of the pressure fluctuation is the variation of the cavity volume. These tendencies are in qualitative agreement with the known facts.

Figure 81 shows that the pressure distribution on the hull surface for four cases resulting from the simulations with rudder condition. It is noticeable that the peak of the pressure is occurring in the middle of the hull with symmetrical pressure contribution on starboard and port sides It is obvious that the hull pressure on the stern region is lower in Case 2 and 3 than that in Case 1 and Orig. This is due to the distance between propeller tip and hull. The results of the simulation without rudder condition shown in Figure 82 has the same trend for the peak of the pressure in the middle of the hull with symmetrical pressure contribution on starboard and port sides. Generally, the peak pressure from the simulations without rudder condition is obviously lower than that with rudder condition. In Case1, the pressure distribution on the hull has slightly different shape from other cases since the propeller position is the nearest to the hull in this case. The lowest peak pressure is found in Case3 for both conditions of with&without rudder.

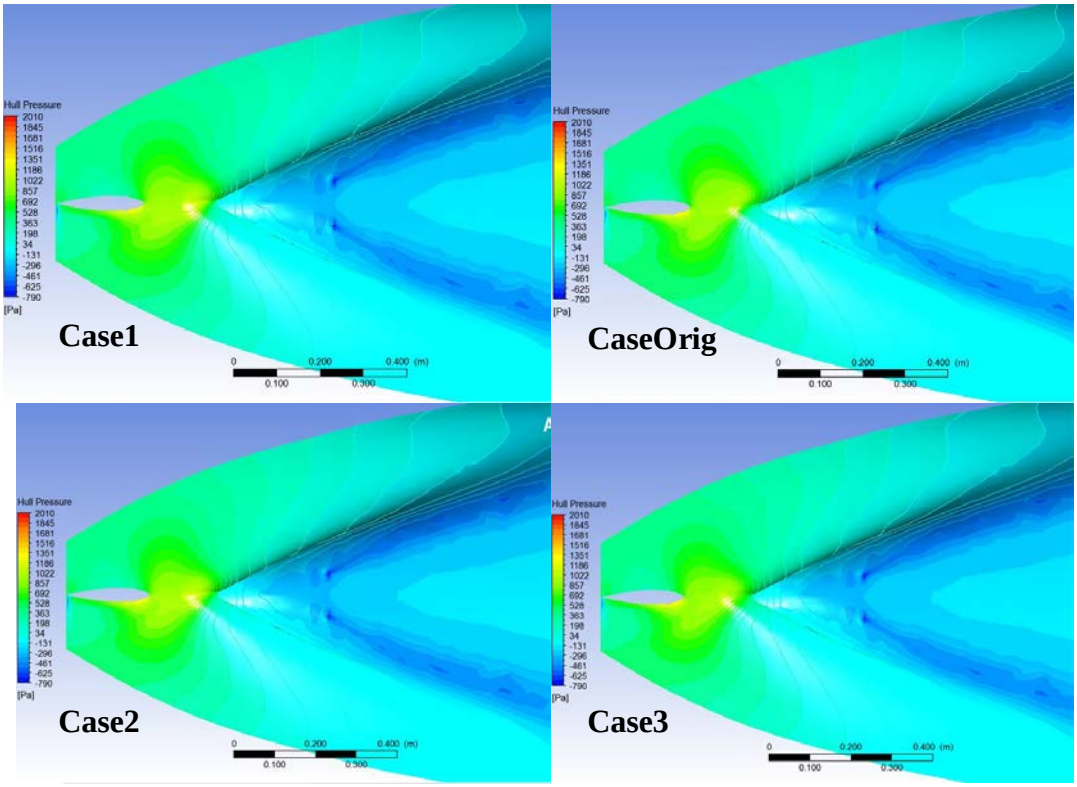

Figure 81 Distribution of Total Pressure Contour on Hull Surface for Four Cases from Simulations with Rudder Condition

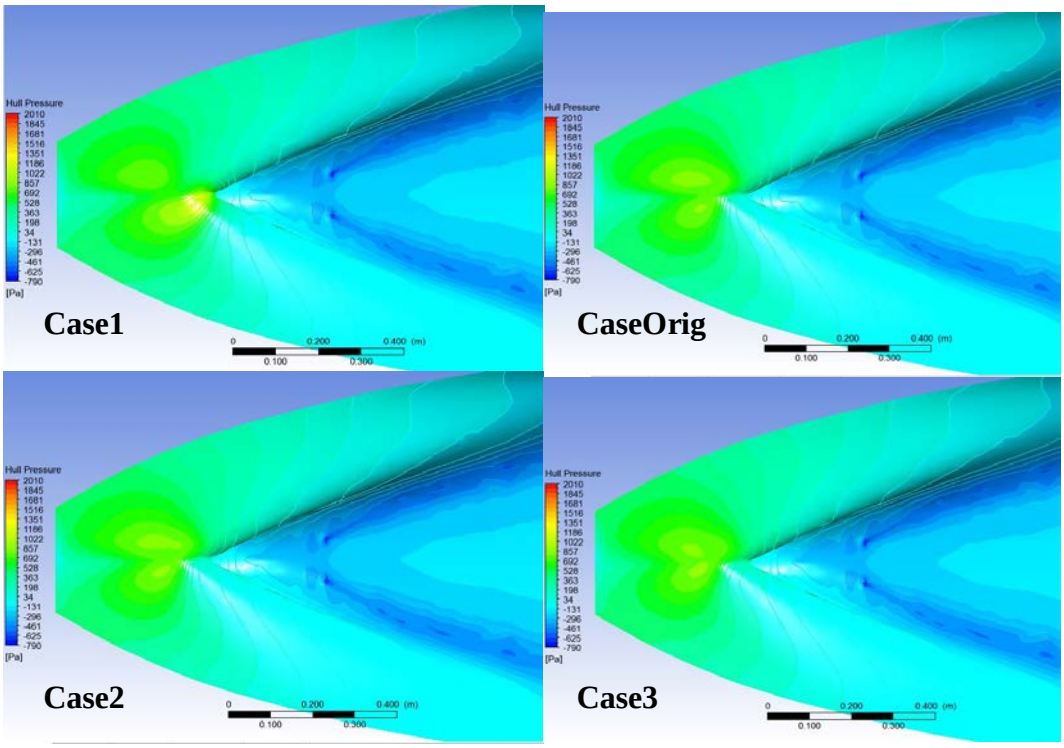

Figure 82 Distribution of Total Pressure Contour on Hull Surface for Four Cases from Simulations without Rudder Condition

This effect can be easily described. As the blades of the propeller pass by the stern frame and other adjacent parts of the hull structures, they cause a cyclic pressure perturbation at the hull. The pressure disturbances are caused by both the thickness and loading of the blades (displacement flow and circulatory flow). The effects are magnified by the nonuniformity of the wake and the presence of the hull.

The prediction of propeller-induced field pressures is possible at various levels of refinement. Breslin and Tsakonas [56] presented a theory, accounting for thickness and loading (lifting line model), for the free-field pressures of a uniform-wake propeller. Tsakonas, Breslin and Jen discussed [57] the effects of a nonuiform wake.

Wijngaarden [54] performed investigation into ways of improving the prediction procedures for vibratory hull excitation forces. In search of the major sources of prediction uncertainty the proceedings of the *International Towing Tank Conference* have been consulted. For the numerical simulation of propeller-induced hull-pressure forces two computational methods have been used, both based on the potential flow assumption and employing the *Boundary Element Method* for the discretization. One method is for the simulation of propeller flows, the other for predicting the acoustic scattering effect of the hull and free surface. On the basis of the boundary element method, a computational method has been developed for the computation of the scattering effect of the hull on incident pressures caused by propeller noise sources. The

method has been validated with model scale experiments on propellers with and without cavitation. The same boundary element method has been used to correct for the influence of model hull vibrations on the assessment of hull-excitation forces. Guidelines have been derived for the execution of model scale experiments so as to minimize vibration-induced hull pressures.

7. CONCLUSION AND FURTHER DEVELOPMENTS

In this thesis, the numerical propulsion simulations in model scale for different propeller positions were performed by using RANSE solver, ANSYS CFX commercial CFD code. The four positions of propeller were relocated in the simulations namely as Case1,2,3 and Orig. These numerical propulsion simulations for all cases were performed under two conditions: one is the simulation including hull, propeller and rudder called “Simulation with Rudder Condition” and another one is the simulation including hull and propeller only called “Simulation without Rudder Condition”.

There are several conclusions that can be made on these studies referring to the numerical CFD methods used in this thesis, the numerical investigations on the propulsion characteristics and fluid flow studies from the results of numerical simulations.

The study performed for this thesis shows the effect of propeller position that is placed behind hull in the propulsion simulations which has the influence on the propulsion characteristics mainly the propulsion efficiency. Furthermore, the influence of the rudder on the propulsion simulations for all cases are described in this thesis.

The numerical propulsion simulation method that was developed in MMG is very effective and functional tool for investigating and researching for many cases of parametric studies also. The simulations in this thesis were carried out with minimum time consumption by using this NPS method.

Regarding the investigation of the propulsion efficiency depending on propeller position, the increasing propulsion efficiency can achieve by placing the propeller away from the hull since the Case3 in this thesis gain the maximum propulsion efficiency among the other cases. This is due to the minimum delivered power found in Case3. That means the lesser installation power required when the propeller is located away aft from the hull. The other propulsion characteristics and propeller performance changed as a result of propeller relocations. The higher thrust are produced by the propeller when the distance of propeller and hull is very close. The torque results in full scale prediction have large deviations among the cases. The influence of rudder on the simulations are observed apparently and the propulsion efficiency becomes higher in simulations without rudder condition than that with rudder condition. The thrust and torque produced by the propeller are lower in “without rudder condition” than “with rudder condition” due to the rudder blockage effect.

Concerning on the pressure exerted on the hull caused by the rotating propeller, it is evident that the hull is suffering more pressure when the propeller is closer to the hull. The larger

pressure fluctuations are found in Case1 and CaseOrig in which the propeller has close distance to the hull. The pressure distribution on the hull is necessary to determine and consider to be the minimum value occurrence since this could lead to the ship vibration. Besides, the pressure exerted on the rudder can be higher when the propeller is moving aft from the hull in order to reduce the hull pressure. As mentioned by Horst Nowacki [58], these hydrodynamics pressures and forces depend on the wake field and many characteristics of propeller designed and stern configuration. The clearances of the propeller are a most significant parameter. The maximum pressure fluctuation occurs in a plane a little ahead of the propeller. This suggests generous forward axial clearance, but also a fair amount of distance from the rudder. The benefits from tip clearance are similar. Rake in the propeller is a means of providing more forward axial clearance at the expense of rudder clearance. In practice, the tip clearance was sometimes increased by cropping the blades if the corresponding increase in RPM could be afforded. Therefore, the propeller clearance for the hull and rudder must be chosen judiciously.

Moving the propeller aft from the hull indicated a great potential for power reduction. Interesting trends in propulsive factors were revealed in the simulations since the investigation was carried out with and without rudder condition. There are other benefits of having the propeller located just behind the hull. The primary reason is larger clearance and less pressure pulses and it is possible to increase the propeller diameter. [7]

In the matter of further development, the pre-processing stage in numerical CFD simulations is the most time consuming step for the engineers. In this thesis work, the geometry creation of computational ship and propeller domains in DesignModeler took 60% of the working time. Therefore, the script can be developed by using the programming language that can give commands to ANSYS Workbench and DesignModeler. Moreover, the numerical resistance simulations can be performed beneficial to evaluate the full scale prediction results by using the numerical resistance results in the combination of numerical self-propulsion and open water simulation results. In this thesis work, the required resistance data are taken from the experimental resistance test and the experimental resistance has been performed with hull and rudder. This have an effect on the results of thrust deduction factor evaluation in “Without Rudder Condition”. Therefore, the numerical resistance simulations without rudder condition should be carried out in order to get more accurate final results on the self-propulsion simulations without rudder condition.

8. REFERENCES

[1] M. M. M. GmbH, “Efficiency by MMG, Research and Innovation,” *MMG News*, 2013.

[2] Gao, Qiuxin;Wei Jin;Dracos Vassalos, “The Calculations of Propeller Induced Velocity by RANS and Momentum Theory,” *J. Marine Sci. Appl.*, vol. 11, pp. 164-168, 2012.

[3] N. Bulten, “Transient blade load determination in behind ship based on CFD”.

[4] Y.N.Win, Computation of the Propeller-Hull and Propeller-Hull-Rudder Interaction Using Simple Body-Force Distribution Model, Osaka University, 2014.

[5] C. Simonsen, R. Carstens, “NUMERICAL FLOW SIMULATION OF MODEL SHIP WITH APPENDAGES. METHOD, VALIDATION AND INVESTIGATION OF THE FLOW AROUND HULL, RUDDER AND PROPELLER,” FORCE Technology, MAN Diesel A/S and DTU, 2009.

[6] C. Wang, S. Sun, L. Li, L. Ye, “Numerical prediction analysis of propeller bearing force for full-scale hullepropellererudder system,” *International Journal of Naval Architecture and Ocean Engineering*, pp. 1-13, 2016.

[7] D.Knutsson,L. Larsson, “Large area propellers,” in *SMP'11 (Symposium on Marine Propulsors Marine Propulsors)*, 2011.

[8] D. Villa, S. Gaggero and S. Brizzolara, “Ship Self Propulsion with different CFD methods: from actuator disk to viscous inviscid unsteady coupled solvers,” in *10th International Conference on Hydrodynamics*, St. Petersburg, 2012.

[9] T. BUGALSKI, “An overview of the selected results of the European Union Project EFFORT,” *ARCHIVES OF CIVIL AND MECHANICAL ENGINEERING*, vol. 7, 2007.

[10] K. Paik, H. Park and J.Seo, “RANS simulation of cavitation and hull pressure fluctuation for marine propeller operating behind-hull condition,” *Int. J. Nav. Archit. Ocean Eng.*, vol. 5, p. 502~512, 2013.

[11] Abdel-Maksoud M,Rieck K,Menter FR, “numerical investigation of the turbulent flow around the container ship model (KCS) with and without propeller,” *A Workshop on Numerical Ship Hydrodynamics*, 2000.

[12] L. LO, “Numerical simulation of the flow around the propelled KCS,” in *Proceedings of CFD Workshop Tokyo 2005*, 2005.

[13] Carrica PM,Castro AM,Stern F, "Self-propulsion computations using a speed controller and a discretized propeller with dynamic overset grids," *Journal of Marine Science and Technology,* pp. 316-330, 2010.

[14] AQUO, "Predictive theoretical models for propeller URN," Achieve QUieter Oceans by shipping noise footprint reduction, 2015.

[15] E. Øyan, Speed and powering prediction for ships, Norwegian University of Science and Technology, 2012.

[16] Lindgren, H., Aucher, M., Bowen, B.S., Gross, A., Minsaas, K.J., Muntjewerf, JJ., Tamura, K., Wennter, R.,, "Report of Performance Cornmittee," in *Proceedings of the 15th Intemariunal Towing Tank Conference,* Th Hague, 1978.

[17] S. Molloy, Ship Powering Prediction Using Load Varying Self-Propulsion Tests, NeMoundland: Faculty of Engineering and Applied Science,MemoRal University, 2001.

[18] V. Bertram, Practical Ship Hydrodynamics, British Library Cataloguing, 2000.

[19] S. Steen, *Experimental Methods in Marine Hydrodynamics,* NTNU TRONDHEIM NORWEGIAN, 2014.

[20] I. 2008b, "Recommended procedures and guidelines 7.5 - 02 - 03 - 01.1".

[21] ITTC, "ITTC Recommended Procedures and Guidelines-1978 ITTC Performance Prediction Method," Propulsion Committee of 27th ITTC, 2014.

[22] K.J.Oh , S.H.Kang, "Numerical calculation of the viscous flow around a propeller shaft configuration," *International Journal for Numerical Methods in Fluids,* vol. 21, pp. 1-13, 1995.

[23] S.H. Rhee,S.Joshi, "Computational validation for flow around a marine propeller using unstructured mesh based Navier-Stokes solver," *JSME International Journal, Series B,* vol. 48, pp. 562-570, 2006.

[24] B.Munson, T.Okiishi, W.Huebsch, A.Rothmayer,, Fluid Mechanics. (7th edn.), Hoboken: Wiley, 2013.

[25] A.F. Molland, S.R. Turnock, D.A. Hudson, Ship Resistance and Propulsion, Cambridge University Press, 2011.

[26] P.Ferrant, *Seakeeping Lectures,* 2016.

[27] S. PERAVALI, Investigation of Effective Wake Scaling for Unconventional Propellers, Gothenburg: Chalmers University of Technology, 2015.

[28] R. Mehdipour, Simulating propeller and Propeller-Hull Interaction in OpenFOAM, Stockholm: Royal Institute of Technology, 2013.

[29] R.J. Pattenden, N.W.Bressloff, S.R.Turnock, and X.Zhang, "Unsteady simulations of the flow around a short surface-mounted cylinder," *International Journal for Numerical Methods in Fluids*, vol. 57, p. 895–914, 2007.

[30] V. I. Krasilnikov, "First Introduction into Computational Fluid Dynamics for Marine Applications," pp. 72-152, 2011.

[31] A. J. Dubas, Robust Automated Computational Fluid Dynamics Analysis and Design Optimisation of Rim Driven Thrusters, UNIVERSITY OF SOUTHAMPTON, 2014.

[32] Inc.ANSYS, ANSYS CFX-Solver Theory Guide, 2013.

[33] D.C.Wilcox, Turbulence Modeling for CFD, LA Canada: DCW Industries, 1998.

[34] H.K. Versteeg, W. Malalaskera, An Introduction to Computational Fluid Dynamics, The finite Volume Method (2nd edition), Perason Education Limited, 2007.

[35] L. Larsson, H. C. Raven, Principles of Naval Architecture: Ship Resistance and Flow, The Society of NAME, 2010.

[36] Y. Zhao, Investigation in Scale Effects on Propellers with Different Magnitude of Skew by CFD Methods, Ålesund: Ålesund University College, 2015.

[37] G.M.Rotte, Analysis of a Hybrid RaNS-BEM Method for Predicting Ship Power, Netherlands: Delft University of Technology.

[38] E.M.V.Siggeirsson,S.Gunnarsson, Conceptual design tool for radial turbines, Gothenburg: Chalmers University of Technology, 2015.

[39] F. Menter, "Two-equation eddy-viscosity turbulence model for engineering applications," *AIAA Journal 32*, pp. 1598-1605, 1994.

[40] D. Wilcox, "Reassassment of the scale-determening equation," *AIAA Journal 26*, pp. 1299-1310, 1988.

[41] M.S.A.Mintu, RANS Computation of Propeller Tip Vortex Flow for Steady and Unsteady Cases, Memorial University of Newfoundland, 2011.

[42] L. Zimmerman, Development and validation of momentum source propeller model in open-water conditions, Rolls-Royce Hydrodynamic Research, 2015.

[43] Inc.ANSYS, ANSYS FLUENT 12.0 - Theory guide, 2009.

[44] F. Inc., Fluent Solver Guide, 2001.

[45] Inc.ANSYS, ANSYS Meshing User's Guide, 2016.

[46] M. M. J.Neugebauer, “Fluid-Structure Interaction of Propellers,” in *IUTAM Symposium on Fluid-Structure Interaction in Ocean Engineering*, 2008.

[47] J. Carlton, Marine Propellers and Propulsion,2nd Edition, 2006.

[48] Vladimir Krasilnikov et al, “A Numerical Study on the Characteristics of the System Propeller and Rudder at Low Speed Operation,” 2011.

[49] Basic Principles of Ship Propulsion, MAN Diesel & Turbo.

[50] Ship Hydrodynamics Lecture Notes Part3.

[51] *SHIP RESISTANCE AND PROPULSION.*

[52] A.B.Phillips, Simulations of a self propelled autonomous underwater vehicle, University of Southampton, 2010.

[53] M. Nakisaa, A. Maimunb, Yasser M. Ahmeda, F. Behrouzia, Jaswara, A. Priyantoa, “CFD Mesh Independency Technique for a Propeller Characteristics in Open Water Condition,” *Jurnal Teknologi*, vol. 74:5, pp. 5-10, 2015.

[54] H.C.J.V.WIJNGAARDEN, Prediction of Propeller-Induced Hull-Pressure Fluctuations, Maritime Research Institute Netherlands (MARIN), 2011.

[55] T.Kawamura, “Numerical Simulation of Propulsion and Cavitation of Marine Propellers,” *Journal of the JIME*, vol. 46, 2011.

[56] J.P.Berslin, S.Tsakonas, “Marine Propeller Pressure Field Due to Loading and Thickness Effects,” *Transactions of The Society of Naval Architects and Marine Engineers*, 1959.

[57] S.Tsakonas, J.P.Breslin, N.Jen, “Pressure Field Around a Marine Propeller Operating in a Wake,” *Journal of Ship Research*, 1963.

[58] H.Nowacki, Ship Vibration Lecture Notes, University of Michigan, 1973.

[59] C. D. Simonsen, Rudder, Propeller and Hull Interaction by RANS, Denmark: Department of NAOE,DTU, 2000.

[60] G. D. Tzabiras, “A Numerical Study of Additive Bulb Effects on the Resistance and Self-Propulsion Characteristics of a Full Ship Form,” *Ship Technology Research*, vol. 44, pp. 98-108, 1997.

[61] R. Muscari, A.D.Mascio, “Numerical simulation of the flow past a rotating propeller behind a hull,” in *Second International Symposium on Marine Propulsors*, Hamburg, 2011.

[62] D. Sridhar,T V K Bhanuprakash, H N Das, “Frictional Resistance Calculations on a Ship using CFD,” *International Journal of Computer Applications,* vol. 11, 2010.

[63] N. Prakash, A. Muthuvel and D. G. Roychowdhury, “Numerical Simulation of a three bladed marine propeller in Steady and Unsteady state,” *Applied Mechanics and Materials,* Vols. 592-594, pp. 1136-1141, 2014.

[64] K. Boumediene and S.E. Belhenniche, “Numerical Analysis of Turbulent Flow Around DTMB4119 Marine Propeller,” *International Journal of Mechanical, Aerospace, Industrial, Mechatronic and Manufacturing Engineering,* vol. 10, 2016.

[65] M. Morgut, E. Nobile, “Influence of grid type and turbulence model on the numerical prediction of the flow around marine propellers working in uniform inflow,” *Ocean Engineering,* pp. 26-34, 2012.

[66] H. Versteeg, W. Malalasekera, An Introduction to Computational Fluid Dynamics,2nd Edition, Edinburgh Gate: Pearson Education Limited, 2007.

[67] E.Tokgoz, A CFD Study on the Propeller-Hull Interaction Flow in Waves Using Body-Force Distribution Model, Osaka University, 2015.

[68] A. F. Molland,S. R. Turnock, “Marine Rudder and Control Surface,” 2006.

[69] A.B.Phillips, S.R.Turnock, M.E.Furlong,, “Accurate capture of rudder-propeller interaction using a coupled blade element momentum-RANS approach,” *Ship Technology Research (Schiffstechnik),* vol. 57, p. 128–139, 2010.

[70] M. M. M. GmbH, “Evolution of high-efficiency propeller design and manufacturing,” *Ship & Offshore, GreenTech,* pp. 22-23, 2015.

[71] SánchezCaja et al, “Simulation of the Incompressible Viscous Flow around Ducted Propellers with Rudders Using a RANSE Solver,” 2008.

[72] A.Kolakoti, T.V.K.Bhanuprakash, H.N.Das, “CFD ANALYSIS OF CONTROLLABLE PITCH PROPELLER USED IN MARINE VEHICLE,” *G.J.E.D.T.*, vol. 2, pp. 25-33, 2013.